Advanced spectroscopy studies of highly-efficient emitter molecules

LARISSA GOMES FRANCA

Advanced spectroscopy studies of highly-efficient emitter molecules

Larissa Gomes Franca

A Thesis Presented for the Degree of Doctor of Philosophy

Supervisor: Professor Andrew Monkman

Organic Electroactive Research Group

Department of Physics

University of Durham

2023

Abstract:

This thesis aims to use advanced optical spectroscopy to gain deep understanding of the properties of highly-efficient emitter molecules and the key parameters that strongly influence their performance for potential application in organic light-emitting diodes (OLEDs). Through this thesis, significant factors that impact the thermally activated delayed fluorescence (TADF) molecules and their mechanisms are addressed. These molecules exhibit many factors which can affect their performance, including electronic coupling, environmental conditions, conformational arrangements, and design aspects. Initially, these techniques are employed to uncover the highly complex photophyscis properties of a specific molecule, 10-phenyl-10H,10′H-spiro[acridine9,9′-anthracen]-10′-one, known as ACRSA. As previously reported in a study involving a detailed computation chemistry, this molecule has complex behaviour due to its highly decoupled nature of the donor and acceptor units. The finding from this thesis revealed that ACRSA behaves as three different subsystems. While each these subsystems follows Kasha's rules individually, the molecule as a whole completely disregards them. Exploring the environment conditions, time-resolved optical spectroscopy studies indicate that the rigid bridge present in ACRSA prevents variations in the rates of the reverse intersystem crossing (rISC). This effect, typically observed in TADF in solid host, have significant implications for the performance of OLEDs. Apart from the photoluminescence techniques, this thesis also explores the use of pump-probe techniques as a powerful tool to analyse the role of the dark excited states in the TADF molecules. This technique combined with the optical spectroscopy techniques enables the mapping of the electronic excited states, their transition, and their nature. Finally, time-resolved optical spectroscopy was employed to study the alternative design of TADF molecule, known as through-space charge transfer (TSCT). The results obtained provided the first experimental evidence of TSCT. This study also significantly contributes to design rules for TADF molecules, demonstrating the role of the bridge on these molecules and importance of the molecular reorganisation in the TSCT formation.

Contents

List of abbreviations:

E_a – activation energy;

k_B – Boltzmann constant;

2MeTHF – 2-methyl tetrahydrofuran;

A– acceptor;

Alq_3 – tris(8-hydroxyquinoline)aluminum(III);

CT – charge transfer states;

D – donor;

DCM – dichloromethane;

DF – delayed fluorescence;

EML – emissive layer;

EQE – external quantum efficiency;

ET – electron transfer;

F – fluorescence;

FRET – Förster resonance energy transfer;

fs – femtosecond;

FWHM – full width half maximum;

$\hbar$ – Planck's constant;

HFC – hyperfine coupling;

HOMO – highest occupied molecular orbital;

IC – internal conversion;

iCCD – intensified charge coupled device;

InGaAs – indium gallium arsenide;

$Ir(ppy)_3$ – tris(2-phenylpyridine)iridium(III);

IRF – instrument response function;

ISC – intersystem crossing;

J – electron exchange energy;

K – Coulomb repulsion;

LE – locally excited states;

LUMO – lowest unoccupied molecular orbital;

MCH – methylcyclohexane;

MR – multiple resonance;

ns – nanosecond;

OLED – organic light-emitting diode;

PF – prompt fluorescence;

Ph – phosphorescence;

PhMe – toluene;

PIA – photoinduced absorption;

PL – photoluminescence;

PLQY – photoluminescence quantum yield;

QA – quasi-axial;

QE – quasi-equatorial;

rISC – reverse intersystem crossing;

RTP – room temperature phosphorescence.

S_0 – ground state;

S_1 – lowest singlet excited state;

S_n – upper singlet excited state;

SOC – spin-orbit coupling;

T_1 – lowest triplet excited state;

TA – transient absorption;

TADF – thermally activated delayed fluorescence;

TCSPC – time-correlated single photon counting;

THG – third harmonic generation;

T_n – upper triplet excited state;

TTA – triplet-triplet annihilation;

WLC – white light continuum;

ΔE_{ST} – energy splitting between singlet and triplet excited states;

λ – wavelength;

ε – extinction coefficient;

List of published papers:

2023:

(1) Pander, P.; **Gomes Franca, L.**; Dias, F. B.; Kozhevnikov, V. N. Electroluminescence of Tetradentate Pt(II) Complexes: O^N^N^O versus C^N^N^O Coordination. *Inorg. Chem.* **2023**, No. Ii. https://doi.org/10.1021/acs.inorgchem.3c00364.

(2) **Franca, L. G**.; Danos, A.; Monkman, A. Donor, Acceptor, and Molecular Charge Transfer Emission All in One Molecule. *J. Phys. Chem. Lett.* **2023**, *14* (11), 2764–2771. https://doi.org/10.1021/acs.jpclett.2c03925.

(3) Marchi Luciano, H.; Farias, G.; Salla, C. M.; **Franca, L. G.**; Kuila, S.; Monkman, A. P.; Durola, F.; Bechtold, I. H.; Bock, H. R.; Gallardo, H. Room Temperature Phosphorescence in Solution from Thiophene-Bridged Triply Donor-Substituted Tristriazolotriazines. *Chem. – A Eur. J.* **2023**, No. Ii, 0–3. https://doi.org/10.1002/chem.202203800.

(4) Stavrou, K.; **Franca, L. G.**; Böhmer, T.; Duben, L. M.; Marian, C. M.; Monkman, A. P. Unexpected Quasi-Axial Conformer in Thermally Activated Delayed Fluorescence DMAC-TRZ, Pushing Green OLEDs to Blue. *Adv. Funct. Mater.* **2023**, 2300910. https://doi.org/10.1002/adfm.202300910.

2022:

(5) **Franca, L. G.**; Danos, A.; Monkman, A. Spiro Donor–Acceptor TADF Emitters: Naked TADF Free from Inhomogeneity Caused by Donor Acceptor Bridge Bond Disorder. Fast RISC and Invariant Photophysics in Solid State Hosts. *J. Mater. Chem. C* **2022**, *10* (4), 1313–1325. https://doi.org/10.1039/D1TC04484B.

(6) **Franca, L. G.**; dos Santos, P. L.; Pander, P.; Cabral, M. G. B.; Cristiano, R.; Cazati, T.; Monkman, A. P.; Bock, H.; Eccher, J. Delayed Fluorescence by Triplet–Triplet Annihilation from Columnar Liquid Crystal Films. *ACS Appl. Electron. Mater.* **2022**, *4* (7), 3486–3494. https://doi.org/10.1021/acsaelm.2c00432.

(7) Kelly, D.; **Franca, L. G.**; Stavrou, K.; Danos, A.; Monkman, A. P. Laplace Transform Fitting as a Tool To Uncover Distributions of Reverse Intersystem Crossing Rates in TADF Systems. *J. Phys. Chem. Lett.* **2022**, *13* (30), 6981–6986. https://doi.org/10.1021/acs.jpclett.2c01864.

(8) Phan Huu, D. K. A.; Saseendran, S.; Dhali, R.; **Franca, L. G.**; Stavrou, K.; Monkman, A.; Painelli, A. Thermally Activated Delayed Fluorescence: Polarity, Rigidity, and Disorder in Condensed Phases. *J. Am. Chem. Soc.* **2022**, *144* (33), 15211–15222. https://doi.org/10.1021/jacs.2c05537.

2021:

(9) **Franca, L. G.**; Long, Y.; Li, C.; Danos, A.; Monkman, A. The Critical Role of Nπ* States in the Photophysics and Thermally Activated Delayed Fluorescence of Spiro Acridine-Anthracenone. *J. Phys. Chem. Lett.* **2021**, *12* (5), 1490–1500. https://doi.org/10.1021/acs.jpclett.0c03314.

(10) Kumar, S.; **Franca, L. G.**; Stavrou, K.; Crovini, E.; Cordes, D. B.; Slawin, A. M. Z.; Monkman, A. P.; Zysman-Colman, E. Investigation of Intramolecular Through-Space Charge-Transfer States in Donor–Acceptor Charge-Transfer Systems. *J.*

Phys. Chem. Lett. **2021**, *12* (11), 2820–2830. https://doi.org/10.1021/acs.jpclett.1c00265.

(11) Morozov, K. M.; Pander, P.; **Franca, L. G.**; Belonovski, A. V.; Girshova, E. I.; Ivanov, K. A.; Livshits, D. A.; Selenin, N. V.; Pozina, G.; Monkman, A. P.; Kaliteevski, M. A. Opposite Sign of Polarization Splitting in Ultrastrongly Coupled Organic Tamm Plasmon Structures. *J. Phys. Chem. C* **2021**, *125* (15), 8376–8381. https://doi.org/10.1021/acs.jpcc.1c02432.

2020:

(12) Stavrou, K.; **Franca, L. G.**; Monkman, A. P. Photophysics of TADF Guest–Host Systems: Introducing the Idea of Hosting Potential. *ACS Appl. Electron. Mater.* **2020**, *2* (9), 2868–2881. https://doi.org/10.1021/acsaelm.0c00514.

(13) Morozov, K. M.; Ivanov, K. A.; Belonovski, A. V.; Girshova, E. I.; Pereira, D. D. S.; Menelaou, C.; Pander, P.; **Franca, L. G.**; Monkman, A. P.; Pozina, G.; Livshits, D. A.; Selenin, N. V.; Kaliteevski, M. A. Efficient UV Luminescence from Organic-Based Tamm Plasmon Structures Emitting in the Strong-Coupling Regime. *J. Phys. Chem. C* **2020**, *124* (39), 21656–21663. https://doi.org/10.1021/acs.jpcc.0c05091.

Declaration:

All material contained in this thesis is original and is the result of my own work except where explicit reference is made to the work of others. This thesis has not been submitted in whole or part for the award of a degree at this or any other university.

Advanced spectroscopy studies of highly-efficient emitter molecules

Larissa Gomes Franca

Acknowledgements:

Firstly, I would like to thank Professor Andrew Monkman, my supervisor, for all support and invaluable guidance during these four years. His supervision enriched my career, making me a better, more confident, and independent researcher. I also extend my gratitude to all collaborators, especially the participants of the TADFlife project. This project brought together an interdisciplinary and enthusiast group, where I not only engaged in valuable research discussions but also had opportunity to meet amazing people with whom I have become friends.

Many thanks to all former/current members and visitors of the Organic Electroactive Materials (OEM) research group: Fernando, Daniel, Rongjuan, Chunyong, Danos, Suman, Ari, Patrycja, Emma, Marc, Ruth, Ines, Dan, Francesco, Hector, Kamile, Matheusz, Alaistar, Lucy, Michal, for sharing great moments together, a wealth of experiences, and valuable knowledge.

I would like to thank the following people, without whom I would not have been able to complete this research. My boyfriend, Peter – thank you for consistently encouraging and supporting me throughout these years, and for always helping me to pursue my dreams and turn them into reality. To Paloma, who was always there for me – thank you for boosting my confidence and encouraging me. Your companionship in the library and during difficult days was crucial throughout the writing process. To Kleitos, who shared this experience with me from the beginning and providing support and affection every day, filling each moment with his happiness. Thank you both for welcoming me into your lovely family! To Michele, who always filled me with affection and love – thanks for sharing every moment and embarking on all our trips together. To Deborah, who has never left me alone, particularly during the most challenging phases of this journey. To Ivan, for being part of my life over these 11 years. Thank you for your invaluable advice and genuinely care about me.

I extend my gratitude to all my friends. From the UK, Mirsini, Mayra, Aga and Przemek, your attention and care meant a lot to me. A special thanks to my Brazilian friends in Poland, especially Marli, who turned that place into my second home. To my friends back home, Cintia, Saul, Lais, Leticia and Ismael, for the wonderful moments we spent together.

Finally, I express my gratitude to my family, especially my parents and my brother. Despite the physical separation, they have consistently been there, providing encouragement and unwavering support in all my decision. Muito obrigada pelos pequenos gestos que sempre me ensinaram o significado da palavra amor!

To TADFlife project funded by the European Union's Horizon 2020 Research and Innovation Programme under grant agreement No. 812872.

To my family and friends

Dedico esse trabalho à minha família e amigos

1 Introduction

This chapter highlights the motivation behind studying highly-efficient emitter molecules, including their promising features and their critical challenges. The main objectives and a description of the organisation of this thesis follow this motivation section.

1.1 Motivation

The display technology industry has faced a revolutionary period since the first organic light-emitting diode (OLED) prototype, created by researchers at Eastman Kodak in 1987, was developed.[1] The invention of the OLED technology opened possibilities for the design of transparent, flexible, and increasingly thinner displays.[2] Consequently, the major advances in this area attracted significant interest from researchers and investment in electronic devices, which rapidly expanded and reached the consumer market. According to a recent market research report by IDTechEx, the OLED display market continues rising and is expected to grow from $16 billion in 2016 to $57 billion in 2026.[3]

Essentially, an OLED is an electroluminescent device that produces light through the flow of current.[4] The main advantage of OLED devices emerges from the use of organic semiconductors. Organic semiconductors are a promising class of optoelectronic materials which comprises π-conjugated polymers and small molecules. There exists a wide variety of such materials with versatile molecular designs. They are lightweight, may be manufactured with solution-processed techniques and can be produced at low-cost.[5] Their features have driven OLED innovation towards the next generation of display technology,[6] as in the commercial foldable smartphones, transparent OLED displays,[7–9] or with prototypes of wearable and stretchable OLED displays integrated with sensors for heart rate monitoring in real-time, announced in 2021 by Samsung.[10]

A typical OLED architecture consists of multiple layers of organic semiconductors deposited between the anode and cathode.[4] The layers are stacked one on top of another, comprising hole and electron transport layers and most importantly, the emissive layer (EML).[11] EML contains luminescent materials that are usually incorporated into host molecules. While the luminescent molecules, determine the colour of each device, the host molecules provide a medium to prevent typical concentration quenching, thus ensuring high emission efficiency.[12–14] Furthermore, by combining electroluminescence from pixels with different colours: red, green, and blue (RGB) the OLED can render any other colour.[15,16] Applying a voltage to the electrodes injects charge carriers through injection layers into the

transport layers. The carriers travel towards the EML, and as they meet, they form an exciton which, upon recombining, emits light. Due to spin statistics, the recombination process produces a 25% probability for forming singlet states and a 75% probability of triplet states in the organic emitter.[17,18] Therefore, to improve the overall efficiency of an OLED, great effort has been dedicated in the development of highly-efficient emitters which can harvest both singlet and triplet excitons.[1]

Among the several classes of organic luminescent materials, two important types of luminophores exhibit this property: phosphorescence (Ph) and thermally activated delayed fluorescence (TADF) molecules. Phosphorescence emitters have their emission originating from triplet states. These molecules contain heavy atoms, such as metals, which due the so-called heavy atom effect, facilitate the radiative decay from the triplet states.[19–21] Additionally, this effect transfers the remaining 25% of singlets into triplet states via intersystem crossing (ISC) thus, allowing them to harvest 100% of the excitons formed by electric excitation.[22] However, the heavy atom effect mainly contain metals such as iridium or platinum, which are rare and very expensive, therefore limiting the potential for application in OLED technology.[23,24]

On the other hand, TADF molecules provide an alternative route for harvesting triplet states without the need for heavy metals.[25] These molecules have a small energy gap between the lowest singlet and triplet excited states, enabling thermal up-conversion from the triplet state to the singlet manifold.[26] As a result, the emission originates from a singlet state, however with a longer lifetime than the conventional singlet emissive molecules, i.e. delayed fluorescence.[27]

The energy up-conversion mechanism is complex and affected by multiple parameters, which significantly impact the efficiency of these molecules. Hence, in this thesis, I use advanced optical spectroscopy to uncover the main variables relevant to obtaining highly-efficient emitter molecules and to evaluate the mechanisms affecting their efficiency and luminescent properties.

1.2 Objectives

The main objective of this work is to use advanced optical spectroscopy to obtain a deep understanding of highly-efficient emitter molecules for potential applications in organic light-emitting diodes. Specific objectives include:

i) exploring various photoluminescence techniques to investigate the significant electronic decoupling of the lowest excited states in thermally activated delayed fluorescence molecules in solution;
ii) identification of sources of distribution in the rates of the reverse intersystem crossing of a thermally activated delayed fluorescence molecule through photoluminescence techniques in a guest-host system;
iii) use of pump-probe techniques to map the electronic upper excited states of a thermally activated delayed fluorescence molecule;
iv) exploring photoluminescence techniques to study through-space charge transfer thermally activated delayed fluorescence molecules.

1.3 Organisation of the thesis

Chapter 1 presents a brief discussion about the motivation behind the project and the main goals of this work. **Chapter 2** covers all fundamental topics of the background theory within the context of this thesis, including molecular electronic excited states, thermally activated delayed fluorescence molecules and the environmental aspects which affect their properties. **Chapter 3** will describe the materials and the experimental procedures used, and details of the techniques employed in this work: steady-state optical spectroscopy, time-resolved optical spectroscopy, and pump-probe techniques. **Chapter 4** comprises the first chapter of experimental results, which probes emissive excited states to uncover the highly complex photophysical properties in solution and study the electronic decoupling of a spiro thermally activated delayed fluorescence molecule. **Chapter 5** employs similar techniques as in the previous chapter, however exploring the same spiro thermally activated delayed fluorescence molecule in a guest-host system. By analysing these experimental results, a deep understanding was achieved on the source of the distribution of reverse intersystem crossing rates observed in the emission decays. **Chapter 6** demonstrates that using pump-probe techniques allows us to study in-depth the dark excited states and map the excited states of a donor-acceptor (D-A) type of thermally activated delayed fluorescence molecule. **Chapter 7** explores the use of photoluminescence spectroscopy to identify and evaluate the presence of through-space charge transfer in thermally activated delayed fluorescence molecules. **Chapter 8** presents a summary of the findings, a remarking conclusion, and a future perspective of this work. Lastly, **Chapter 9** contains all the bibliographic references used in this thesis.

2 Background Theory

This chapter covers essential aspects of the background theory related to the contents of this thesis. Firstly, a brief introduction on the formation of molecular electronic excited states and the main energy transitions is presented. The discussion is followed by the discussion of important processes occurring in the molecule in the excited state and the different types of organic molecules, particularly the thermally activated delayed fluorescence molecules. The last two subsections cover the main characteristics of these TADF molecules and how the environment affects their properties.

2.1 Molecular Electronic States

2.1.1 From atomic to molecular orbitals and electronic states

Organic molecules are carbon-based compounds, therefore, most of their properties can be understood by considering carbon's electronic structure.[28] Carbon atoms have six electrons, and their orbital configuration, described as $1s^2 2s^2 2p_x^1 2p_y^1$, formally allows only to make two covalent bonds using the single occupied p_x and p_y orbitals.[29] When other atoms approach the carbon atoms to bond and form a molecule, the external force causes the *2s* and *2p* orbitals to mix and become degenerate, creating new hybrid orbitals.[30] Three different types of hybrid orbitals can be formed depending on how many electron pairs are shared in the bonding, known as *sp*, sp^2 and sp^3.[31] In ethylene ($H_2C{=}CH_2$), for example, carbon atoms share two electron pairs between them.[32] In this case, as it contains a carbon-carbon double bond, the carbon atomic orbitals form a hybrid orbital called sp^2.[28] The direct overlap between these two sp^2 hybrid orbitals of carbon form a σ bond. On the other hand, the remaining unhybridised p_z orbitals overlap sideways, forming a π bond (Figure 2.1). The p_z orbital has only one electron and is perpendicular to the sigma bond. Therefore, the electrons forming the π bond are further away from the nuclei, and the π bond is considered weaker than the σ bond.[32]

As mentioned earlier, atomic orbitals can hybridise into molecular orbitals when interacting with other atoms. According to the principles of quantum mechanics, the number of orbitals interacting equals the number of orbitals formed, giving rise to bonding and antibonding orbitals.[33] As wave functions describe the atomic orbitals, the bonding and antibonding molecular orbitals are defined by a linear combination of these wave functions (Figure 2.1).[34] Occupying less energetic bonding orbitals with electrons stabilises the bond. In contrast, occupation of the more energetic antibonding orbitals with electrons causes destabilisation of the bond. There are also non-bonding orbitals which do not participating in

bond formation, also known as free electron pairs or lone pairs, and depicted with letter *n* in diagrams and schemes. Occupation of non-bonding orbitals does not affect bond energy.[28]

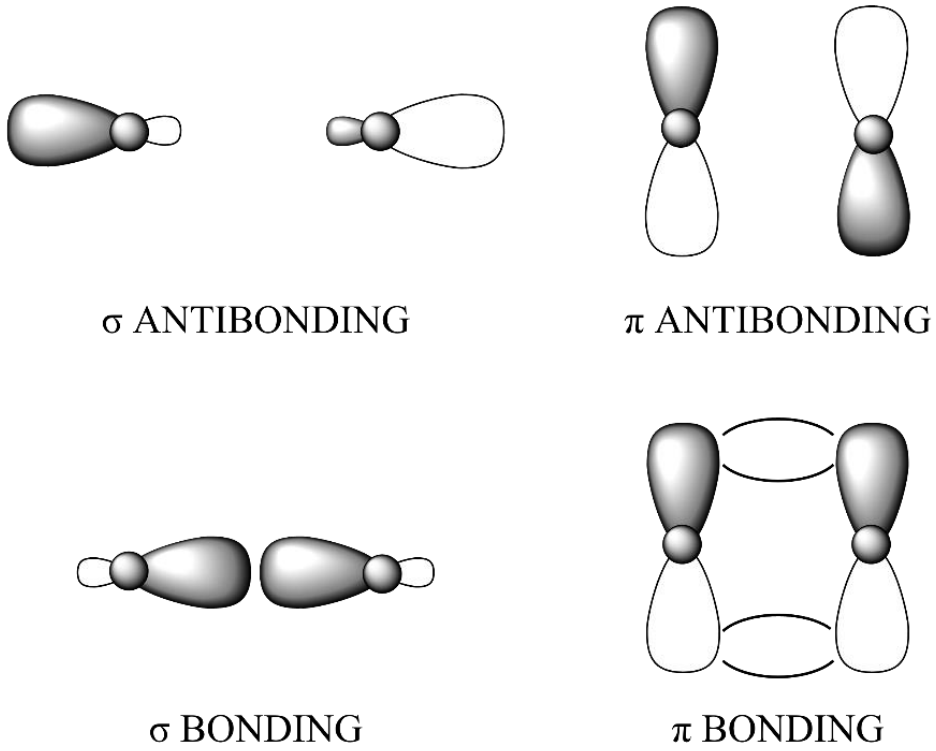

Figure 2.1: Schematic representation of the σ and π bonding and antibonding orbitals formed with sp hybridized orbitals (left) and p orbitals (right). Figure adapted from Köhler *et al*. [30]

Importantly, the orbitals will be occupied or unoccupied depending on the number of electrons in the molecule. The most energetic occupied orbital is called the highest occupied molecular orbital (HOMO), while the least energetic unoccupied orbital is called the lowest unoccupied molecular orbital (LUMO).[30] Those terms can be correlated to the inorganic semiconductors, where the HOMO and the LUMO can be associated with the valence and conduction band, respectively (although orbitals represent discreet energy levels while bands are composed of multiple energy levels, hence the term 'band' is used to describe them).[35] Particularly in the context of OLED displays, the energy level of HOMO and LUMO in the molecule have a critical role in electrical processes, essential to design the optimal device structure. Hole and electron injection into the organic semiconductor depend on the energy of the HOMO and LUMO, respectively.[36] Importantly, the experimentally determined ionization potential and electron affinity are usually associated with HOMO and LUMO, respectively.

The above description concerns molecular orbitals relevant to the molecular ground state. An electron from HOMO can be promoted to occupy a different orbital if sufficient energy is provided – we call this process an electronic transition. This process can be assigned to a type depending on the nature of the originating occupied orbital, for example $\sigma \rightarrow \sigma^*$, $n \rightarrow \pi^*$ and

$\pi \rightarrow \pi^*$ transitions. In the $n \rightarrow \pi^*$ transition, the electron moves from a non-bonding orbital to an upper π orbital. This transition tends to have low absorptivity, with molar extinction coefficient less than ~2000 $M^{-1}cm^{-1}$.[37,38] On the other hand, $\pi \rightarrow \pi^*$ transitions present higher molar extinction coefficient values of ~10000 $M^{-1}cm^{-1}$, where the electron moves from occupied to unoccupied π orbital.[37] Importantly, the molar extinction coefficient (ε) can be measured experimentally, providing a way to differentiate the nature of the transition, e.g. $n \rightarrow \pi^*$ and $\pi \rightarrow \pi^*$.

Lastly, electronic states can be defined by how the electrons are spatially distributed among the available molecular orbitals. In this context, the occupation pattern of orbitals present in the ground state is that of the lowest energy. While by providing energy to the molecule, electrons may be promoted to an upper energy level, also named as an electronic excited state.

2.1.2 Singlet and triplet electronic states

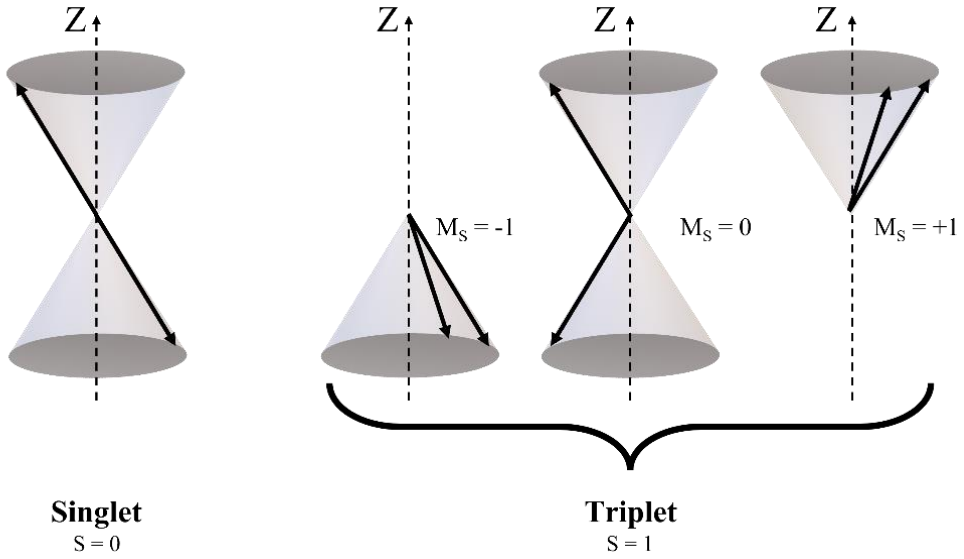

Figure 2.2: Vector model representation of the relative orientation of two electrons, forming the singlet and triplet states. Figure adapted from dos Santos.[39]

Based on Pauli exclusion principle, two electrons occupying the same electronic orbital must have paired spins. This means that paired electrons must possess opposite spin quantum numbers. In other words, the Pauli exclusion principle states that no two electrons can be described by an identical set of quantum numbers.[40] Therefore, if they occupy different orbitals then the Pauli exclusion principle does not apply and the two electrons may assume paired and unpaired spins. Singlet states occur when the electron spins are paired, so the net spin is zero. Looking at the ground state, for example, the orbitals are filled with two electrons each, which

according to Pauli exclusion principle are spin paired and therefore, the ground state is a singlet state in all organic molecules where the number of electrons is even (with exception to systems such as the diradicals in the ground state).[41] In the excited state, each of the two electrons occupies a different orbital, which allows the electron spins to be unpaired. In Figure 2.2, the total electron spin is represented by a vector sum of the individual spins. In the singlet configuration, the spin vectors are antiparallel and colinear. Such vector orientation results in a net spin vector of zero (S=0). In the triplet states, the net spin is equal 1, allowing three possible spin orientations. These three spin states correspond to the quantum numbers: M_s=-1; M_s=0; M_s=+1. Both spin vectors for M_s=-1 and M_s=+1 have their orientation antiparallel or parallel to the z-component. Even though M_s=0 of the triplet states appears to have similar spin characteristic than in the singlet states, the distinction is observed in the z-axis component. In this case, by adding these two electron's spin orientation result in a net spin vector of 1 (S=1) in the z-component.[30,42]

When modelling the singlet and triplet energy levels, two interactions play an important role: (1) Coulomb repulsion (K) and (2) electron exchange energy (J). The Coulomb term is a classical description of the interactions between the charge distribution of the electrons. On the other hand, the exchange energy is a quantum mechanical correction derived from the Pauli exclusion principle, which correlates with the relative orientation of the electron's spins. Considering these factors, the lowest singlet and triplet excited state are given by equations (2.1) and (2.2).[43]

$$E_{S1} = E + K + J \tag{2.1}$$

$$E_{T1} = E + K - J \tag{2.2}$$

$$\Delta E_{ST} = 2J \tag{2.3}$$

In equations (2.1) and (2.2), E is the orbital energy, *i.e.* the energy associated to one electron subjected to the electromagnetic field produced by nuclei and other electrons in a molecule. In one molecule, the electron configuration of the singlet and triplet excited state is the same, leading to equal values of the K and J in both equations. However, the unpaired electron's spin giving rise to a triplet excited state leads to a negative J and its energy is reduced, while in the singlet the paired electron's spin possesses positive J and its energy is increased.

By subtracting these two equations, the energy splitting between the singlet and triplet excited state (ΔE_{ST}) can be estimated as twice the exchange energy (equation (2.3)), which is calculated by the equation (2.4).[44]

$$J = \iint \Phi(r_1)\Psi(r_2)\left(\frac{e^2}{r_1 - r_2}\right)\Phi(r_2)\Psi(r_1)dr_1 dr_2 \qquad (2.4)$$

Where the Φ and Ψ represent the HOMO and LUMO wavefunctions, $r_1 - r_2$ is the spatial separation of the HOMO and LUMO, and e is the electron charge.

Therefore, ΔE_{ST} can assume values close to zero by minimising the exchange energy. Two main parameters can lead to $J \approx 0$: (i) reducing the overlap between Φ and Ψ wavefunctions, *i.e.* HOMO and LUMO in the molecule, and (ii) increasing the separation distance between the two electrons.

2.1.3 Jabłoński Diagram

The electronic states and the electronic transitions between them can be represented by an energy diagram called the Jabłoński diagram, often spelt as 'Jablonski', (named after Aleksander Jabłoński, a Polish physicist who introduced an early version of this scheme).[45] Figure 2.3 shows a typical Jabłoński diagram which is used nowadays, illustrating the electronic states and processes undergoing in organic molecules. This diagram provides a simplified representation of electronic energy levels, without accounting for energy dispersion as a function of spatial variation, such as nuclear distances.

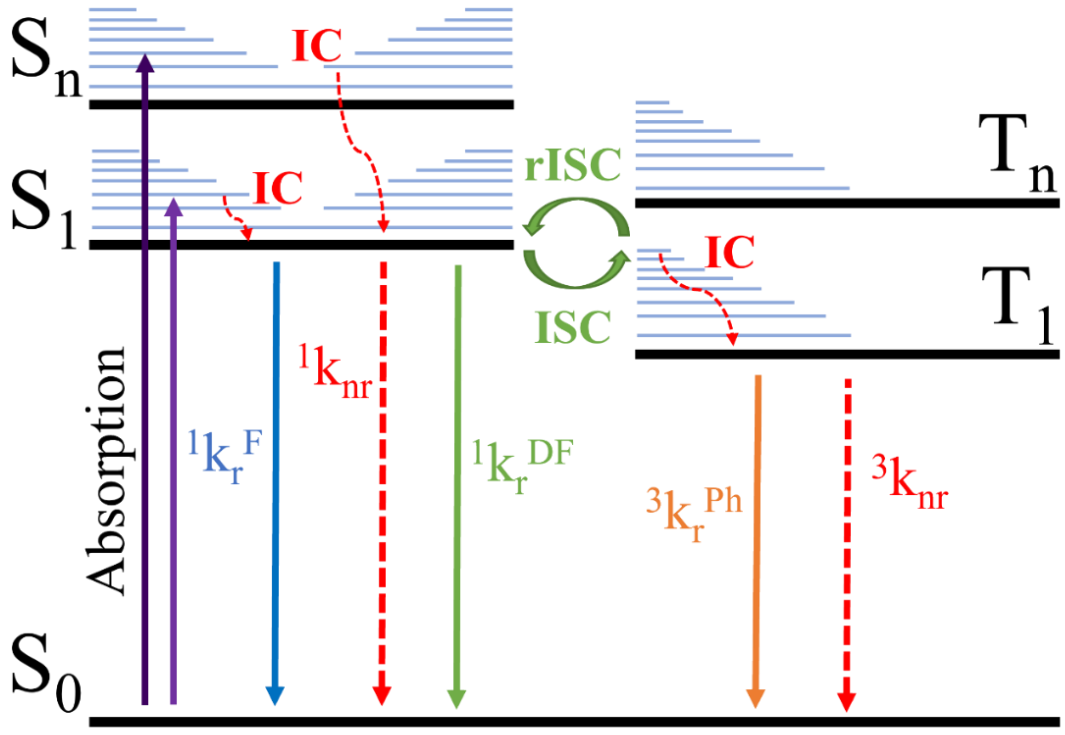

Figure 2.3: Jabłoński diagram, representing the electronic states and the transitions between them. Figure adopted from Valeur *et al.*[37]

The electronic states presented in the diagram are: S_0 (ground state), S_1 (lowest singlet excited state), S_n (upper singlet excited state), T_1 (lowest triplet excited state) and T_n (upper triplet excited state). Vibronic levels of each of the electronic excited states are represented by thin blue lines and the transitions between electronic states are depicted with vertical arrows. Note that the term vibronic refers to the interaction between electronic and vibrational states within a molecule.

When the molecule absorbs a photon, the electrons may move from ground state (S_0) to an excited state (S_1, S_n). The absorption of a photon by a molecule is a process which occurs within 10^{-15} s, and thus follows the Franck-Condon principle.[46,47] This principle states that the electronic transition occurs faster than the nuclear motion.[48]

Following absorption, several processes can occur when the electrons are in the excited state, among them non-radiative and radiative transitions, such as: internal conversion (IC), intersystem crossing (ISC), fluorescence (F), phosphorescence (Ph), and delayed fluorescence (DF). Internal conversion is a non-radiative process which occurs in two ways: (i) from an upper to the lowest electronic excited state within the same multiplicity, *i.e.* S_n to S_1 and T_n to T_1, which may occur through conical intersections, or (ii) as a vibronic relaxation to the lowest vibronic level of the electronic excited state. Vibronic relaxations are generally faster, happening within timescale of 10^{-12} to 10^{-10} s while the IC between two electronic excited state occurs within 10^{-11} to 10^{-9} s.[43] It is worth mentioning that while the IC between electronic excited states (*e.g.* S_n to S_1 or T_n to T_1) requires a conical intersection of these two states, vibronic relaxation occurs within the same state, eliminating the need for crossing between two electronic levels.

The electron in the excited state may also undergo a transition between two electronic states with different multiplicity, this process is called intersystem crossing (ISC) or reverse intersystem crossing (rISC). ISC is described when the electron is moving from the singlet to triplet excited state, while rISC is a reverse ISC transition, from the triplet to single excited state. Both ISC and rISC require a spin flip, which is principally forbidden, however, spin-orbit coupling (SOC) can facilitate this process (this mechanism will be later discussed).[42] ISC rates are usually within 10^{-10} to 10^{-8} s, therefore competing with fluorescence decay, for example.

In the lowest singlet excited state, electrons may decay non-radiatively ($^1k_{nr}$) or radiatively through fluorescence ($^1k_r^F$). Fluorescence is a radiative decay from the lowest singlet excited state to the ground state, *i.e.* $S_1 \rightarrow S_0$. Rare examples of molecules exhibit a forbidden electronic transition from $S_1 \rightarrow S_0$, thus emitting through the $S_2 \rightarrow S_0$ pathway, as seen in azulene.[49] As these electronic transitions are allowed by spin conservation, the decay is

relatively fast with average lifetime around 10^{-10} to 10^{-8} s.[37] Molecules that have their emission originating from singlet excited states are called fluorescent luminophores. The most typical OLED emitter in this category is the tris(8-hydroxyquinoline)aluminum(III) (Alq_3).[50]

Triplet excited states are populated by ISC directly via S_1 to T_1 or indirectly through upper electronic and/or vibronic triplet excited states. As discussed before, the electron in the upper electronic (T_n) or vibronic triplet excited state populates the lowest triplet excited state (T_1) through one of the presented non-radiative processes. Similarly to the singlet excited states, the lowest triplet excited state can decay non-radiatively ($^3k_{nr}$) or radiatively to the ground state through a process called phosphorescence. Phosphorescence is a radiative decay from the T_1 to the S_0, which due to the spin-forbidden nature of the transition occurs only thanks to spin-orbit coupling. Consequently, the decay from T_1 is very slow, in a range of 10^{-6} to 1 s.[51] Spin-orbit coupling is usually facilitated by the heavy atom effect, therefore phosphorescent materials are predominantly transition metal-based molecules.[22] A well-known OLED material of this class is the tris(2-phenylpyridine)iridium(III) ($Ir(ppy)_3$).[52]

As mentioned before, fluorescence and phosphorescence are radiative transitions occurring from the lowest excited state, S_1 and T_1, respectively. This is a consequence of Kasha's rule, which states that radiative transition of an electronic state of a given multiplicity in a molecule occur from the lowest electronic state of that same multiplicity.[53] Radiative decays can be quantitatively described through its radiative rate constant ($k_r = PLQY/\tau$, where PLQY is the photoluminescence quantum yield and τ is the radiative decay lifetime).

Lastly, delayed fluorescence is radiative decay from S_1, which is populated from a triplet excited state via rISC. This is a radiative transition from the $S_1 \rightarrow S_0$ but preceded by a non-radiative $T_1 \rightarrow S_1$ process which results in a significantly longer decay time than for typical fluorescence. Therefore, this process is called delayed fluorescence.[37] There are two main mechanisms for delayed fluorescence: (i) triplet-triplet annihilation (TTA) or P-type DF and (ii) thermally activated delayed fluorescence (TADF) or E-type DF. While TTA gains energy to upconvert triplet states into a singlet excited state by collision and merging of two triplet excitons, TADF molecules can achieve this by thermal energy.[45] TADF will be further discussed in the following section.

2.2 Thermally Activated Delayed Fluorescence

2.2.1 Overview

Discovery of delayed fluorescence trigged significant advances in the optical spectroscopy field. The mechanism was first reported by Perrin *et al*.[54] in 1929 in the eosin molecule. It was later characterised in more detailed by Lewis *et al*.[55] This therefore inspired the name of the mechanism as E-type delayed fluorescence at the time, which is nowadays known as thermally activated delayed fluorescence mechanism. Years later, in 1961, Parker and Hatcher[56] were the first to propose the current mechanism as it is understood today. Since then, many works have aimed to identify and explore this effect in different molecules. However, a report by Endo *et al* from 2011 had a significant impact on the use of this class of molecules by showing the great potential for improving OLED efficiency.[57]

TADF enables thermal upconversion of triplet states into singlet states, as the ΔE_{ST} is very small for this type of molecules. Usually, ΔE_{ST} assume values below 0.2 eV, therefore due to the Boltzmann distribution, there is enough thermal energy to convert substantial population of the triplet into the singlet states at room temperature.[58] As previously discussed in section 2.1.2, ΔE_{ST} can be expressed in terms of the exchange energy (J), and minimising J becomes an important requirement to achieve TADF. A strategy to minimise J is by obtaining a spatial separation between the HOMO and LUMO.[44] Thus, properly designing TADF molecules plays an important role. This aspect will be discussed in the following section.

2.2.2 Designing TADF molecules

To obtain the spatial separation of HOMO and LUMO, a typical molecular structure for TADF molecules comprises a donor group (electron rich, D) attached to an acceptor group (electron deficient, A). Many D and A groups have been used over the years to synthesise molecules and evaluate the TADF potential. In these studies variations in the D and A strength, the linkage, and other parameters have been considered.[43] Examples of typical D and A groups are given in Figure 2.4. By linking these units in a near orthogonal relative orientation, typically through a C-N bridging bond, a small ΔE_{ST} is achieved.[59] Because of this orthogonal D-A relative orientation, these units are decoupled and behave independently from each other, forming their own excited states, namely locally excited (LE) states. Additionally, by interacting weakly with each other, these units also form charge transfer (CT) states.

There are several ways to connect the donor and acceptor units, for example: by C-N bond, by the spiro bridging or even using neutral spacers and bridges. Majority of TADF

molecules reported are C-N linked, and thus relative rotation between the D and A is allowed. The variation of the D-A dihedral angle strongly affects the TADF mechanism, such as rISC rate, and importantly gives rise to a possible stable ground and excited state conformers.[60] Spiro TADF molecules, on the other hand, have a rigid and orthogonal bridge, which is enforced by the tetrahedral configuration of the sp^3 hybridised spiro carbon atom.[61] This restricts relative D-A motion and consequently, reduces rates distributions in the TADF behaviour. Alternatively, an inert scaffold/bridge can increase the separation of the D and A, giving rise to a through-space type of TADF molecules.[62] Figure 2.4 shows examples of TADF molecular structures representative to each of these types.

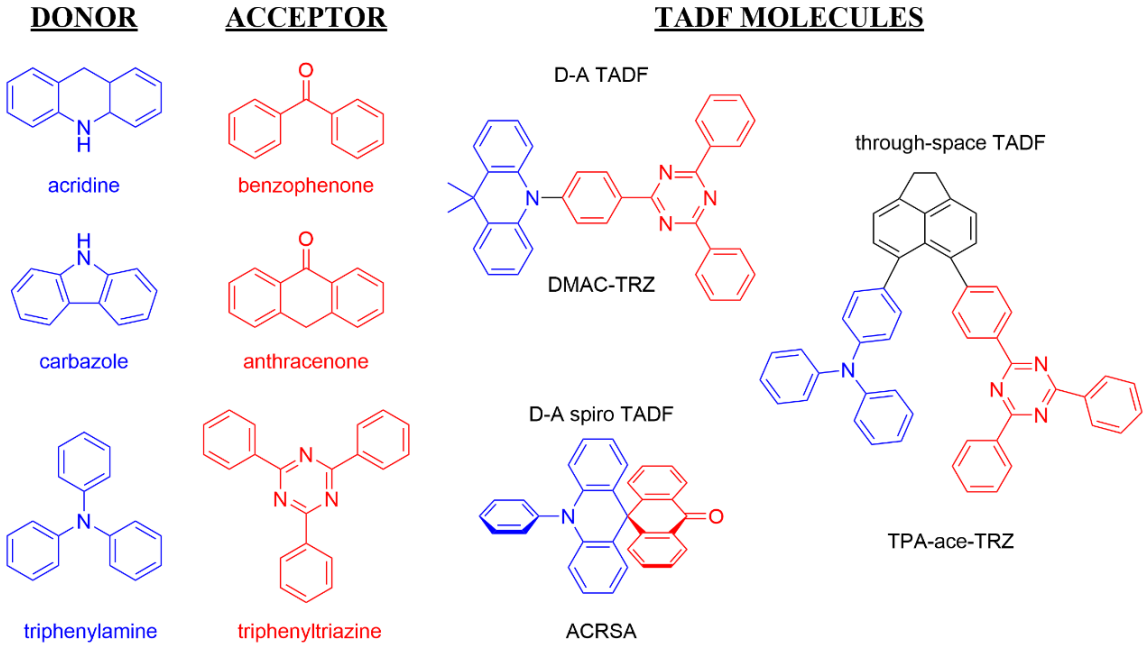

Figure 2.4: Molecular structure of the typical donor (blue) and acceptor (red) groups, and different structures of TADF molecules.

Apart from these typical TADF molecules, which contain D and A groups in their structure, there is an emerging class called multiple resonance (MR) TADF molecules.[63] The MR TADF molecules are designed to achieve HOMO and LUMO separation in plane. This is possible by introducing donor and acceptor atoms in different regions of the molecule within one plane, forming an alternating electron density distribution pattern over the molecular structure, *i.e.* the HOMO electron density is 90° out of phase with that of the LUMO.[64,65]

2.2.3 Jabłoński diagram for TADF molecules

As previously mentioned, both LE and CT states are present in the TADF molecules. LE states refers to the localised excitation of the molecule, which can be either located on the donor or acceptor groups, for example. LE states can show vibronic structure in their emission

spectra.[37] On the other hand, CT states formation involves a charge redistribution in the excited state of the molecule, therefore CT states present a significantly increased dipole moment with the respect of the ground state.[66] Thus, a way to distinguish these two characters of excited states, LE and CT, through their emission spectra is by changing solvent polarity. CT states present higher polarity dependence in their emission spectra than LE states, and hence a more detailed discussion on the effects of environment on these molecules will be made in section 2.3.

Figure 2.5 shows a modified Jabłoński diagram representing the TADF mechanism, considering the LE and CT states present in these molecules.

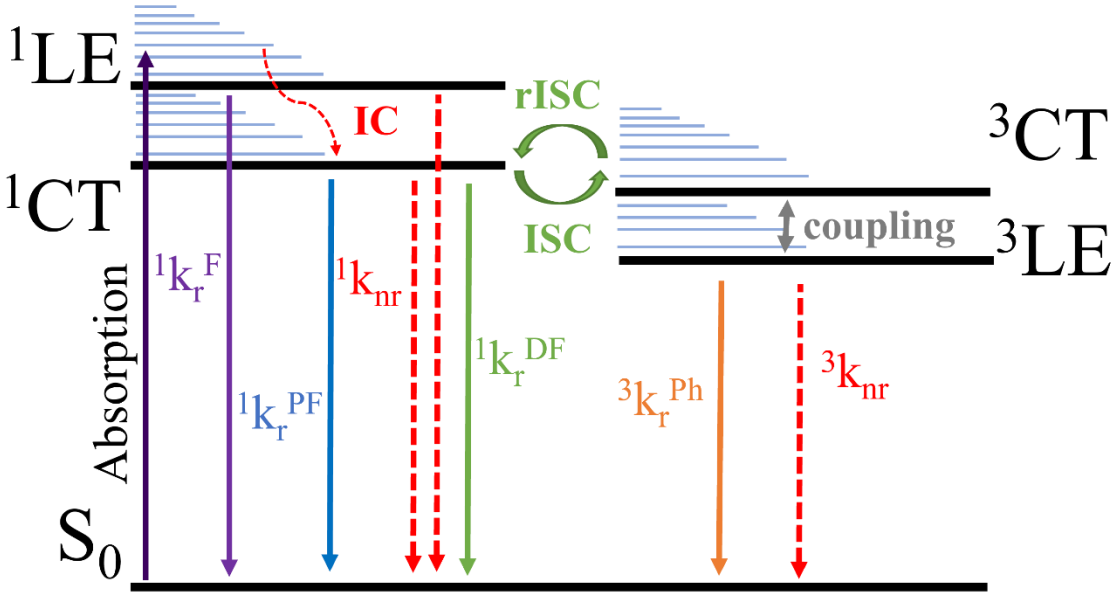

Figure 2.5: Jabłoński diagram for TADF molecules, representing the electronic states and the transitions involved in the mechanism. Note that the coupling between ^{3}LE and ^{3}CT is attributed to vibronic coupling. Figure adapted from dos Santos.[39]

By optically exciting the molecule, electrons may populate the singlet LE states (^{1}LE), either from the D or A unit, or directly populating the ^{1}CT state by the weak CT absorption band. In the case of the first pathway, from the lowest ^{1}LE state, several processes compete with each other: i) radiative/ non-radiative decays from the ^{1}LE state ($^1k_r^F$ /$^1k_{nr}$), ii) electron transfer (ET) populating the ^{1}CT state, and iii) ISC populating the triplet excited state. Importantly, while the probability of each of the processes occurring is highly dependent on their rates, the rates can be tuned by molecular design.[37] For example, slow ET can be achieved by decoupling the D and A units, *i.e.* by positioning these units nearly orthogonally to each other. As a result, a larger proportion of emission from the ^{1}LE states would be detected in the first few nanoseconds of decay.

Similarly to the ^{1}LE state, once the ^{1}CT state is populated, electrons can enter three different channels for deexcitation: (1) radiative decay or prompt fluorescence ($^1k_r^{PF}$), (2) non-radiative decay ($^1k_{nr}$) and (3) ISC populating the triplet excited state. Once the triplet excited states are populated, electrons may undergo either radiative (phosphorescence) or non-radiative decays ($^3k_r^{Ph}/^3k_{nr}$), or transition back into the singlet excited states through rISC.[39,43] The latter process will require a small ΔE_{ST} and sufficient thermal energy, therefore the equilibrium between the singlet and triplet excited states enables the spin flip and the rISC. This gives rise to the TADF mechanism, which the singlet excited state emits with longer lifetime as the mechanism is driven by the triplet excited state. Consequently, the TADF mechanism is highly dependent on temperature, but also due to its longer lifetime, both TADF and phosphorescence are very susceptible to quenching, such as by molecular oxygen.[67,68]

It is worth mentioning that CT absorption is often considerably weaker compared to the absorption of the LE states. Upon optical excitation, the CT states can be directly populated through this less intense band, or indirectly populated by the LE states. However, in OLED devices, electronic excitation populates the lowest singlet excited state, usually the CT state, through charge recombination. Therefore, it is necessary to emphasize that the photophysical properties cannot be straightforwardly translated into the behaviour in the device.

2.2.4 rISC rates and relevant interactions

According with the equation (2.5), the rISC rates which drive the TADF mechanism can be described as:

$$k_{rISC} = k_{rISC}^0 e^{-\frac{E_a}{k_B T}} \tag{2.5}$$

where k_{rISC}^0 is a pre-exponential factor, E_a the activation energy for the TADF process, k_B is the Boltzmann constant and T is temperature. Through this equation, an important plot can be obtained, known as Arrhenius plot, which allows to estimate the activation energy of the process. For most of the TADF cases, the E_a can be directly correlated to the ΔE_{ST}.[69] This equation is simplistic and most often adopted to describe rISC rates, where the critical factor to affect the rate is the ΔE_{ST}. However, it is known that the coupling interactions, such as spin-orbit coupling, vibronic coupling, and hyperfine coupling, play an important role to determine rISC rates. Specifically, when aiming to minimise the ΔE_{ST}, the ^{1}CT and ^{3}CT excited state become degenerate, resulting in zero SOC. Consequently, an additional third state (^{3}LE) is necessary to facilitate efficient ISC/rISC.[70] As a result, describing TADF simply as function of ΔE_{ST} is as simplistic model and does not accurately represent the main factor influencing the

mechanism. Therefore, the second-order perturbation theory is required to address this issue, offering a more rigorously view to express the rISC rate in the context of the TADF mechanism:[71]

$$k_{rISC} = \frac{2\pi}{\hbar} \left| \frac{<^1\psi_{CT}|\hat{H}_{SOC}|\,^3\psi_{LE}><^3\psi_{LE}|\hat{H}_{vib}|\,^3\psi_{CT}>}{\delta(^3E_{LE} - ^3E_{CT})} \right|^2 \delta(^3E_{LE} - ^1E_{CT}) \quad (2.6)$$

where the number π is divided by the Planck's constant ($\hbar$). In the equation, the first term considers the coupling between the ^{1}CT and ^{3}LE states via SOC. Additionally, the SOC term incorporates another coupling, namely hyperfine coupling, involving the interaction between the ^{3}CT and the ^{1}CT, using the ^{3}LE as a mediator state. The second term in the equation considers a vibronic coupling, which drives the interaction between the ^{3}LE and ^{3}CT states. Importantly, the vibronic coupling play a crucial role in the ISC/rISC mechanism, by effectively mixing the ^{3}LE and ^{3}CT states. This mixing, as initially described by Lim *et al*,[72] is significant because it facilitates the transition to ^{1}CT by SOC, considering that the transition from ^{1}CT to ^{3}CT is degenerate and consequently has zero SOC. Therefore, the following section will further discuss each of these couplings.

i. Spin-orbit coupling (SOC):

Spin-orbit coupling is a mechanism which allows a formally spin-forbidden processes, such as ISC, rISC and phosphorescence ($T_1 \rightarrow S_0$) to occur.[73] This interaction involves an oscillation in resonance resulting in the mixing of singlet and triplet states. The mechanism occurs as the electron rotation around the nucleus generates a magnetic moment, *i.e.* the orbital motion.[42] While the electron's spin generates another magnetic moment. These two magnetic moments interact with each other giving rise to the SOC. The strength of this coupling varies depending on the atomic number of the atoms, therefore heavy atoms (*e.g.* bromine - Br, lead - Pb, platinum - Pt) induces a strong SOC leading to fast ISC rates. Even for light atoms, the topology of the involved orbitals also plays a significant role, which can also lead to SOC.[74] An example of this phenomenon is the transition from nπ to ππ* observed in benzophenone.[75] Thus, this effect is particularly evident in metal complexes, typical phosphorescent luminophores. As the SOC depends on both, spin magnetic and spatial angular momenta, the coupling between singlet and triplet states described by the same pair of orbitals is zero.[37] Consequently, the presence of both CT and LE states within TADF molecules is required to achieve significant SOC. This coupling facilitates rapid rISC rates (*e.g.* ^{1}CT and ^{3}LE), which is not possible between ^{1}CT and ^{3}CT.[43]

ii. Vibronic coupling:

As previously mentioned, the ISC and rISC rate are strongly dependent on spin-orbit coupling interactions, implying that different orbitals (or orthogonal orbitals) should participate in these processes. A key factor for achieving fast rISC (and ISC) rates is minimising ^{1}CT-^{3}CT energy gap; however, when these states are degenerate, it results in zero spin-orbit coupling. Therefore, to facilitate the rISC (and ISC) rate a second triplet excited state, very close in energy to the ^{3}CT state but having a different orbital character, is required.[72] Through vibronic coupling with ^{3}CT, this second triplet excited state mediates the required spin flip and couples the CT triplet back to the singlet manifold. This coupling state can be either a local triplet state (^{3}LE) or a higher lying triplet CT state.[76]

The vibronic coupling involves the interaction between electronic and nuclear motions, also known as nonadiabatic mixing.[77,78] In the TADF mechanism, this interaction is responsible for mixing between the triplet states, *e.g.* ^{3}LE and ^{3}CT. Vibronic coupling forms an equilibrium between these two states with less thermal activation required. Importantly, the critical role of this coupling for rISC rates has previously been shown. Which by reducing the vibronic coupling between ^{3}LE and ^{3}CT, significantly reduces the rISC rates.[79,80] Therefore, vibronic coupling plays an important role in mediating the rISC mechanism by coupling ^{3}LE and ^{3}CT.

iii. Hyperfine coupling (HFC)

Hyperfine coupling originates from the interaction between the nucleus and electrons magnetic momenta.[81,82] In TADF molecules, HFC induces an ISC pathway between ^{1}CT and ^{3}CT. However, the HFC constant has been shown to be very small, in the range of 10^{-4} meV, when compared to other coupling constants such as SOC.[78] Therefore, this coupling constant is mostly accounted for in systems with significantly smaller SOC.

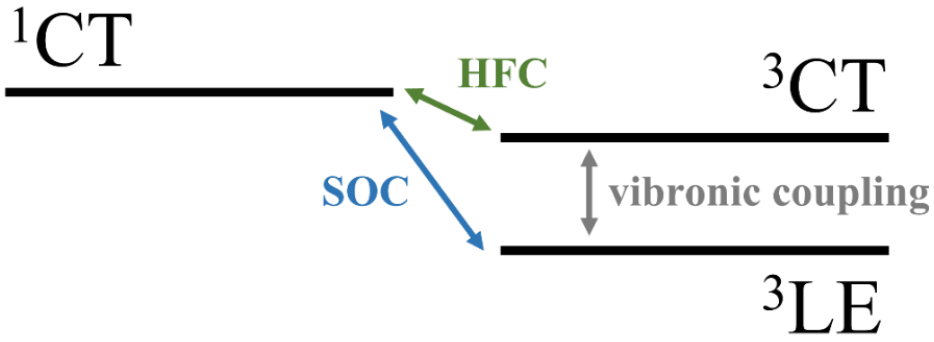

Figure 2.6 : Representation of the coupling interactions between the electronic states involved in the TADF mechanism. Figure adapted from Dias *et al*.[43]

2.3 Environment effects

As previously mentioned, CT states are highly sensitive to their local environment, therefore the environment effect have a significant impact on TADF properties. Some of which will be explored in this section.

2.3.1 Solvatochromism

Solvent molecules surround or solvate molecules and the interaction between them (solvent and solute) gives rise to changes in their photophysical properties.[83] The effect of this interaction depends on the electronic transitions in the molecule and the properties of the solvent, such as its polarity. In the ground state the molecules will be stabilised by the interaction with the dipole moment of the solvent, and by exciting the molecular electronic states, a reorganisation on the electronic distribution changes the solvent-solute interaction.[84] The result of that is called a solvatochromic effect, which is evidenced by a shift in the absorption and emission band in solvents of different polarity. Solvatochromism is dependent on solvent polarity, associated with the static dielectric constant and the dipole moment of the solvent molecules.[85] Absorption and emission bands related to different electronic transitions undergo different solvatochromic effects, according to their orbital nature and the transition dipole moments of the molecule. The transition dipole moment represents the change in dipole moment resulting from the displacement of charges during a transition.[37] Molecules with a high transition dipole moment experience a significant change in their dipole moment when in the excited state. Therefore, upon exciting the molecule in high-polarity solvents, the difference in dipole moment between the ground state and the excited state (transition dipole moment) leads to a reorganisation of the solvent molecules. This reorganisation, known as solvent relaxation, serves to stabilise the molecule. This effect can be observed through time-resolved photoluminescence measurements, where a temporal emission shift occurs within the nanosecond time regime.[45]

Importantly, the magnitude and the direction of the shift is often used to identify the character of the electronic transition.[84] For example, bands with a CT character involve a significant increase in the dipole moment from the ground state to the excited state. In this case, in solvent of higher polarity, the CT is better stabilised relative to ground state. This leads to a redshift or bathochromic shift in the absorption and emission band, also called as positive solvatochromism (seen in Figure 2.7). On the other hand, $n \rightarrow \pi^*$ transition has its ground state better stabilised than the molecule in the excited state, leading to a blue shift or hypsochromic shift in the absorption and emission band, also known as negative solvatochromism.[86]

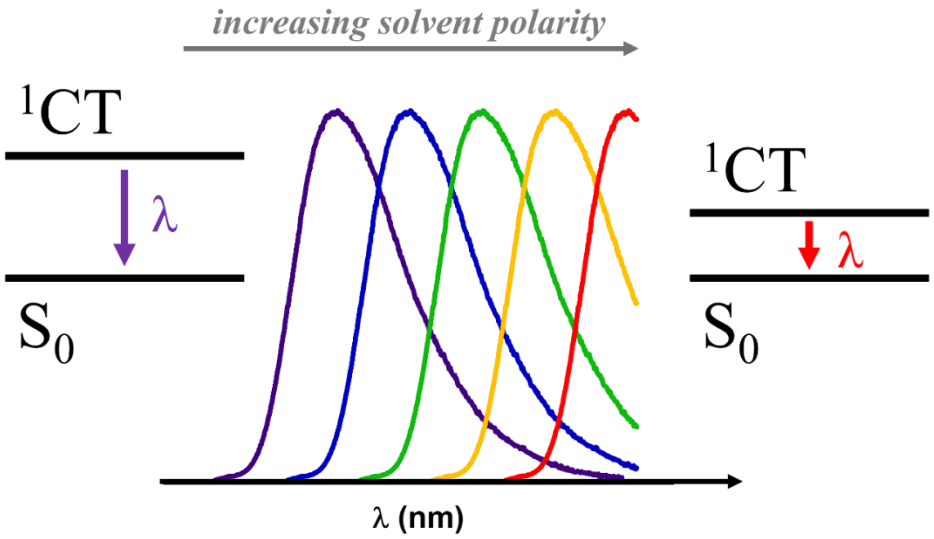

Figure 2.7: Diagram representing the positive solvatochromism (bathochromic shift) in CT emission bands.

In the context of TADF molecules, positive solvatochromic effect is a significant experimental indication for CT state formation.

2.3.2 Solid films

To facilitate the practical use of organic molecules in OLED devices, one should study and understand their properties in solid films in detail. TADF emitters in neat films may display quenching in their emission properties due to aggregates formation, for example, which is a source of non-radiative losses.[12,13,45] Therefore, use of host molecules for TADF is essential to avoid quenching and helps to control the electrical transport properties.[14] Different types of host molecules have been used for TADF molecules, among them, polymers, and small molecules. Host molecules have strong influence on the TADF mechanism, particularly due to their static dielectric constant, polarizability, rigidity and packing properties. An example is that the host environment which can directly affect dihedral angles between the donor and acceptor units, molecular conformations, as a result affecting the ΔE_{ST}.[87,88]

TADF molecules can also form stable molecular conformers in ground and excited states. An example is the **3,7-DPTZ-DBTO$_2$**, a D-A-D type of TADF molecules, which showed two coexistent configurations where D and A units are orthogonal, in which due to their different relative orientations are called axial and equatorial conformers. Figure 2.8 shows an X-ray crystal structure of this molecule, showing both conformers of the phenothiazine donor.[89,90] As mentioned before, the energy of the CT state is highly dependent on the relative orientation between the D and A unit. When the D and A are positioned orthogonally, the lowest energy CT is formed, consequently leading to a smaller ΔE_{ST}. By moving away from the orthogonality

between to D and A, a higher energy CT is formed, resulting in a larger ΔE_{ST}.[91] As a result, each relative position between D and A forms a conformer, which has a specific CT state energy. Usually, the evidence of these conformers can be seen from calculations and optical measurements. In solution state, these stable conformers are rather difficult to detect due to the fast interconversion between the two forms. However, in solid films, these stable and other types of conformational effects have a strong impact on the photophysics properties.[92] Due to the more restricting, rigid environment, the TADF molecules can be locked in different conformational positions. Each of these conformers comprises of a different dihedral angle between the D and A units leading to varies ΔE_{ST} and rISC rates.

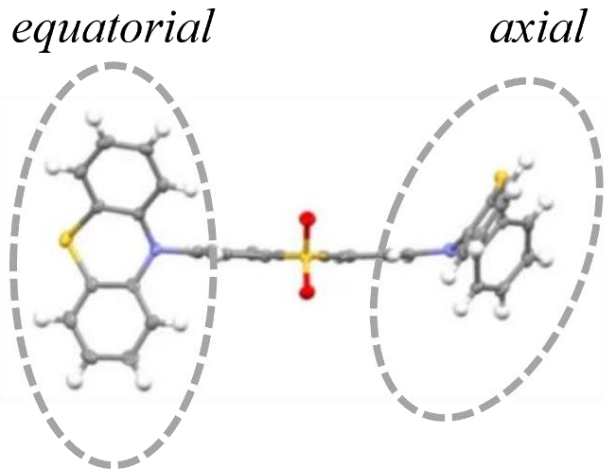

Figure 2.8: X-ray crystal structures of **3,7-DPTZ-DBTO$_2$** showing both axial (left) and equatorial (right) conformers of the phenothiazine donor. Adapted from Etherington *et al.*[80]

2.3.3 Reorganisation of energy levels

As previously discussed, the CT states are very sensitive to the environment, varying energy in solution by solvent polarity, or in solid film by the different molecular conformation which assumes a distribution of D-A dihedral angles.[93] The different responses to changes in the local embedding environment of the CT and LE excited states combined to the crucial interplay between them, causes a reorganisation of the energy levels by changing the environment, consequently affecting the ΔE_{ST} and the coupling interactions for the TADF mechanism.[94,95] This highlights that all states involved in the mechanism and the energy gaps between them should be considered in order to optimise the mechanism. Three different cases of the TADF mechanism are observed by varying the CT states energy. Figure 2.9 shows the configuration of the electronic energy levels for each of these scenarios:[78,96] (i) ^{1}CT/^{3}CT > ^{3}LE: the ^{3}LE state is lower in energy than the CT states (both ^{1}CT and ^{3}CT); (ii) ^{1}CT/^{3}CT = ^{3}LE: the three states involved (^{3}LE, ^{1}CT and ^{3}CT) are energetically aligned with each other, and (iii)

^{1}CT/^{3}CT < ^{3}LE: the ^{3}LE state has higher energy than the CT states (both ^{1}CT and ^{3}CT). It is important to note that the rISC rates have been shown to be more efficient for cases when there exists strong vibronic coupling between the ^{3}LE and ^{3}CT. Therefore, when designing a TADF molecule, it is important to note that just tuning the ΔE_{ST} is insufficient and one must pay close attention to the energy gaps between the ^{3}LE and ^{3}CT, ^{3}LE and ^{1}CT and ^{3}CT and ^{1}CT states.[43,79,80] The interaction between these states and the influence of these gaps for the TADF mechanism will be further explored in the experimental part of this thesis.

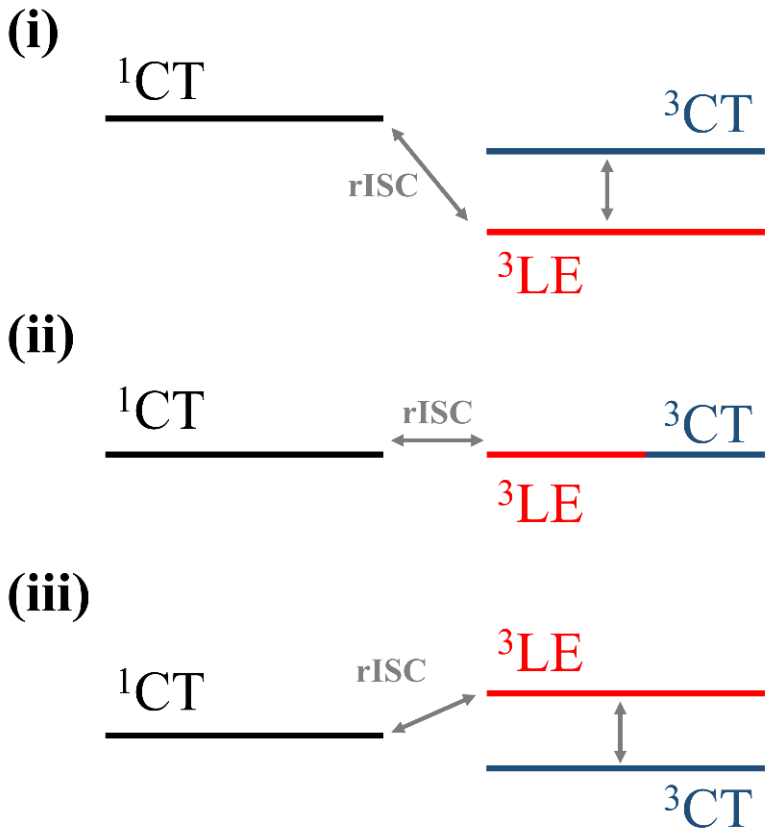

Figure 2.9: Schematic energy level diagram representing the three different configurations of electronic excited states affecting the TADF mechanism.

2.3.4 Intermolecular interactions

Lastly a deep understanding of the intermolecular interactions is necessary to uncover the impact of the environmental effects on the dynamics of the TADF molecules. Intermolecular interactions between the luminophores can lead to molecular aggregates, which may cause luminescence quenching.[45] These intermolecular interactions are often observed in neat films of TADF molecules, as previously mentioned. Consequently, molecular packing is an important parameter in the formation of aggregates and is highly dependent of the

geometries and structures of the molecules. In this context, large aromatic structures, due to their rigidity and planarity, are known for displaying strong intermolecular interactions such as π-stacking leading to the formation of dimer and excimer species.[97] Formation of dimer species can be defined by the interaction between molecules in the ground state, while the excimer species form through interaction in the excited state.[37] The photophysical properties of both species, dimers and excimers, are similar. Usually, excimers/dimers can be detected in high concentration samples. Their photoluminescence (PL) spectrum is red shifted in respect to the monomer and often structureless, they also display a longer decay lifetime in comparison to the monomer decay.[45] Due to these features, the formation of dimer and excimer species may produce a new channel for the decay and is therefore strongly affecting the photoluminescence and TADF mechanism.[98]

3 Materials and Experimental Methods

This chapter covers the essential foundation underlying the data presented in this thesis. This includes a comprehensive overview of the materials used, the sample preparation procedures, the experimental methods employed, and the data processing utilised. Specifically, in the experimental methods section, a description of the advanced optical spectroscopy techniques utilised for characterising the highly-efficient emitter molecules will be provided, such as the steady state, time-resolved photoluminescence and pump-probe measurements.

3.1 Materials

Given the objective of evaluating various advanced optical spectroscopy techniques for characterising highly-efficient emitter materials, several organic semiconductors were employed in this project. While the **Chapters 4, 5** and **6** focused on the investigation of previously published and commercially available materials, the **Chapter 7** explored newly synthesised emitter molecules. The materials discussed on **Chapter 7** was synthesised in the research group led by Professor Eli Zysman-Colman in the EaStCHEM School of Chemistry at the University of St. Andrews. Table 3.1 summarise detailed information about all the materials involved in this project, such as: molecular structure, chemical names, acronyms, type of the molecules.

Table 3.1: Summarise information about the materials studied in this project, including the TADF molecules, the donor (D), acceptor (A) and bridge/scaffold (B) units, and the host molecules. Note that the specific details of each material, includes their molecular structure, chemical names, acronyms, types of molecules, sources, and the chapters they can be found.

Molecular structure	Chemical name	Acronym	Type	Source	Chapter
Emitter molecules					
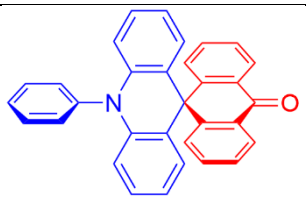 ACRSA	10-phenyl-10H,10′H-spiro[acridine9,9′-anthracen]-10′-one	**ACRSA**	Spiro TADF	Commercial	4,5
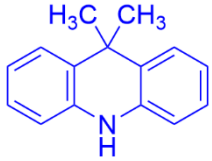 acridine	9,9-dimethyl-9,10-dihydroacridine	Acridine	D unit	Newly synthesised[a]	4,5

 anthracenone	9(10H)-anthracenone	Anthracenone	A unit	Commercial	4,5
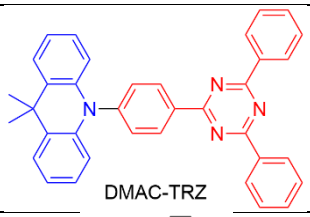 DMAC-TRZ	10-(4-(4,6-diphenyl-1,3,5-triazin-2-yl)phenyl)-9,9-dimethyl-9,10-dihydroacridine	**DMAC-TRZ**	D-A TADF	Commercial	6
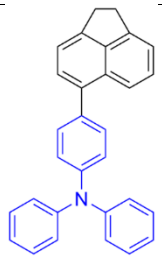 TPA-ace	4-(1,2-dihydroacenaphthylen-5-yl)-N,N-diphenylaniline	**TPA-ace**	D-B	Newly synthesised[b]	7
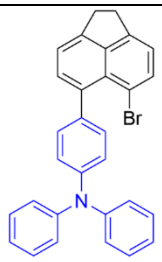 TPA-ace-Br	4-(6-bromo-1,2-dihydroacenaphthylen-5-yl)-N,N-diphenylaniline	**TPA-ace-Br**	D-B-Br	Newly synthesised[b]	7
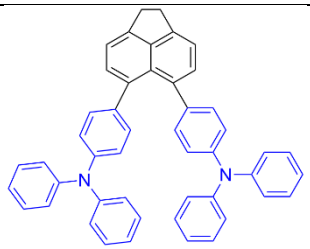 2TPA-ace	4,4'-(1,2-dihydroacenaphthylene-5,6-diyl)bis(N,N-diphenylaniline)	**2TPA-ace**	D-B-D	Newly synthesised[b]	7
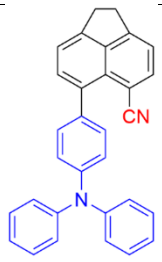 TPA-ace-CN	6-(4-(diphenylamino)phenyl)-1,2-dihydroacenaphthylene-5-carbonitrile	**TPA-ace-CN**	D-B-A	Newly synthesised[b]	7

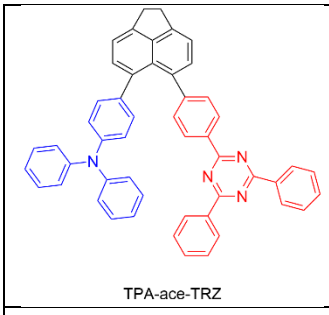 TPA-ace-TRZ	4,4'-(1,2-dihydroacenaphthylene-5,6-diyl)bis(N,N-diphenylaniline)	**TPA-ace-TRZ**	D-B-A	Newly synthesised[b]	7
Host molecules					
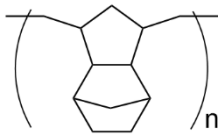 zeonex	zeonex[c]	zeonex	Polymer	Commercial	4,5,7
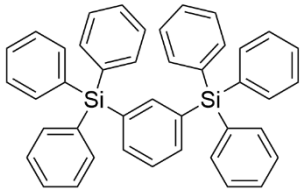 UGH	1,3-Bis(triphenylsilyl)benzene	UGH	Small molecule	Commercial	5
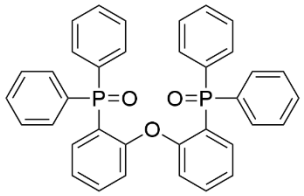 DPEPO	bis[2-(diphenylphosphino)phenyl]ether oxide	DPEPO	Small molecule	Commercial	5

[a] Synthesised by Dr. Suman Kuila in the Department of Chemistry at Durham University. [b] Synthesised by Dr Shiv Kumar in the EaStCHEM School of Chemistry at the University of St. Andrews.[c] Here is shown a general molecular structure for this type of polymer, as the specific molecular structure for this material is not known.

3.2 Sample preparation

In this section, a concise description of the methodology utilised for the preparation and treatment of the samples will be provided.

3.2.1 Solutions

Initially, stock solutions were prepared in toluene at concentration of 1 mg/mL or 10^{-3} M. For subsequent dilutions, a portion of the stock solution was transferred to a new vial, where the solvent was evaporated. Various solvents were used to dissolve the material and achieve the desired final concentration, typically around 10^{-6} M. The solvents used in this study include methylcyclohexane (MCH), toluene (PhMe), 2-methyl tetrahydrofuran (2MeTHF) and dichloromethane (DCM). Note that low concentrations (about 10^{-6} M) were used for mostly spectroscopic measurements to avoid intermolecular interactions.

3.2.2 Degassing solutions

As discussed earlier in section 2.3, the presence of oxygen can lead to quenching mechanisms that significantly impact long-lived species, particularly triplet excited states. Hence, conducting measurements in oxygen-free solutions is crucial for studying the TADF mechanism. To remove all dissolved oxygen within the solution, degassed solutions were obtained through 5 freeze-pump-thaw cycles.[99]

3.2.3 Films

Films were mainly prepared by drop casting methods. In this approach, a solution of 100-200 μL was dropped onto sapphire or quartz substrates, which was left under vacuum, allowing the solvent to evaporate and producing a solid film. The neat films were produced from a solution of the emitter molecules in PhMe at a concentration of 1 mg/mL. On the other hand, the host-guest films were formed by blending two solutions: one containing the emitter molecules and another containing the host molecules. When zeonex was used as the host molecule, the solution concentration of the emitter in PhMe remained at 1 mg/mL, while the concentration of zeonex in PhMe was 100 mg/mL. In the case of using small molecules such as UGH and DPEPO as hosts, the solution concentration of the emitter in chloroform ($CHCl_3$) was 1 mg/mL, while the concentration of these hosts in chloroform was 10 mg/mL. The host-guest films were therefore, obtained by combining the host and emitter solutions in different proportions, resulting in varying concentrations, typically 1% and 10% in this study.

3.3 Experimental Methods

This section will provide a description of the techniques utilised, highlighting important aspects of the experimental setups. A range of optical spectroscopy techniques were employed in this thesis due to the complex photophysical properties exhibited by these highly-efficient emitter molecules.

3.3.1 Steady-state measurements

Steady-state techniques are the first category of measurements to be discussed here. These techniques comprise a range of measurements that utilise a continuous-wave light source, such as UV-vis absorption, photoluminescence, excitation profile and photoluminescence quantum yield measurements. The main goal of employing these techniques in this thesis is to identify the main excited states of the molecules, assess their

emission efficiency and investigate the formation of new luminescence species such as dimers/excimers.

3.3.1.1 UV-vis absorption spectroscopy

UV-vis absorption spectroscopy is an experimental technique that measures the efficiency of light absorption by a material at specific wavelengths (λ).[37] The spectrometer measures the reduction in the flow of photons within the optical beam as it passes through the sample, in comparison to the reference beam. Therefore, the absorbance A(λ) can be defined as in the equation (3.1):[45]

$$A(\lambda) = \log \frac{I_\lambda^0}{I_\lambda} = -\log T(\lambda) \quad (3.1)$$

where I_λ^0 and I_λ are the intensities of the beam passing through the reference and the absorbing medium, respectively, and $T(\lambda)$ represents the transmittance of the light.

Importantly, the absorption of the materials follows the Beer-Lambert law (equation (3.2)):

$$A(\lambda) = \varepsilon(\lambda) l c \quad (3.2)$$

where $\varepsilon(\lambda)$ is the molar absorption coefficient (M^{-1} cm^{-1}), c is the concentration (M) and l is the absorption path length (cm).

In this study, the absorption spectra were acquired using a Shimadzu model UV3600 double beam spectrophotometer, equipped with a reference beam and a sampling beam that traversed the sample. All spectra were recorded at room temperature under atmospheric conditions.

3.3.1.2 Photoluminescence spectroscopy

Photoluminescence spectroscopy is a technique that enables the measurement of the light emitted by a material when it is excited with a specific wavelength. After the excitation, the material emits light, resulting in an emission spectrum.[84] The spectrometer often consists of two monochromators: the first one is positioned before the sample to select the excitation wavelength, and another (positioned after the sample) for selecting the emission wavelength. Additionally, a photomultiplier detector is used to obtain the spectral wavelength and intensity of the emitted light. In this study, the photoluminescence (PL) spectra were recorded using FluoroLog fluorescence spectrometer (Jobin Yvon) or a matrix spectrometer QePro (Ocean

Optics). In these systems, spectra can be recorded under various conditions, including air and degassed solutions, different temperatures, solid films, vacuum or air environments.

3.3.1.3 Excitation spectra

The excitation spectrum represents variations in the emission intensity resulted from different excitation wavelengths when collected at specific wavelength. The excitation spectrum can exhibit identical characteristic to the absorption spectrum. However, in the presence of species that are exclusively formed in the excited state, such as excimers, the excitation and absorption spectra may differ from each other.[37] Consequently, the excitation spectrum provides valuable insights into the materials. Apart from detecting excimer species, excitation spectra can also identify very weakly absorbing transition bands, such as the direct CT absorption. This measurement is obtained using a feature of the FluoroLog fluorescence spectrometer from Jobin Yvon.

3.3.1.4 Photoluminescence quantum yield (PLQY)

The photoluminescence quantum yield is determined by the ratio of the number of emitted photons to the number of absorbed photons. This parameter can be obtained in both solution and solid films, as described below:

i. PLQY in solutions:

The approach utilised to derive the PLQY in a solution involved employing a relative method that relies on a standard compound with a "known" PLQY. Typically, a series of the fluorescence intensity (integrated area under the whole emission spectra) is recorded as function of the absorption at the specific wavelength for the sample (indexed as X) and the standard compound (indexed as S). These measurements create a gradient curve (Δ), which is subsequently compared and adjusted for differences in refractive index (n) if the sample and standard compound were measured in different solvents. The equation (3.3) used to estimate the PLQY is shown below:[84]

$$\phi_X = \phi_S \frac{\Delta_X}{\Delta_S} \frac{n_X^2}{n_S^2} \tag{3.3}$$

where ϕ is the PLQY value of the sample (ϕ_X) and the standard compound (ϕ_S).

For a more accurate determination of the PLQY value, a gradient curve is generated by measuring the emission and absorption at 4-5 different concentrations. It is important to note that this approach is applicable within a linear concentration range, and the compound's

absorbance at the excitation wavelength should remain below 0.1 in order to avoid reabsorption effects and intermolecular quenching.[100] Additionally, it is crucial to maintain consistent settings for all the measurements. Absorption and emission were recorded as described above. The measurements are conducted in an air-equilibrated environment, however due to the presence of long-lived species in TADF, determining PLQY in degassed solutions is crucial. To achieve this, the emission spectra were recorded in both degassed and air-equilibrated solutions. Subsequently, the ratio between the integrated areas of these two spectra is multiplied by the PLQY value obtained in the air-equilibrated solutions.

ii. PLQY in solid film:

The absolute PLQY of the solid film was measured using a calibrated integration sphere (Horiba Quanta-ϕ) connected to a Horiba Fluorolog-3 spectrofluorometer. To ensure an oxygen-free environment, the integration sphere was purged with dry nitrogen gas for 30 minutes. The equipment used is housed within the Chemistry Department facilities at Durham University.

3.3.2 Time-resolved photoluminescence measurements

Time-resolved photoluminescence measurements are widely used as a powerful tool for investigating the molecular dynamics of fluorophores. In contrast to steady-state measurements, these advanced optical spectroscopies provide valuable insights into the temporal behaviour of the emitted light, defining the lifetime. The lifetime is a distinct and intrinsic molecular parameter that can be utilised to investigate electronic transitions and the dynamics of the excited state.[37] In this study, two main techniques were employed: time-resolved gate spectroscopy and time-correlated single photon counting. These advanced optical spectroscopies were used in this thesis to study the temporal behaviour of the emitted photons, providing valuable information about these energy-efficient emitter molecules, such as excited state lifetimes, energy transfer, rates constants, and other parameters.

3.3.2.1 Time-resolved gate spectroscopy (iCCD)

Time-resolved gate spectroscopy enables the acquisition of spectra at various time intervals after the excitation. Essentially, a pulsed laser excites the sample, which then emits light. Subsequently, the emitted light is collected by the detector, which opens and closes its electronic shutter at different time intervals, from a few nanoseconds to seconds.

Basically, the system comprises a pulsed laser, monochromator and a gated intensified charge coupled device (iCCD) camera. As excitation sources, there are two main lasers coupled in this system: a pulsed Nd:YAG laser, emitting at 355/266 nm with a pulse width of 150 ps (FWHM), and a nitrogen laser, emitting at 337 nm with a pulse width of 3 ns (FWHM). After the excitation, the emitted photons from the sample are focused into a spectrograph equipped with a 300 lines/mm grating, then directed onto a sensitive gated intensified charge coupled device (iCCD) camera from Stanford Computer Optics. The synchronisation between the iCCD camera and laser depends on the laser used. For the Nd:YAG laser, the synchronisation is achieved through an electrical pulse, while in the case of the nitrogen laser, a portion of the excitation beam is directed to a photodiode, which then sends electrical pulses to the iCCD. These two setup designs are represented in Figure 3.1.

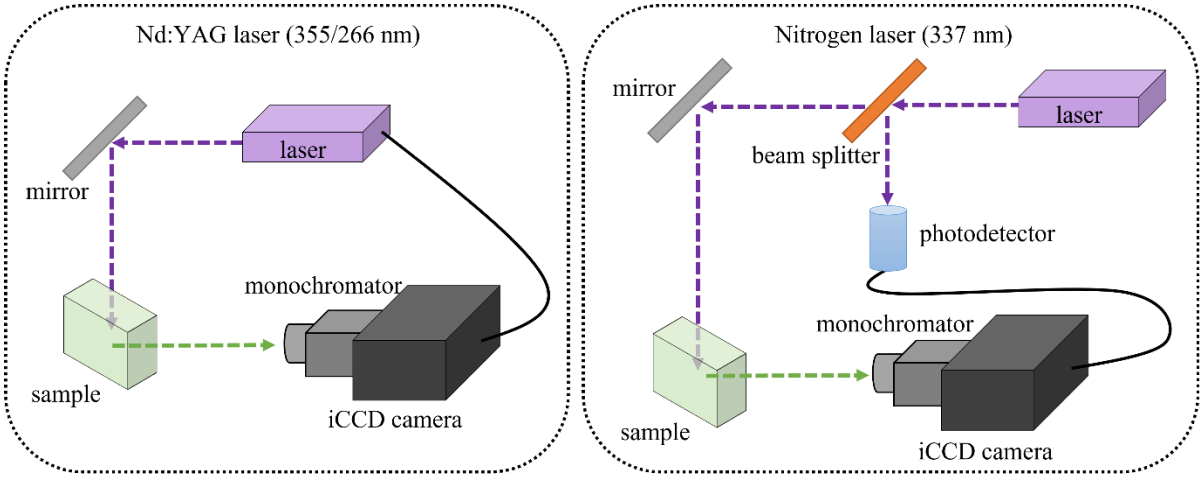

Figure 3.1: Schematic representation of the time-resolved gate spectroscopy setup for both configuration, using the Nd:YAG and the nitrogen laser.

The 4 PICOS camera software allows the control of parameters such as delay time (the time the camera shutter opens) and integration time (how long the shutter remains open to accumulate signal). Data collection occurs using logarithmically increasing delay and integration times, covering the desired time range, and enabling to build a decay curve. Figure 3.2 shows a decay curve obtained from this technique, with each data point representing the integrated area of each spectrum. Note that it is possible to choose any part of the full collected spectrum. Therefore, if the full spectrum is integrated, all species lifetimes can be estimated. However, by integrating a specific area of the spectrum (under a specific feature) the lifetime of that specific species/feature can be obtained. By using this setup, measurements can be recorded under various conditions, including air and degassed solutions, different temperatures, solid films, vacuum or air environments.

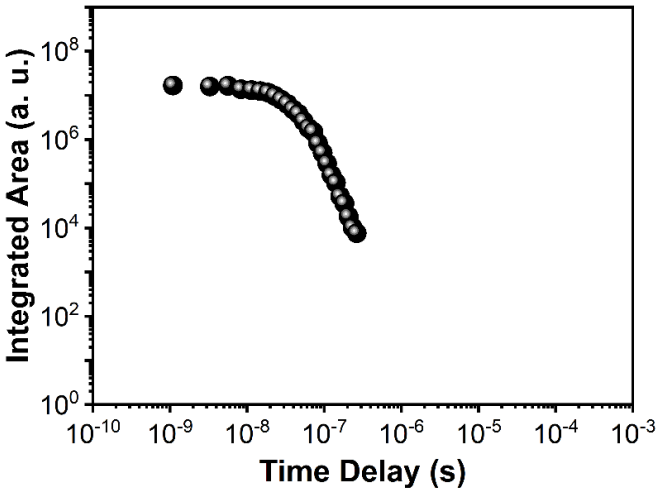

Figure 3.2: Example of decay curve obtained from this technique, where each data point represents the integrated area of each spectrum.

Delayed fluorescence can arise from either a monomolecular process, as in TADF mechanism, or a bimolecular process, such as triplet-triplet annihilation. Therefore, analysing the DF integrated intensity as function of the excitation dose helps to identify the origin of the DF, *i.e.* TADF or TTA mechanism. In such a power dependence plot, the slope of 1 corresponds to a monomolecular, TADF mechanism, while slope of 2 suggest a bimolecular process, as TTA mechanism. It is worth mentioning that experimentally, at low excitation doses, the TTA mechanism shows a slop close 2, turning to slope close to 1 at high excitation doses.[43] This is ascribed to the effect of dispersive migration of the triplet population.[101] To perform this measurement, a variable filter wheel was used, which was manually controlled and positioned in front of the nitrogen laser, emitting at 337 nm. This filter wheel allowed the control the laser power reaching the sample. A single spectrum was collected at various excitation dose, and the measurement parameters were adjusted to collect the spectra that integrates the entire DF regime. In this technique, it is also possible to collect spectra that integrate over different time regimes. As a result, by collecting power dependence at various time regimes, multiple process can be studied independently.

3.3.2.2 Time-correlated single photon counting (TCSPC)

The TCSPC technique is widely recognised for its high sensitivity in determining lifetimes. Broadly speaking, the technique records the arrival times of individual photons in a specific wavelength followed by the optical excitation of a sample. A pulsed excitation source generates a start pulse in the timing electronics. Subsequently, a "stops" pulse in the timing electronics is triggered by the detection of an emitted photon. The time difference between

these two signals represents a count. Therefore, by repeating the excitation-emission process is repeated multiple times (up to 10000 counts in the peak channel), builds up a histogram that correlates the counts with respect to time.[45]

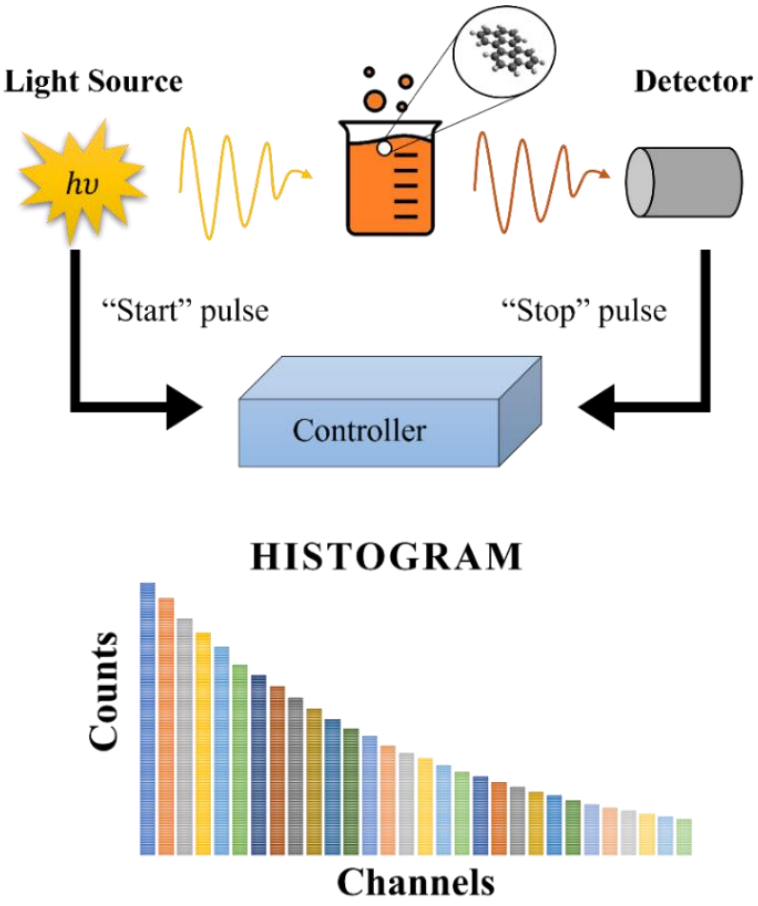

Figure 3.3: Schematic representation of TCSPC setup and histogram generated from this measurement. Adapted from Horiba Scientific.[102]

The setup includes excitation sources, usually lasers or LEDs, a monochromator, and a photon detector integrated with a photomultiplier tube. One of the key factors influencing the effective resolution of a TCSPC system is its instrument response function (IRF). The IRF contains valuable information about the pulse shape of the excitation source and the temporal dispersion within the optical system, for example.

In this study, the equipment used was a Horiba DeltaFlex TCSPC system coupled with various excitation sources, such as a 330 nm SpectraLED, a 357 nm NanoLED, and a 405 nm DeltaDiode light source. This setup also allows the measurements to be recorded under various conditions, including air and degassed solutions, different temperatures, solid films, vacuum or air environments.

3.3.3 Pump-probe techniques

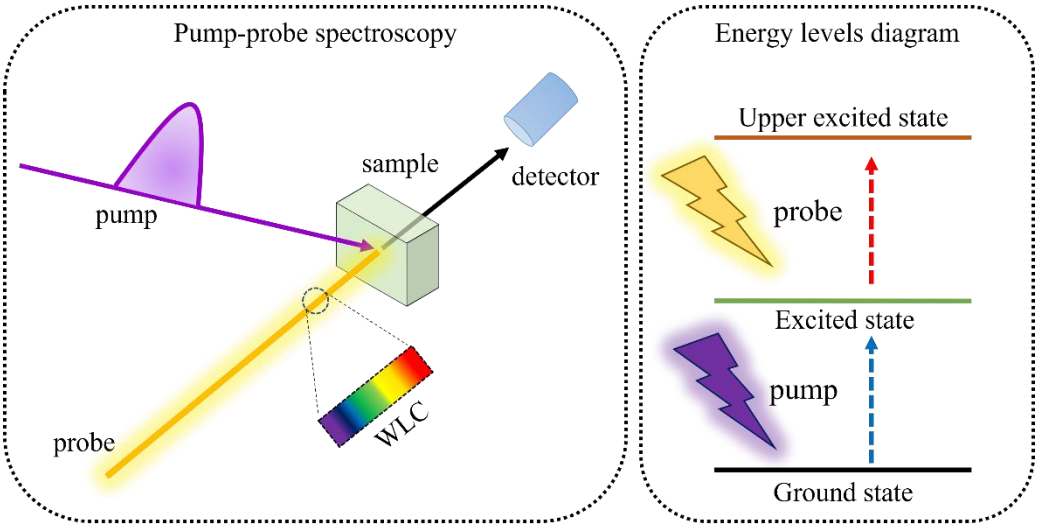

Figure 3.4: Pump-probe spectroscopy: schematic representation of the experimental setup (left) and the energy levels diagram representing the electronic transitions involved in the experiment (right).

Pump-probe spectroscopy is another powerful tool to study the dynamic of the excited state. This technique is widely use to study a range of applications in photonics and optoelectronics. Importantly, this technique offers a unique advantage of investigating both emissive and non-emissive excited states, providing crucial insights into the radiative and non-radiative processes of molecules. A simplified pump-probe setup comprises two light sources: a high-energy laser pulse, known as the pump, to populate the molecules' excited state, overlapped with a synchronised weak white light source that probes these excited states. In principle, this technique measures changes in the transmittance signal (T), detecting the transmittance before and after the laser/pump pulse (ΔT), giving rise to signals that is then defined as $\Delta T/T$. There are two main modes for this technique: (i) spectrograph mode: where absorption spectrum of the excited state is recorded; (ii) kinetic mode: where the absorption at specific wavelength is recorded as function of time. Another important feature of the experimental setup is the duration of the laser pulses, this will determine the time resolution of the measurement.[84] This thesis employed three different pump-probe setups: quasi-CW photoinduced absorption and transient photoinduced absorption with nanosecond (nsTA) and femtosecond (fsTA) time resolutions. The primary goal of conducting measurements using these techniques for this thesis was to gain information and insights into dark excited states involved in the TADF process, such as the ^{3}CT excited state.

3.3.3.1 Quasi-CW photoinduced absorption

The quasi-CW photoinduced absorption measurements utilise as a probe source a broadband output of a laser driven white light source (Energetiq EQ-99). This light source is focused on an aluminium parabolic mirror (Thorlabs) generating a spot of ~ 4 mm diameter on the 1 cm sample cuvette. The pump source is a 375 nm laser pump beam (Vortran Stradus 375-60) modulated at 173 Hz, which is carefully aligned to overlap with the probe source. The probe beam then passed through a Bentham TM300 monochromator and is detected by either a Si (Hamamatsu) or InGaAs photodiode detector (FEMTO PWPR-2K-IN-FS). The output from the detector is connected to the Signal Recovery dual channel 7225 digital lock-in amplifier, which not only collect the signal but also provides the reference frequency modulation for the pump laser. The phase of the lock-in amplifier was set in the PL signal.

3.3.3.2 Nanosecond transient photoinduced absorption (nsTA)

Guided by the photoinduced absorption spectra obtained by Quasi-CW photoinduced absorption technique, nanosecond kinetics and the absolute signs of the induced absorption signals were determined at wavelengths of interest. The probe source utilised for this setup was the same laser driven light source (Energetiq EQ-99). However, the pump source used for this measurement is a Nd:YAG laser (EKSPLA, ~ 150 ps pulse length, 355 nm, 10 Hz repetition rate). The pump source was also aligned with this probe beam spot in a quasi-coaxial beam path, passing directly from the sample into a beam dump. The transmitted probe beam was refocussed into the monochromator and measured by either a balanced Si (Femto HBPR-200M-30K-Si) or single-element InGaAs (Femto HCA-S-200M-IN) photodiode. The diode output was optionally amplified (Femto DHPVA-201) and read using an oscilloscope (Agilent Infiniium 1 GHz) triggered by the pump laser.

Significant oscillations of the probe beam are detected for measurements at visible wavelengths. To minimise the oscillation signals, a balanced Si diode was used. One signal was collected from the monochromatic probe beam emerging from the sample (after sample), while another signal was collected as a portion of the pre-sample (before sample) probe beam. With the pump beam blocked, the portion of the pre-sample probe beam was reflected from a quartz plate to a variable filter wheel. This filter wheel was connected to an optical fibre to generate the second channel signal. The purpose of the filter wheel was to balance the intensities of the probe beam before and after the sample. By matching these intensities, a balanced output was achieved, effectively cancelling out the oscillations originating from the probe beam. With the pump beam then unblocked, the transient absorption signal could be

collected (pump and probe). Emission from the sample was then also collected using the same oscilloscope settings by simply blocking the probe beam (pump-only). Pump-only measurements are essential and can be utilised for corrections and background subtraction. Although this thesis exclusively measured the pump-only signal using this nsTA technique, it can be highly beneficial to also measure pump-only signals using the other photoinduced absorption techniques for correction purposes, including the Quasi-CW photoinduced absorption technique.

3.3.3.3 Femtosecond transient photoinduced absorption (fsTA)

Femtosecond resolution transient photoinduced absorption allows to the study of very fast processes, such as internal conversion, solvent reorganisation, vibronic relaxation. The setup for this measurement uses the same laser source to generate both, the pump and probe pulse, which with an optical delay it is possible to control the time interval between these two pulses. The laser utilised in this setup was PHAROS from Light Conversion (wavelength: 1030 nm, pulse duration: 180 fs). To generate the pump pulse, part of the output is used to do third harmonic generation (THG), which produces a 343 nm output and is used to pump the samples. Another part of the original laser (1030 nm wavelength) output passes through a computer-controlled delay line formed by a mobile platform with a hollow retroreflector and then is focused on 2 mm sapphire plate to generate a white light continuum (WLC). This WLC is used to probe the dynamics of the excited states. The WLC probe and the pump beam reaches the sample almost collinear with each other, within a small angle between them. After passing through the sample, the probe beam is sent into a home-made spectrometer, which is using a CMOS detector. The delay line and the CMOS detector are computer-controlled, and the temporal window of this experiment is about 6000 ps.

3.4 Data processing

This section will briefly describe of the main methodologies employed to process the data and extract important parameters to necessary to a deeper understanding of the highly-efficient emitter molecules.

3.4.1 Obtaining the state's energy and ΔE_{ST}

The energy of each state is determined through the absorption and emission spectra of the electronic transition associated with it. From the absorption and emission spectra, the energy is determined through the onset of the spectrum. To achieve a reliable estimation of the

ΔE_{ST} from the spectra, time-resolved photoluminescence spectra of the molecule is recorded at room and low temperature. Thus, the singlet excited state energy is obtained from the onset of the time-resolved photoluminescence spectra at room temperature (in the first few nanoseconds). While the triplet excited state energy is obtained from the onset of the time-resolved photoluminescence spectra at low temperature (typically around 80 K), at longer times (around 80 ms). The choice of utilising the onset of these bands is because emission bands in TADF molecules typically exhibit a Gaussian band shape, making it challenging to accurately define the peak. Figure 3.5 shows an example of determining a ΔE_{ST} by analysing the onset of the spectra of an emitter molecule.

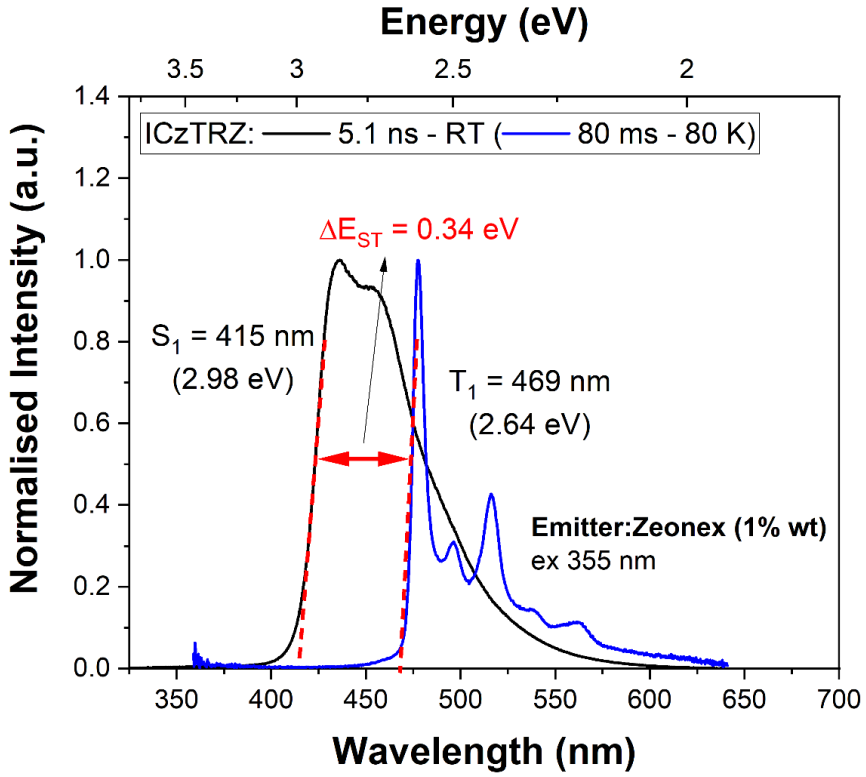

Figure 3.5: Example of determining the ΔE_{ST} value from onset of time-resolved photoluminescence spectra of the emitter molecule (ICzTRZ) in a zeonex matrix (1% concentration). Singlet excited state was estimated from the onset of the spectrum at 5.1 nanosecond, recorded at room temperature (RT, black curve). Triplet excited state was estimated from the onset of the spectrum at 80 milliseconds, recorded at low temperature (80 K, blue curve). λ_{exc} =355 nm.

3.4.2 Determining lifetimes and decay rates

Decay lifetimes are described by exponential functions, either monoexponetial (as shown in equation (3.4)) or multiexponential functions depending on the goodness of the fit. The goodness of the fit was assessed using the *Adjusted R^2* parameter. *Adjusted R^2* is statistical measure used to assess the accuracy of the regression line in approximating the actual data. Three main software were used to fit these decay traces: OriginPro 2020, MagicPlot Pro and DecayFit Fluor Tools (mainly used for short lifetimes obtained from TCSPC data).

$$y = A \times e^{-\frac{x}{t}} \tag{3.4}$$

where t correspond to the lifetime and A is its contribution or amplitude. For multiexponential functions, the monoexponential equation (3.4) can be adjusted as follows:

$$y = A_1 \times e^{-\frac{x}{t_1}} + A_2 \times e^{-\frac{x}{t_2}} \tag{3.5}$$

From the decay lifetimes and their amplitudes, it is possible to estimate crucial rate constants related to the TADF mechanism, including the ratio of the delayed fluorescence (DF) and prompt fluorescence (PF) decay (DF/PF), prompt fluorescence quantum yield (ϕ_{PF}), radiative rate constant (k_F), intersystem crossing (k_{ISC}) and reverse intersystem crossing rates (k_{rISC}). Therefore, these parameters were estimated according to the equations shown below, the subscripts relate the parameter to the DF or PF components:[43]

$$DF/PF = \frac{\int_0^\infty y_{DF}(t)\,dt}{\int_0^\infty y_{PF}(t)\,dt} = \frac{A_{DF} \times t_{DF}}{A_{PF} \times t_{PF}} \tag{3.6}$$

Assuming that $\phi_{PL} = \phi_{PF} + \phi_{DF}$ = 1, it is possible to obtain the following equation for ϕ_{PF}:

$$\phi_{PF} = \frac{1}{1 + (DF/PF)} \tag{3.7}$$

$$k_F = \frac{\phi_{PF}}{t_{PF}} \tag{3.8}$$

Assuming that ISC is the only non-radiative process from the singlet state (S_1), the k_{ISC} can be estimated as:

$$k_{ISC} = \frac{(1 - \phi_{PF})}{t_{PF}} \tag{3.9}$$

Finally, assuming that rISC quantum yield (ϕ_{rISC}) is ≈1

$$k_{rISC} = \frac{(1+ DF/PF)}{t_{DF}} \tag{3.10}$$

A second similar approach was used to extract these rate constants from the time-resolved photoluminescence decay which is based on *Haase et al.* simplified kinetic model.[103] In this simplified model, instead of employing a complex four-state model to describe the TADF mechanism, it considers one mixed triplet excited state – acting as the lowest lying triplet state – and the singlet CT excited state. In developing this model, specific assumptions were taken into account. Among these assumptions is the absence of non-radiative decays from singlets and triplets excited states, as well as the lack of radiative decay from the triplet excited states (no phosphorescence).

3.4.3 Arrhenius plot

Beyond analysing spectra features, an alternative method to determine ΔE_{ST} involves the Arrhenius type of plot. This plot is generated from the temperature dependence time-resolved photoluminescence decay, resulting a graph of the lifetime as function of the temperature. Through this plot, an activation energy can be estimated, which in many cases are correlated with the ΔE_{ST}. The equation used to fit the experimental data and obtain the activation energy (E_a) is provided below as equation (3.11). This equation is based on a simplified model proposed by *Yersin et al.*[104]

$$y = \frac{(3 + e^{\frac{a}{x}})}{\frac{3}{b} + c \times e^{\frac{a}{x}}} \tag{3.11}$$

In the equation, the fitted parameter a represents the ratio of the activation energy (E_a) divided by the Boltzmann constant (k_B), where k_B assume the value of $8.61 \times 10^{-5}\ eV\ K^{-1}$. Additionally, the fitted parameters b and c correspond to the intrinsic decay lifetime of the triplet state and the radiative rate constant (k_F), respectively.

As mentioned in the section 2.2.4, the activation energy equation is simplistic in describing rISC rates, as it does not account for the second-order perturbation theory. Therefore, important coupling interaction, such as spin-orbit coupling, vibronic coupling, and hyperfine coupling, that critically affect the rISC rate and the ΔE_{ST}, are not considered. However, this equation needs to be used carefully to ensure that it can describe the observed TADF mechanism.

3.4.4 Precision and error analysis

Precision and errors in the analysis play an important role in facilitating comparison between different sets of data, which relies on several factors, ranging from instrumentation, (*e.g.* slits, steps, detectors and lasers pulses) to human factors. In this thesis, discussion on precision and errors revolves around determining the wavelength (λ) in spectra and lifetimes.

To determine the λ in absorption and emission spectra (*e.g.* peaks, onsets), based on the settings used, it is assumed that differences above 2 nm are considered distinguishable. These differences translate into errors in energy (E, in eV) and can be determined using the partial derivative method, as shown in the equation below:

$$\sigma_E = \left|\sigma_\lambda \frac{\partial E}{\partial \lambda}\right| = \left|-\sigma_\lambda \frac{hc}{\lambda^2}\right| \tag{3.12}$$

where σ is the uncertainty of the variable, such as E and λ. For example, in the case of 500 nm, the uncertainty in energy is 9 meV.

Moreover, when determining lifetimes, it is assumed that 1 significant digit in the lifetime is certain; for example, for a lifetime of 2.3 ns, the error is 0.1 ns.

4 Probing emissive excited states: unrevealing the critically decoupled nature of a TADF molecule

This chapter focuses on the highly complex photophysics exhibited by spiro TADF molecules. Spiro compounds possess distinctive molecular photophysics due to their rigid and orthogonal spiro carbon bridging bond between donor and acceptor. Firstly, I will present steady-state and time-resolved optical spectroscopy to uncover multiple excited state emissions. As the spiro bridges critically decouple the donor and acceptor units, they create numerous channels for radiative decay, including (dual) phosphorescence, and the molecular charge transfer (CT) states giving rise to TADF, where the outcome of which depends on the excitation wavelength. Subsequently, I will explore the two main channels for the TADF mechanism, where the local acceptor nπ* states play an important role.

The work presented in this chapter has been already published:

i. Franca, L. G.; Danos, A.; Monkman, A. Donor, Acceptor, and Molecular Charge Transfer Emission All in One Molecule. *J. Phys. Chem. Lett.* **2023**, *14* (11), 2764–2771.
ii. Franca, L. G.; Long, Y.; Li, C.; Danos, A.; Monkman, A. The Critical Role of nπ* States in the Photophysics and Thermally Activated Delayed Fluorescence of Spiro Acridine-Anthracenone. *J. Phys. Chem. Lett.* **2021**, *12* (5), 1490–1500.

4.1 Overview:

This chapter introduces the study of an exemplar spiro compound, the spiro-linked acridine−anthracenone derivative, known as 10-phenyl-10H,10′H-spiro[acridine9,9′-anthracen]-10′-one (**ACRSA**; the molecular structure is shown in Figure 4.1). **ACRSA** was one of the first reported spiro-linked TADF materials,[105] displaying high photoluminescence efficiency of 85% in solution, and good OLED performance doped in the host bis[2-(diphenylphosphino)phenyl] ether oxide (DPEPO), achieving an external quantum efficiency (EQE) of 16.5%.[106] It is worth noting that this device performance is lower than expected, especially when compared to the up to 25% EQE achieved by C–N linked D–A molecules.[107] This differences hinted that a distinct photophysics may be associated with the presence of the C–C spiro-bridge, warranting the need for further investigation.

Another reason that drew attention to **ACRSA** is that Lyskov and Marian had already published a highly detailed quantum chemistry analysis for this molecule.[108] Their work highlighted the complex interactions between charge transfer and local states, resulting in strong state mixing (including high-lying excitonic transitions) that overcomes the typically

forbidden radiative decay from these states. Furthermore, the calculations also suggested a potential for rapid nanosecond rISC mediated by n→π* to π→π* transitions.

Thus, the objective of this research was to conduct a range of spectroscopic measurements of **ACRSA** in solution, especially the time-resolved optical spectroscopy, aiming to uncover the highly complex photophysics. Due to the critically tuned electronic decoupling of **ACRSA** enforced by the rigid spiro D−A bridging bonds, the photophysical behaviour of the molecule corresponds to either the donor or acceptor subunit, as well as the full molecular CT state, dependent on the excitation wavelength. This suggests that the spiro D−A system could potentially exhibit charge transfer states that are predominantly intramolecular through space in nature, rather than through bond.

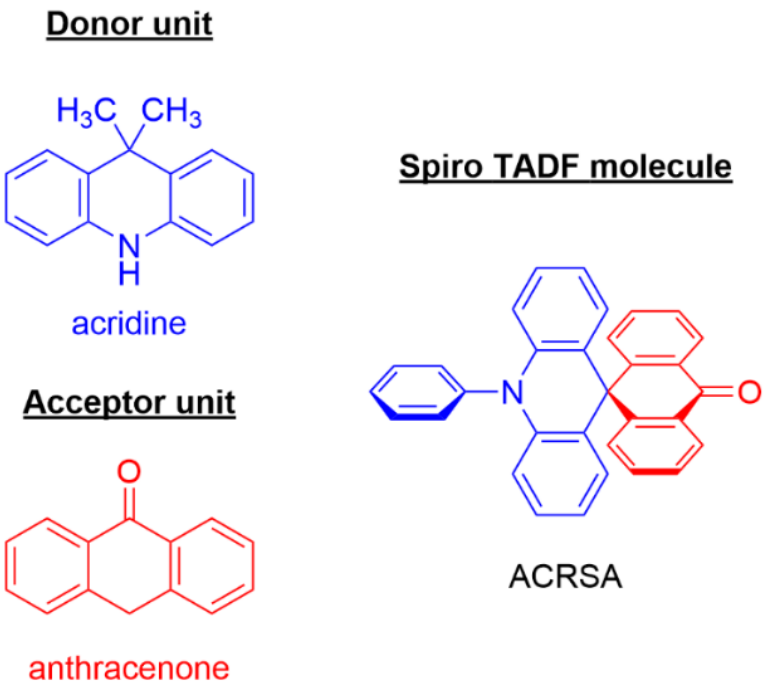

Figure 4.1: Molecular structure of the 9,9-dimethyl-9,10-dihydroacridine (acridine, donor unit), 9(10H)-anthracenone (anthracenone, acceptor unit) and the 10-phenyl-10H,10′H-spiro[acridine9,9′-anthracen]-10′-one (**ACRSA**, spiro TADF molecule).

4.2 Results and Discussion:

4.2.1 Dependence of singlet excited states on the excitation wavelengths:

Figure 4.2 shows the optical absorption spectra of **ACRSA** in a toluene solution (at 50 µM). The absorption spectrum presents two main bands in the ultraviolet (UV) ($\varepsilon > 10^4$ M^{-1} cm^{-1}), which theoretical calculations[108] identified as a pair of π→π* transitions: 1^1B_1 at 341 nm (3.63 eV) and 2^1B_2 at 324 nm (3.82 eV).

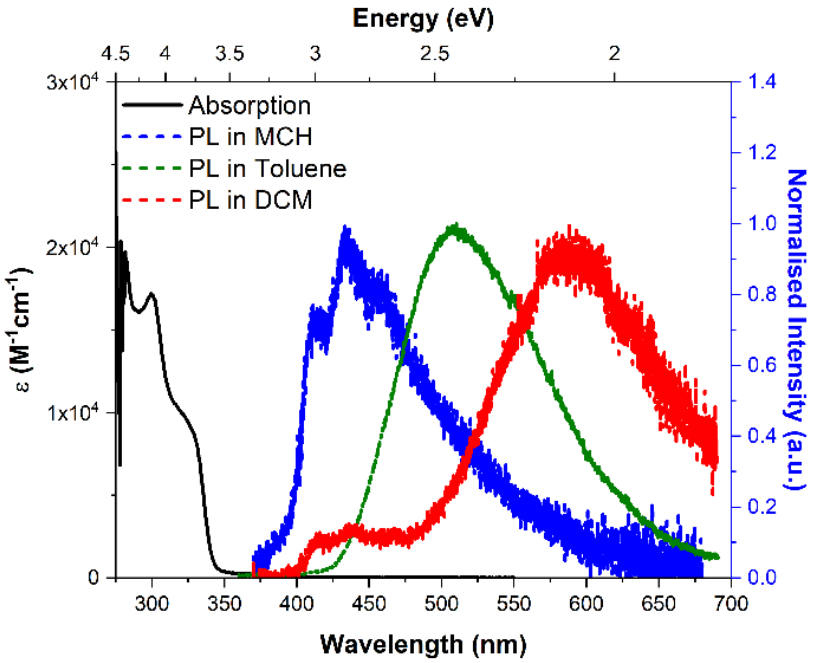

Figure 4.2: Steady-state absorption (solid line) of **ACRSA** in toluene solution (air-equilibrated, at 50 μM concentration); and photoluminescence (dashed lines; λ_{ex} = 350 nm) spectra of **ACRSA** in solvents indicated in the figure legend (degassed solutions, at 50 μM concentration) at room temperature.

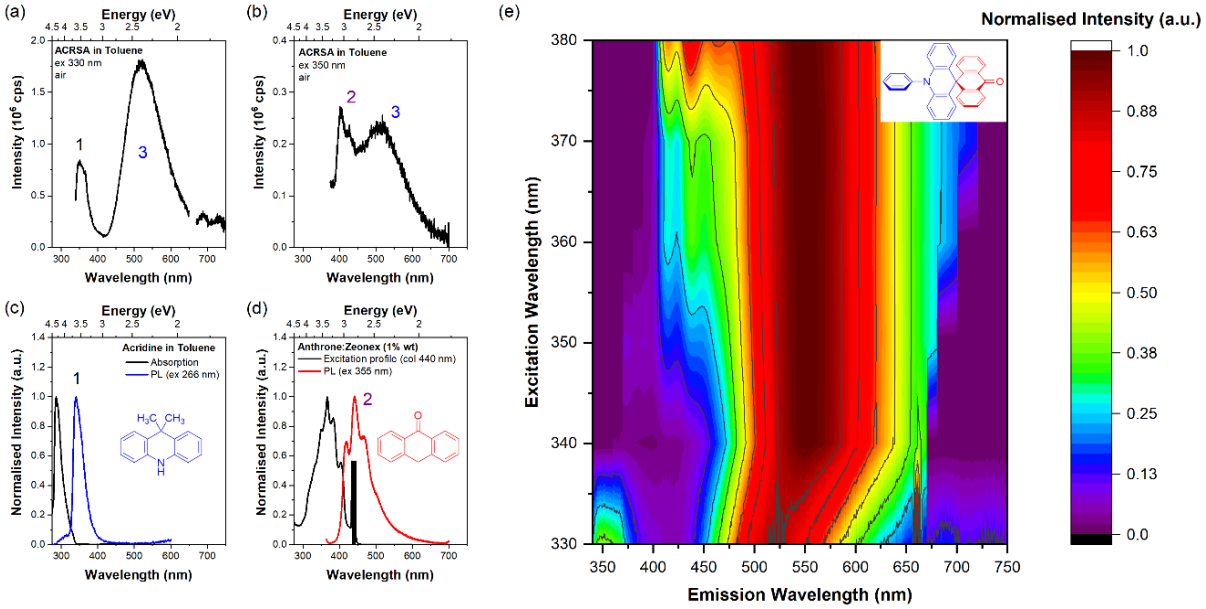

Figure 4.3: Photoluminescence (PL) spectra of **ACRSA** in toluene (air-equilibrated, 50 μM), with excitation at (a) 330 nm and (b) 350 nm. (c) Absorption and PL spectra of the acridine unit (donor unit) in toluene. (d) Excitation and PL spectra of the anthracenone unit (acceptor unit) in the zeonex matrix at 1 wt % concentration, with excitation collected at 440 nm marked with a black line. (e) Contour plot was interpolated from PL spectra of **ACRSA** in toluene (air-equilibrated, 50 μM), exciting at different wavelengths.

To compare the absorption and emission features of **ACRSA**, the experimental absorbance and excitation spectra of acridine (donor) and anthracenone (acceptor) units, along with their photoluminescence spectra, were measured (Figure 4.3). The acridine unit absorbs at 337 nm (3.7 eV) and emits a characteristic UV emission around 350 nm (3.5 eV), identifying the 1^1B_1 state in **ACRSA** as corresponding to the $\pi \rightarrow \pi^*$ transition from the D. The excitation

profile of the anthracenone (acceptor unit) shows absorption in the range of 300−400 nm (Figure 4.3d), and its emission exhibits a well-structured band at wavelengths above 400 nm, similar to that observed from **ACRSA** when excited at 355 nm. This identifies the n→π* transition of A, ascribed as a 2^1A_1. Moreover, the 2^1B_2 state is a contribution of the anthracenone π→π* state.

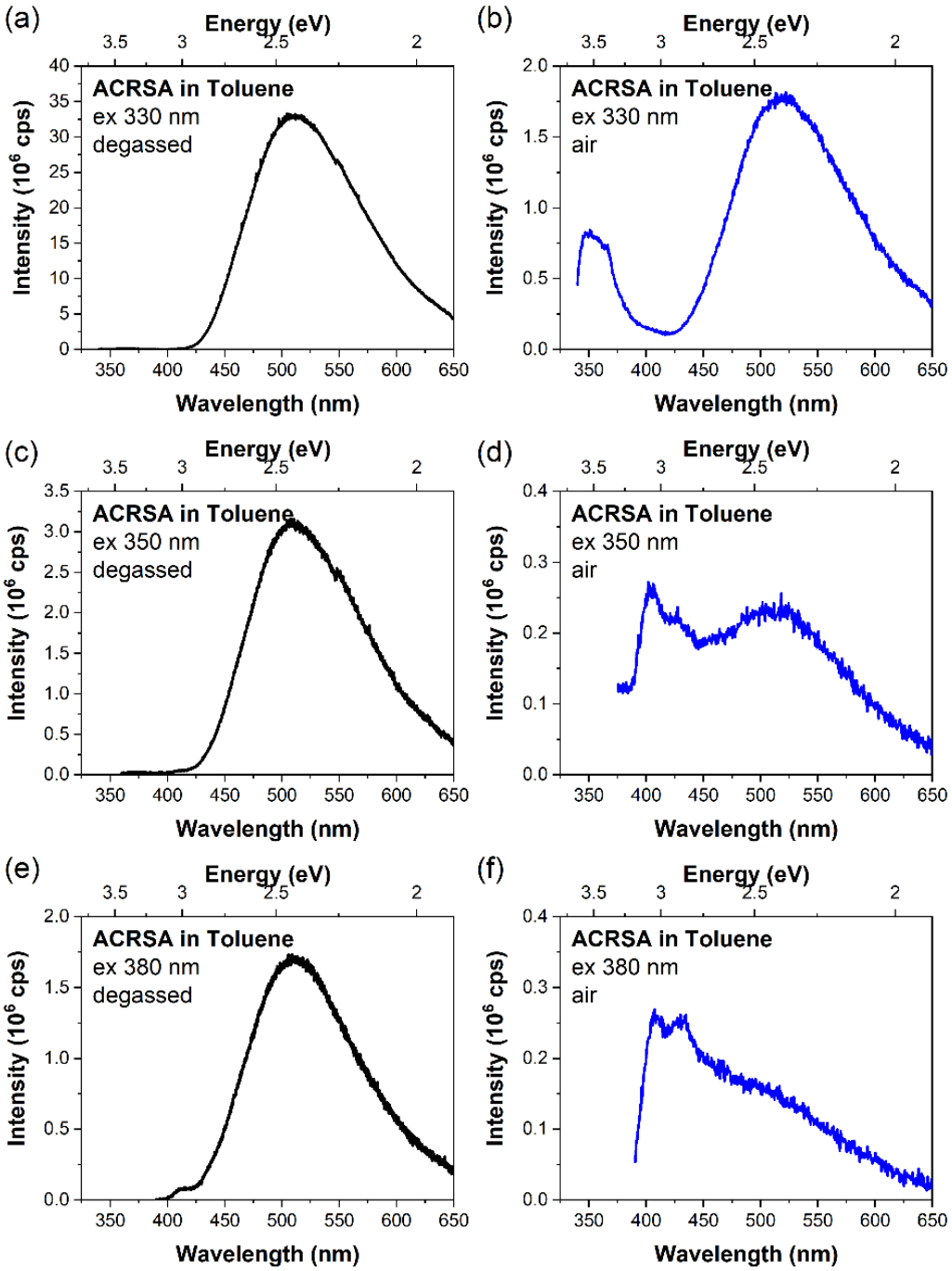

Figure 4.4: Photoluminescence (PL) spectra of **ACRSA** in degassed and air-equilibrated toluene solution (with a concentration of 50 µM), excitation at (a) 330 nm, (b) 350 nm and (c) 380 nm.

In addition to the contributions from the D and A contributions, the emission spectra of **ACRSA** exhibit a pronounced Gaussian-shaped emission at 500 nm when excited at either 330 or 350 nm. This emission is indicative of a CT state (Figure 4.3 a and b). The full excitation-dependent emission is shown in the contour plot (Figure 4.3e). The CT nature of the Gaussian emission at 500 nm in toluene is confirmed by its strong solvatochromism (Figure 4.2).

Figure 4.4 shows the photoluminescence spectra obtained from both degassed and air-equilibrated toluene solution, exciting at different wavelengths. Upon removing dissolved oxygen, a tenfold increase in the PL intensity is observed. This indicates a highly efficient rISC of triplets through this CT state. Indeed, it is only through the presence of oxygen quenching of the DF CT band that it becomes possible to distinguish the considerable weaker emission band of the donor or acceptor (Figure 4.4). The donor and acceptor emission bands are situated beneath the ^{1}CT contribution. In the degassed environment, emission is predominantly from the ^{1}CT band, facilitated by efficient rISC harvesting of the triplet states. Therefore, with the addition of oxygen, the DF (rISC) mechanism is quenched, allowing for the identification of the weak emission signals coming from both donor and acceptor units. Otherwise, these signals are hidden by the strong DF CT emission.

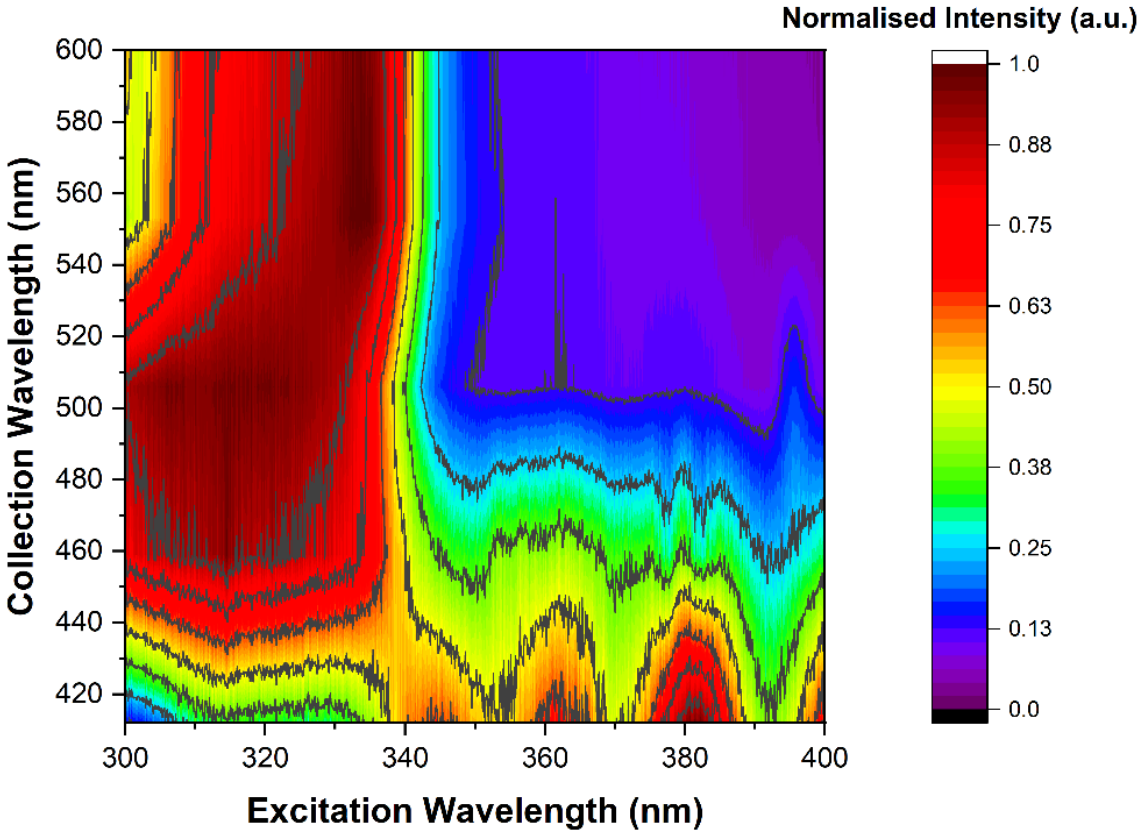

Figure 4.5: Contour plot was interpolated from excitation spectra collected at different wavelengths of **ACRSA** in toluene (air-equilibrated solution with a concentration of 50 μM).

To identify any direct CT absorption and emission, excitation profiles were measured using different emission collection wavelengths and are shown in the excitation contour plot (Figure 4.5). Strong CT formation and emission at ~500 nm is observed when exciting into the acridine ππ* band (from 300 to 340 nm). When exciting at energies below this state (wavelengths above 340 nm) also directly photoexcites CT states, however resulting in emission with significantly lower intensity. This indicates the presence of a direct CT absorption, between 350 and 400 nm, which is considerably weaker than the anthracenone nπ* transition. These wavelength-dependent measurements reveal that, when exciting the acridine ππ* state, the orthogonally oriented anthracenone nπ* state remains inaccessible to this excitation energy (Figure 4.4). This effect leads to no contribution of anthracenone nπ* state emission, indicating that IC between these two states (acridine ππ* state and anthracenone nπ* state) is effectively forbidden by the orthogonality of the D and A units. Furthermore, when the anthracenone nπ* transition is excited, this state does not undergo IC to the ^{1}CT state. The simultaneous appearance of emissions from both states, despite no transfer of excitation between these states, suggests an overlap between the direct CT absorption and the anthracenone nπ* transition (in nonpolar environments) (Figure 4.3b).

4.2.2 Dependence of triplet excited states on the excitation wavelengths:

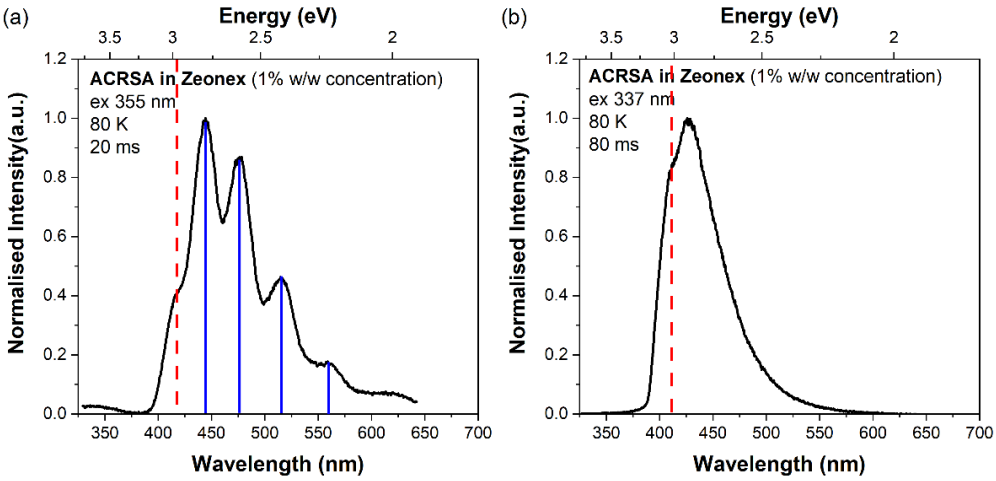

Figure 4.6: Phosphorescence spectra obtained at 80 K of **ACRSA** in zeonex at 1% concentration, excited at (a) 355 nm and (b) 337 nm.

Low temperature phosphorescence measurements were made on films of **ACRSA** disperse in zeonex at 1% w/w concentration to determine the lowest lying triplet state. Very surprisingly, the measured strong phosphorescence is also dependent on excitation, Figure 4.6. Exciting at 355 nm, into the anthracenone (2^1A_2) nπ* singlet state (Figure 4.6a), a well-structured phosphorescence was observed after 22 µs at 80 K. This phosphorescence is

consistent with the phosphorescence of the anthracenone (1^3A_2) nπ* state. Analysing this phosphorescence spectra, a vibronic progression spacing of 190 meV was determined, attributed to strong C=O vibronic coupling with the electronic state (Figure 4.6).[109] Apart from the 190 meV vibronic progression, a high energy knee (at 420 nm) was observed. This emission was attributed to the emission from the higher energy anthracenone (1^3A_1) ππ* triplet excited state, which is weakly in thermal equilibrium with the (1^3A_2) nπ* triplet excited state.[75]

Exciting at 337 nm, into the acridine ππ* band, yields a completely different phosphorescence spectrum with also high intensity, Figure 4.6b. In this scenario, the phosphorescence spectrum displays less defined vibronic structure, and the emitting state has higher energy compared to the anthracenone (1^3A_1) ππ* triplet excited state. This emission is attributed to the acridine (1^3B_2) ππ* triplet excited state. Given that this phosphorescence persists for 80 ms without being eventually quenched by the shorter lived, the highly structured lower energy anthracenone (1^3A_2) nπ* triplet state. This indicates that the acridine and anthracenone sub-units are highly electronically decoupled.

Furthermore, the strong phosphorescence observed from both the D and A triplet excited states suggests that these states do not couple to the molecular CT states at low temperatures. This could arise from either negligible orbital overlap between states, or very weak SOC interaction between them.[108]

4.2.3 Dynamics of excited states in various solvent polarities:

From time-resolved measurements in degassed solutions (Figure 4.7), it is clear that both 337 nm and 355 nm excitations led to very strong DF signals. This indicates that triplet production from both the acridine (1^1B_1) ππ* and anthracenone (2^1A_2) nπ* singlet states is highly efficient. By changing the solvent polarity, a rearrangement in the energy levels is observed, as expected. The changes in the relative energy positions of the singlet and triplet excited states allowed to understand the lifetime decays of the various singlet states, especially the ^{1}CT state which exhibits rather anomalous behaviour. Regardless of excitation wavelength (and thus, purely an effect of the ^{1}CT lifetime), the prompt ^{1}CT lifetime is found to be 8 ns in MCH, 274 ns in toluene and 75 ns in DCM (Figure 4.8).

In MCH, the ^{1}CT ππ* state is energetically positioned above the ^3LE_A nπ* triplet state. As a result, El-Sayed allowed fast ISC competes with radiative decay, effectively quenching the ^{1}CT state to the triplet manifold. In toluene, the solvent polarity relaxes the ^{1}CT state, energetically positioned this state below the ^3LE_A nπ*. Consequently, the ISC channel is significantly reduced, allowing the ^{1}CT to have a longer radiative decay lifetime.

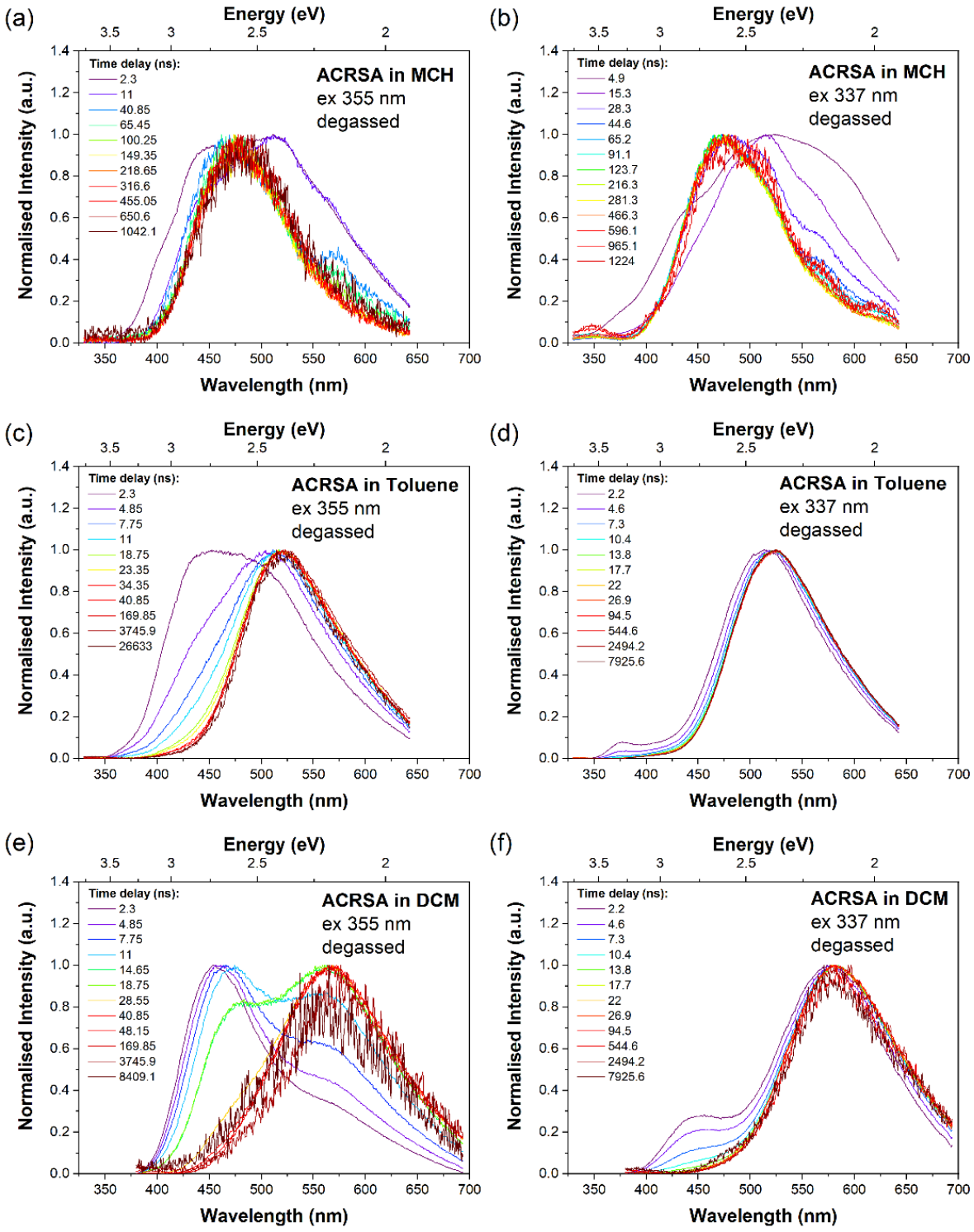

Figure 4.7 : Normalised time-resolved photoluminescence spectra of **ACRSA** in MCH , toluene and DCM, excited at: (a,c,e) 355 nm (the direct mixed $2^1A_2/^1LE_A$ $n\pi^*$ and $1^1A_2/^1CT$ $\pi\pi^*$ transitions) and (b,d,f) 337 nm (into the 1^1B_1 transition). All measurements were performed in degassed solutions (with a concentration of 50 µM) at room temperature.

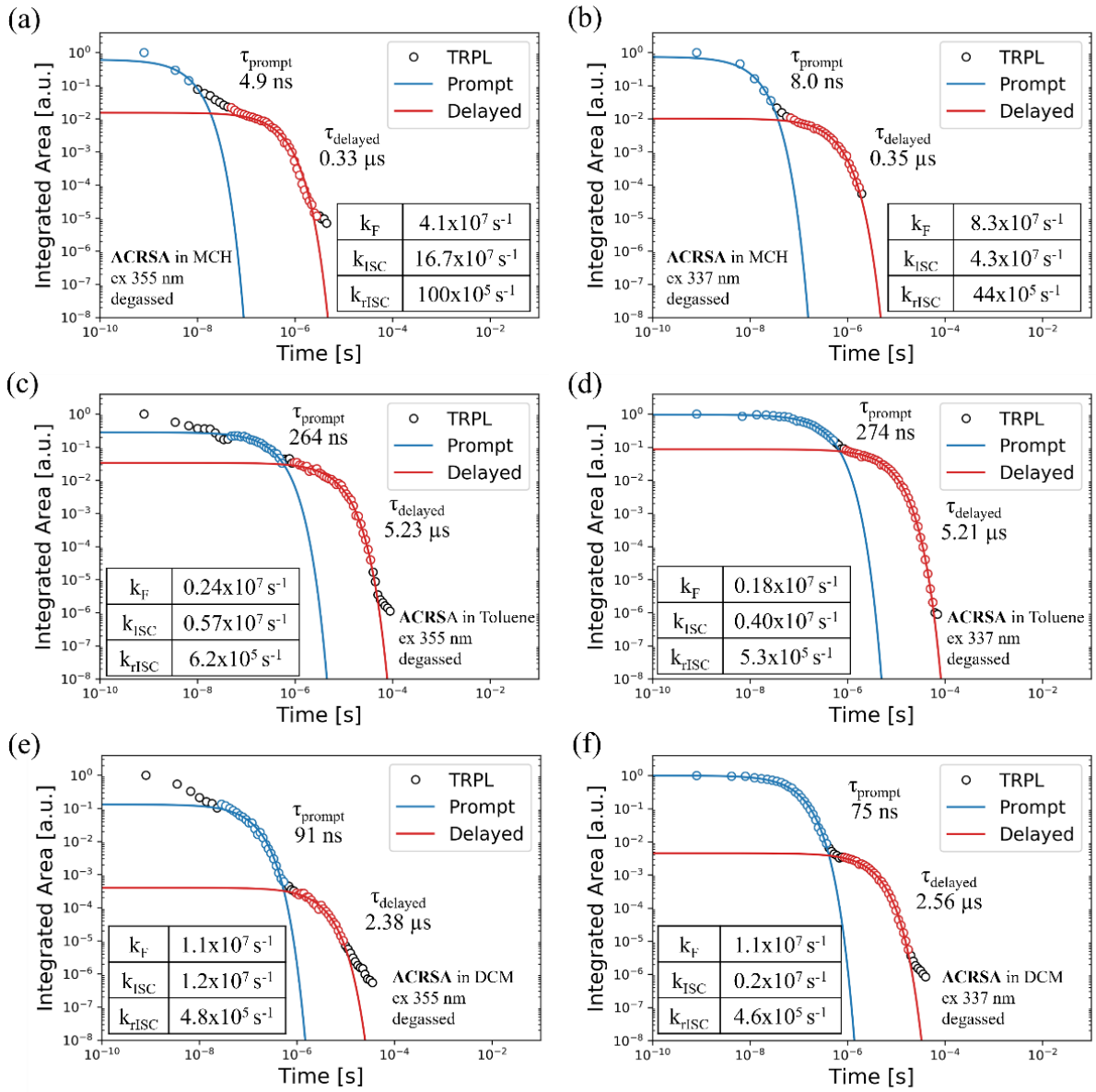

Figure 4.8: Time-resolved PL decay traces of ACRSA in degassed MCH, toluene and DCM solutions (concentration 50 µM) excited at 355 nm into the direct mixed $2^1A_2/^1LE_A$ nπ* and $1^1A_2/^1CT$ ππ* transitions (a, c, e) and at 337 nm into the direct into the 1^1B_1 transition (b, d, f). The data is fitted using a kinetic model described by *Haase et al.*[103]

Indeed, a relatively long singlet radiative decay lifetime of approximately 260 ns is quite reasonable for a ^{1}CT state that is highly decoupled from the ground state, as observed in **ACRSA**. In DCM, the ^{1}CT shifts far to the red spectrum (lower in energy), causing the radiative decay lifetime to decrease. This reduction is a consequence of non-radiative decay following the inverse energy gap law. Therefore, the radiative decay lifetime of the ^{1}CT state provides insight into the relative energy ordering of the ^{1}CT and the lowest energy ^3LE_A nπ* local triplet excited state as a function of environment polarity.

Examining the time-resolved PL decay traces of **ACRSA** in different solvents, the delayed CT emission has a large contribution to the overall emission (Figure 4.8). This large

DF contribution is also observed in numerous examples of exciples TADF molecules, particularly within intramolecular through-space TADF systems.[110] In these systems, although the D and A are physically decoupled in space, the TADF mechanism is still efficient, which it is driven by second order vibronic coupled SOC.[111]

These photophysics results indicate the strong decoupled nature of the D and A moieties of **ACRSA** (the LE states - as demonstrated above in singlet and triplet emission channels). On the other hand, the behaviour of CT states in **ACRSA** resembles that of an intramolecular through space charge transfer-like, rather than the expected through-bond conjugation. This realisation gives a novel insight into the nature of 'spiro-conjugation', which allows for orbital overlap between D and A. While the spiro-centre does not contribute beyond bonding the D and A fragments, fixing distances and orientations that allow a through-space interaction.[112–115] Previous research, as demonstrated by *Jankus et al.*,[116] has indicate that the spiro-conjugation can enhance the intramolecular CT state through the formation of electronically isolate trap states. This isolation is enforced by the weak orbital interaction across the spiro-centre.[117] Importantly, these type of intramolecular through space CT TADF molecules have recently been shown to exhibit high efficient, as demonstrated in the case of the triptycene bridged acridine-triazine donor acceptor TADF molecule **TpAT-tFFO**.[114,118]

Lastly, Figure 4.9 summarises the energy levels involved in the TADF mechanism of **ACRSA**, highlighting the different ISC and rISC pathways. In the right panels, it demonstrates how the solvent polarity affects the ^{1}CT excited state by changing the relative energy ordering in relation to the lowest energy ^3LE_A nπ* local triplet excited state.

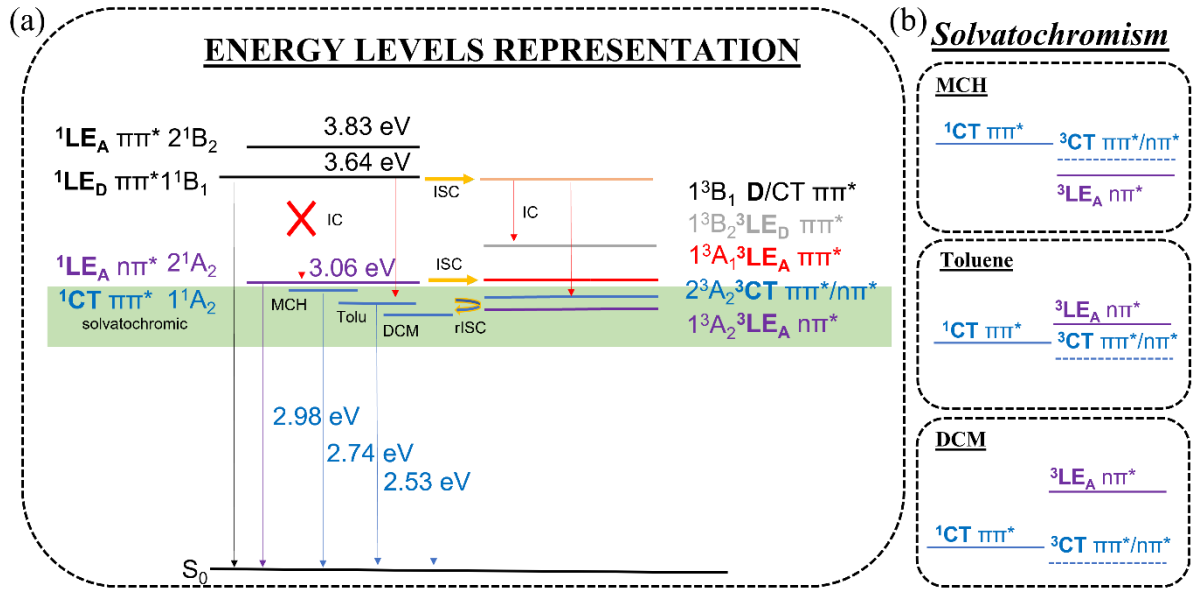

Figure 4.9: Proposed experimental energy level scheme for **ACRSA** in solution. (a) Measured energy levels from spectral onsets of **ACRSA** in different polarity solvents, following the nomenclature of Lyskov and Marian.[108] The green band

represents the energy range over which we observe solvatochromic states. Red arrows represent non-radiative transitions (IC). (b) The effect of solvent polarity on the CT states, highlighting the reorganization of the energy levels which strongly affects the decay rates, ^{1}CT lifetime, ISC and rISC rates.

4.3 Conclusions:

To conclude, the photophysical response of the spiro-acridine–anthracenone TADF molecule, **ACRSA**, exhibited a high dependence on excitation wavelength. Depending on the initial state populated (donor, acceptor, or direct CT transition) through different excitation wavelength, a distinct response and TADF channels are observed. Moreover, even minor changes in the surrounding environment led to a rearrangement of energy levels, resulting in a complete change of available decay channels and the efficiency of rISC processes. This phenomenon arises from the excitation of either the acridine donor or anthracenone acceptor subunits. These subunits maintain a critical level of electronic decoupling, remaining almost perfectly orthogonal due to the rigid spiro D–A bridging bonds. Therefore, this dependence on the excitation wavelength occurs during the prompt, delayed, and phosphorescence emission, which triggers either the donor or acceptor and the molecular CT state of **ACRSA**.

Importantly, despite the molecular CT state in **ACRSA** exhibited weak direct excitation and vibronic coupling with the units, the contribution from delayed CT emission is ten times more intense than the prompt CT emission. This observation suggested that the CT state in **ACRSA** should be considered as a through-space CT state rather than through bond state. This insight highlighted that spiro-conjugation presents orbital overlap of D and A represented by through-space interaction. Where the spiro-centre is only responsible for the spatial positioning of the D and A fragments, rather than directly facilitating electronic conjugation.

Overall, **ACRSA** must be considered as three distinct molecules in one, as evidenced by the acceptor and donor subunits and the molecular CT photophysics. This complex photophysics is achieved by critical decoupling of the D and A units, facilitated by the spiro-centre. In this context, Kasha's rule remains applicable to each subunit locally, but it can be disregarded when considering the photophysics of the entire molecule. Therefore, the competing decay channels from this spiro D-A system may result in a lower device performance compared to C-N bond TADF molecules.

5 Probing emissive excited states: the conformational and spontaneous polarisation effects in solid films of TADF molecules

This chapter covers the study of the spiro TADF emitter, **ACRSA**, within guest-host films. In the solid state, it is commonly observed in the time-resolved photoluminescence (TRPL) decay as a complex, multiexponential decay in the delayed fluorescence regime. This arises from a distribution of rISC rates, attributed to the dispersion of fixed D–A dihedral angles in the guest molecules. Here, I will explore the **ACRSA**'s unique rigid spiro C-C bond structure, which prevents inhomogeneous effects caused by variable donor-acceptor bridge dihedral angles, thus exploring the influence of the host effect in this system. Subsequently, by increasing the concentration, I will investigate the lower excited states of **ACRSA**. These states are attributed to intermolecular excimer states and contribute to slow TADF components, as well as broadening the CT emission band.

The work presented in this chapter has been already published:

i. Franca, L. G.; Danos, A.; Monkman, A. Donor, Acceptor, and Molecular Charge Transfer Emission All in One Molecule. *J. Phys. Chem. Lett.* **2023**, *14* (11), 2764–2771.
ii. Franca, L. G.; Danos, A.; Monkman, A. Spiro Donor–Acceptor TADF Emitters: Naked TADF Free from Inhomogeneity Caused by Donor Acceptor Bridge Bond Disorder. Fast RISC and Invariant Photophysics in Solid State Hosts. *J. Mater. Chem. C* **2022**, *10* (4), 1313–1325.

5.1 Overview:

As previously mentioned, minimising the electron exchange energy and thus reducing ΔE_{ST} hold significant importance for TADF molecules. This can be achieved by twisting the donor and the acceptor to near orthogonality. Spiro TADF molecules have their orthogonality enforced by the tetrahedral spiro carbon atom.[109] On the other hand, molecule linked by C-N bridge allow relative rotation between donor and acceptor, leading to a distribution of ΔE_{ST} and k_{rISC} rates as a consequence, from even minor variation in the D-A dihedral angle.[60] In solid state, this distribution becomes more pronounced due to restricted motion imposed by the host on the guest molecules. This restriction leads to the existence of dispersion of fixed D–A dihedral angles in the guest molecules, as evident in the complex multiexponential of the delayed fluorescence observed in the time-resolved photoluminescence measurements.[87,119] Substantial efforts have been dedicated to controlling D–A angles in TADF materials to maximize k_{rISC}.[120] Strategies such as attachment of heavy adamantyl groups

or the linkage of a diphenyltriazine acceptor in carbazole donors have been reported to restrict torsional motions.[121,122] The introduction or relieving steric influences can also significantly influence the D–A angles and therefore also TADF performance.[60,67,123,124] Additionally, as I will demonstrate, exploring spiro TADF molecules further contributed to this understanding.

Building upon the insights provided in the previous chapter, which an in-depth study on the molecular photophysics of the **ACRSA** molecule in solution was shown, in this chapter, I will investigate its properties within a range of solid host materials (molecular structure, Figure 5.1). This study aims to elucidate the perturbations arising from solid-state interactions. Exploring **ACRSA**'s unique spiro derived properties provides unprecedented new insight into this area to answer several questions of host interactions that play important role in the response of the system. These novel finding have the potential to contribute to a new understanding on the current limited operational lifetimes experienced by TADF emitters.

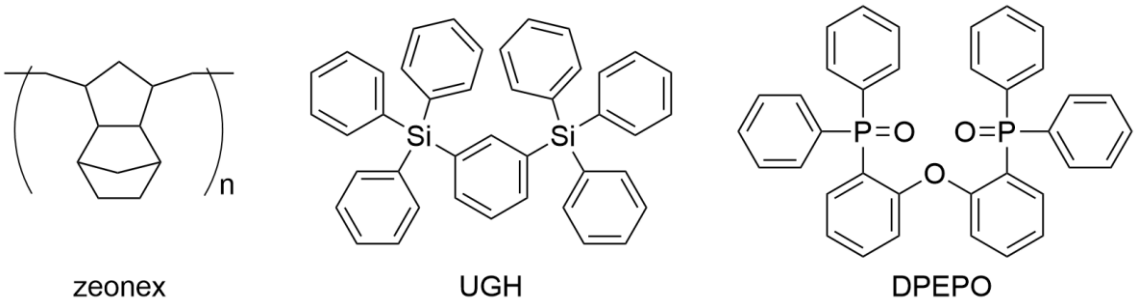

Figure 5.1: Molecular structure of the host molecules used in the chapter: zeonex, 1,3-Bis(triphenylsilyl)benzene (UGH) and bis[2-(diphenylphosphino)phenyl]ether oxide (DPEPO).

5.2 Results and Discussion:

5.2.1 Optical spectroscopy measuremets at 1% wt concentration:

As shown in the previous chapter, the photophysics of **ACRSA** are highly dependent on the excitation wavelength. Consequently, Figure 5.2 shows emission spectra by exciting at various wavelengths for 1% wt **ACRSA** in different environments: zeonex, UGH and DPEPO. Under 350 nm excitation, the spectra in zeonex displays a poorly structured emission, characterised by peak energy 2.8 eV (460 nm) and a higher energy knee at 3.05 eV (410 nm). Comparing these results to previous solution spectra (seen in Figure 4.2), it becomes evident that zeonex mirrors an environment very similar to MCH solution, where the ^{1}CT and ^{1}LE excited states are highly mixed giving strongly overlapped emission. In contrast, in DPEPO and UGH films, the ^{1}CT emission band dominates, peak position at 2.4 eV (520 nm). Additionally, a blue shoulder emerges around 450 nm, which is highly dependent on excitation wavelength. Importantly, the red shift observed in the in solid state emission of the ^{1}CT excited

state is considerably less pronounced compared to that the results obtained in toluene solution (a low polarity solvent – Figure 4.2).

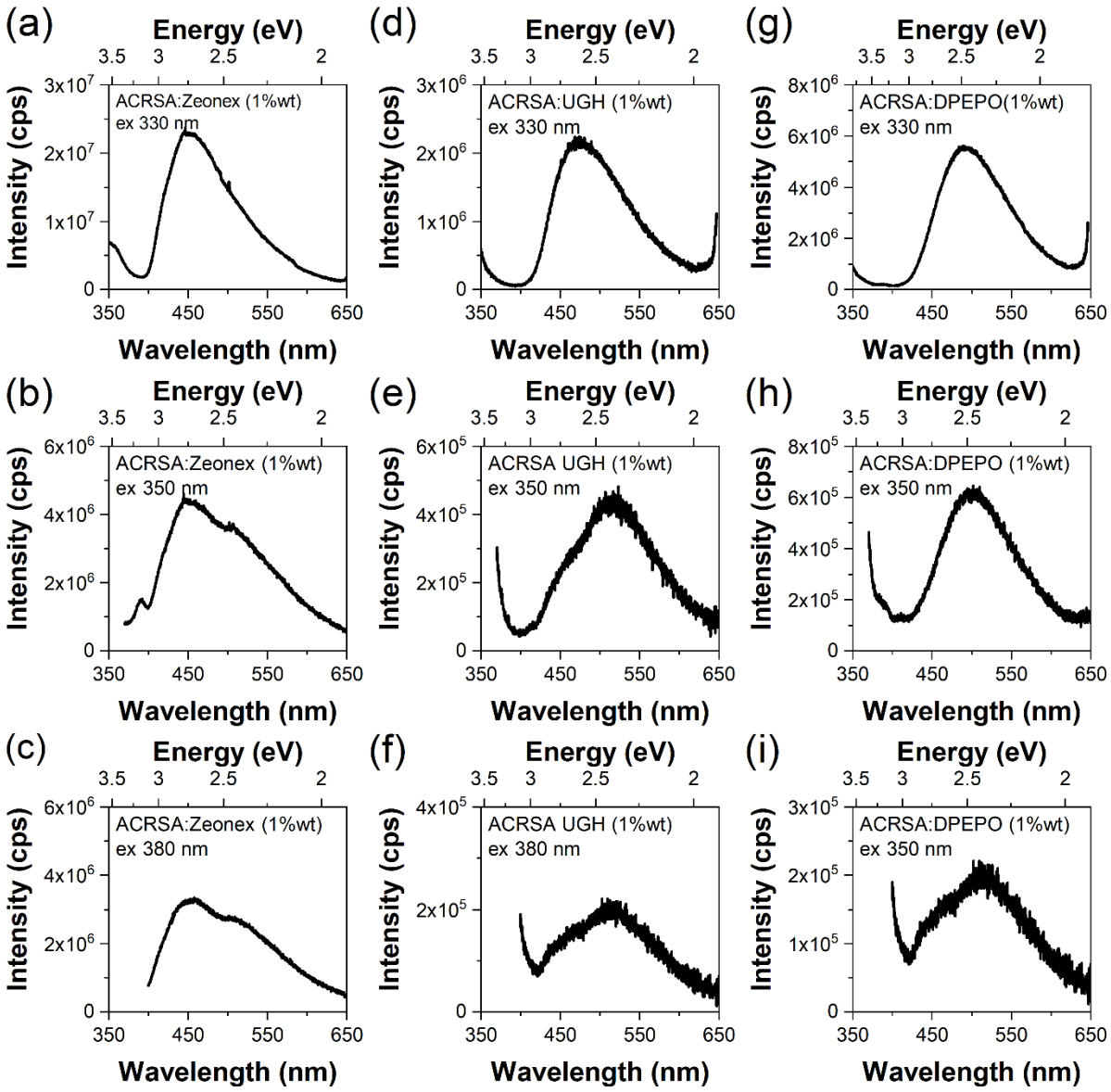

Figure 5.2: Excitation wavelength dependent steady-state emission from **ACRSA** dispersed in zeonex (a-c), UGH (d-f) and DPEPO (g-i) at 1%wt loading, measured at room temperature in air.

In solution, the ^{1}CT excited state of **ACRSA** induces a large change in dipole moment due to the rapid reconfiguration of the solvent molecules. This phenomenon leads to a relaxation of Coulomb energy of the excited state, even in solvents with low polarity such as toluene.[125] However, in solid films, the red shift is only around 30 meV in DPEPO compared to UGH, significantly less than observed in toluene (280 meV). As previously discussed,[126–128] this difference arises from the fact that, unlike solvent molecules, a solid host cannot rearrange around the excited guest molecule (after excitation) in the same level a solvent molecule can. Consequently, the relaxation of the Coulomb energy in solid state is limited, resulting in the

absence of an analogous solid state solvatochromism. It is noteworthy that the host can arrange around the emitter molecule in the ground state, particularly if it has a large ground state dipole moment, but this configuration remains largely unaltered in the excited state. Consequently, there can be no directly analogous 'solid state solvatochromic' effect. In line with the finding by Lyskov *et al.*,[108] who calculate that the ground state dipole moment of 5.46 D for **ACRSA**, these outcomes suggest that only a minor ground state effect should be expected. This conclusion aligns with this small red shift of ^{1}CT excited state across different hosts environments.

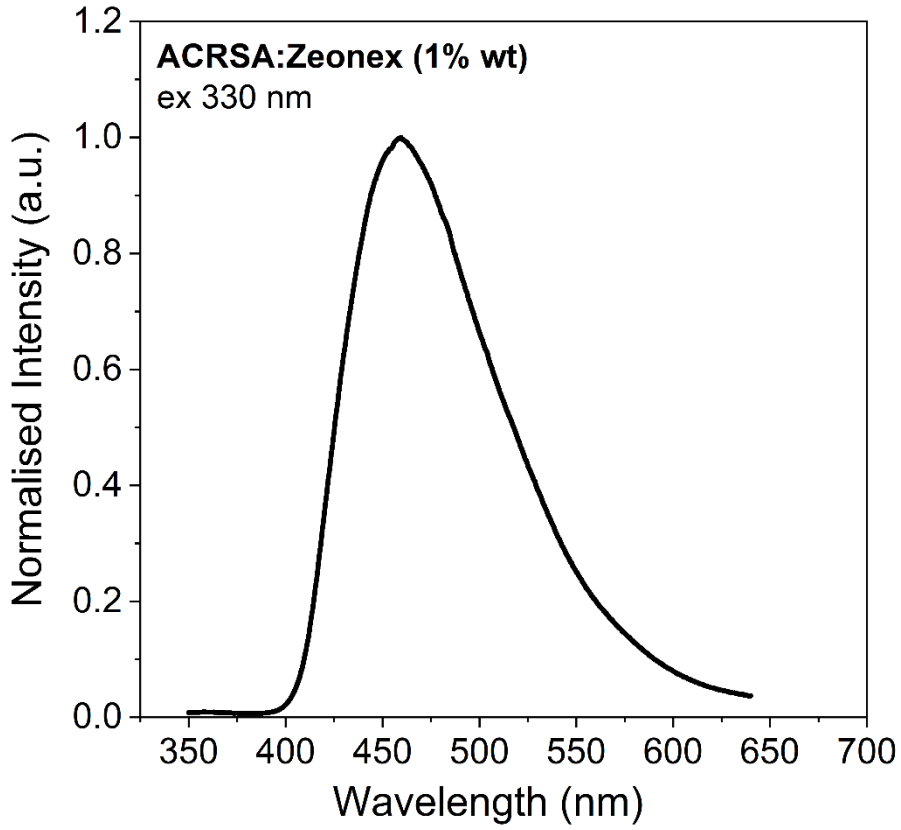

Figure 5.3: Steady-state emission spectra of **ACRSA** in zeonex (1% wt loading). Measurements performed in under vacuum conditions, exciting at 330 nm.

Emission spectra of **ACRSA** in zeonex under 330 nm excitation shows an emission band around 350 nm (Figure 5.2a), which arises from the 1^1B_1 exciton state (acridine donor unit fluorescence)[127], a feature strong observed in MCH solution, for example. By exciting at 350 nm, a well-resolved characteristic appears at the blue edge of the CT band, aligned with the observed ^{1}LE emission from the acceptor in solution. At 380 nm excitation, effectively yields the main ^{1}CT emission band (*ca.* 550 nm) alongside a blue shoulder at 450 nm. These finding show that films behave very similarly to each other and to MCH solution. However, the large overlap between the ^{1}LE and ^{1}CT emission in the films results in poor spectral resolution. The highest intensity of ^{1}LE acceptor emission is observed for **ACRSA** in zeonex exciting at 350

nm, confirming the presence of these states. Moreover, as established from solution data, the ^{1}LE state is rapidly quenched by ISC. In film, this phenomenon yields an emission band that appears unstructured from the ^{1}LE – a characteristic consistent with emission from a hot, unrelaxed vibronic state, as previously suggested by Greene *et al.*[129] for similar acceptor molecules. Consequently, this emission exhibits a more Gaussian band shape in contrast to the structured bands observed in MCH.

Figure 5.3 shows the emission spectra of **ACRSA** at 1% wt in zeonex measured under vacuum conditions. Minimal emission contribution from the ^{1}LE excited states (either from donor or acceptor units) is observed in the vacuum measurements, similarly findings seen in solution where degassing leads to a predominant ^{1}CT DF emission contribution that totally dominated the emission.

Time-resolved photoluminescence was performed in the films. Similar to what was observed in the MCH solution, the zeonex films (with a 1% wt **ACRSA** loading) exhibited an instantaneous and broad emission band (with FWHM of approximately 125 nm), centred at 520 nm (2.38 eV) (shown Figure 5.4a). This emission band undergoes decay with a lifetime of 6.2 ns (Figure 5.4b). This might indicate an emission from a metastable state that originates from a significantly conformationally distorted structure, closely resembling the theoretical description presented by Fan *et al.*[130] Moreover, the broad emission band centred at 520 nm closely aligns with the CT band observed in the toluene solution. As this broad band decays, a prompt and DF emissions centred around 448 nm are observed. These emissions exhibit a multicomponent lifetime of 93.7 ns, 1.2 μs, and 8.3 μs. These complex and long-lived emissions might indicate the presence of two competing rISC channels arising from closely (in energy) excited states. These channels could arise from the mixed nπ*/ππ* (^{1}LE/^{1}CT) character of the ^{1}CT state, which exhibits a small energy gap to local triplet states.

Spectrally resolving these states presents an enormous challenge due to the complexity of the overall emission decay. However, by comparing these results to those obtained from the MCH solution, it is possible to attribute the emissions with lifetimes of 93.7 ns and 1.21 μs to the prompt and DF CT emissions, respectively. Since zeonex behaves in a manner similar to the solution state, it is likely that this behaviour originates from the asymmetrically branched polyolefin structure of zeonex. This structural feature prevents crystallization and creates a significant free volume within the polymer network, allowing guest molecules to occupy this space with minimal or no hindrance to conformational motions.

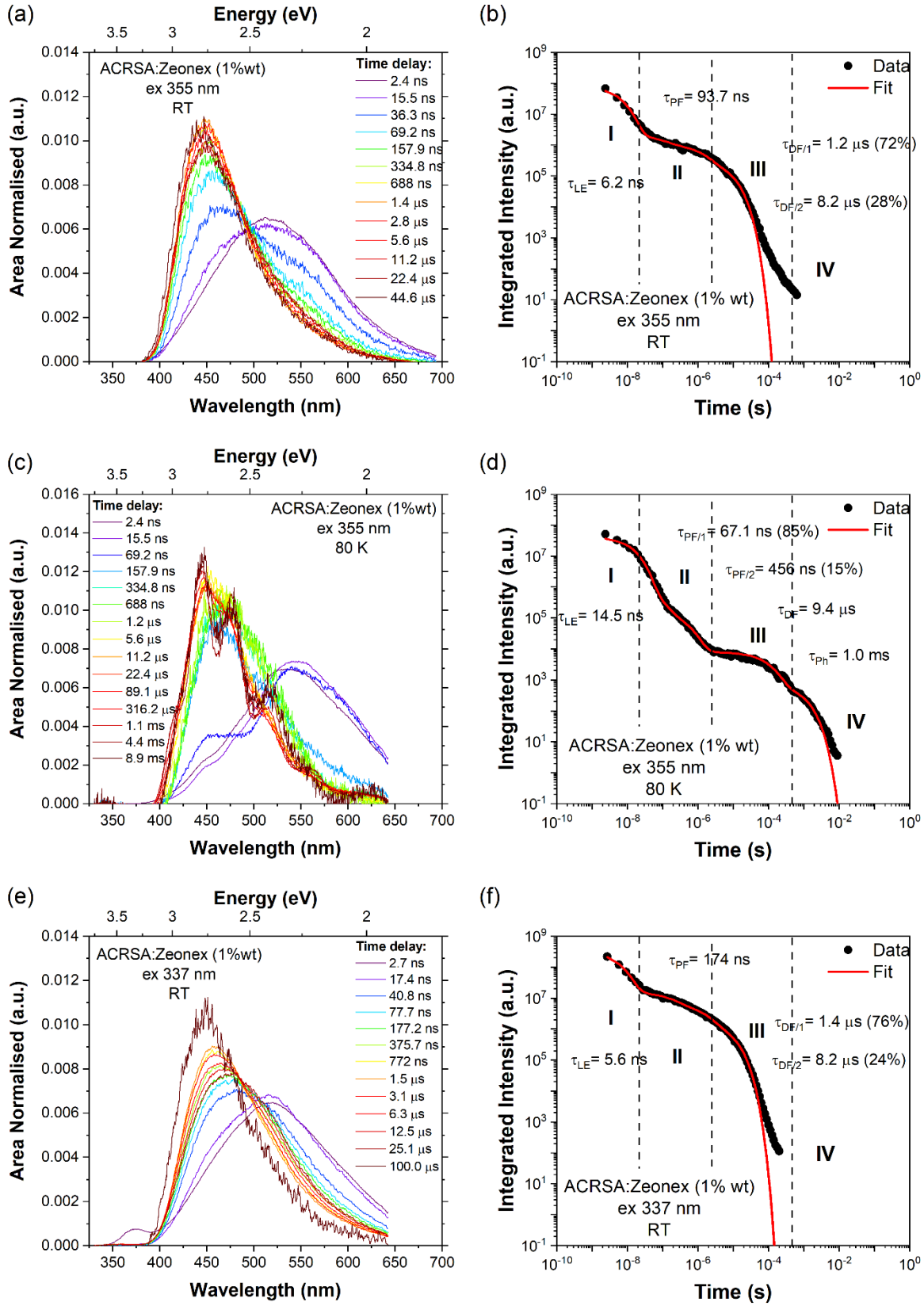

Figure 5.4: Area normalised of the time-resolved emission spectra (shown in left panels) of **ACRSA** in a zeonex matrix (with a 1% loading) and their corresponding kinetic decays and fitted lifetimes (presented in the right panels) . These measurements were performed at room temperature and at 80 K, using 355 nm and 337 nm excitation. The lifetimes were estimated by fitting with multiexponential functions.

The time-resolved photoluminescence decay of zeonex films measured at 80 K are more complex. The kinetic trace (Figure 5.4d) displays four distinct decay processes, with well-resolved decay times. In the initial transient, the broad emission at 520 nm is not so clearly observed, suggesting that this component is strongly influenced by thermally activation. A more complex spectrum is observed at the first few nanoseconds indicating possible multiple spectral components. This suggests that multiple transient emitting states could potentially be originated from different metastable molecular configurations.[130]

As the time delay increases, the emission band resembling CT character decays, peak ca. 550 nm. After 150 ns (as indicated by the green curve in Figure 5.4c), an emission band appears, consisting of primary emission centred at around 450 nm, accompanied by a shoulder at 470–500 nm. The latter component decays with lifetime of 458 ns. After 25 μs, a highly structured emission band dominates the overall emission – attributed to phosphorescence, with lifetime of 1 ms, originating from a local excited triplet state. Importantly, this phosphorescent emission displays a well-defined vibronic progression.

The phosphorescent emission is energetically closer to the singlet ^{1}CT (as indicated by an onset energy ca. 3.1 eV, seen in Figure 5.4a) with an onset energy of 2.97 eV. Furthermore, the energy spacing of the vibronic replicas is 0.19 eV (1530 cm^{-1}), corresponding to the energy of a C=O stretch. This characteristic is attributed to the phosphorescence emission from the anthracenone ^{3}LE $\pi\pi^*$ state localised around the C=O bond.[108] It is worth noting that this phosphorescence is also observed in the 'early' ms spectra of **ACRSA** in UGH and DPEPO films at 80 K (Figure 5.5). In the phosphorescence spectra, a blue shoulder at 400-425 nm (onset 3.12 eV) is also observed. This shoulder does not fit with the 0.19 eV vibronic progression observed in the main band. This suggests a second underlying higher energy phosphorescence,[91,131] potentially originating from the $^3\pi\pi^*$ state.

As mentioned in the previous chapter, excitation at 337 nm targets the 1^1B_1 exciton state, as opposed to 355 nm excitation that directly excites the ^{1}LE and ^{1}CT states. Therefore, time-resolved photoluminescence was performed in films using 337 nm excitation for further comparison. The results revealed that exciting at 337 nm provide excess energy to the molecules (Figure 5.4e-f) resulting in higher intensity DF from the ^{1}CT band. This enhancement is attributed to the increased production of triplet excited states induced by the 337 nm excitation.

Time-resolved photoluminescence measurements were also performed on 1% wt **ACRSA** in UGH and DPEPO films using both excitations, 355 nm and 337 nm (shown in Figure 5.5). The results showed that the CT emission displays minimal temporal evolution

when excited with 337 nm, and only a negligible shift when excited with 355 nm excitation. As expected for the rigid spiro-TADF emitter, the CT energy maintains a constant onset of 2.98 eV (in UGH) and 2.95 eV (in DPEPO), both showing a peak around 2.5 eV.

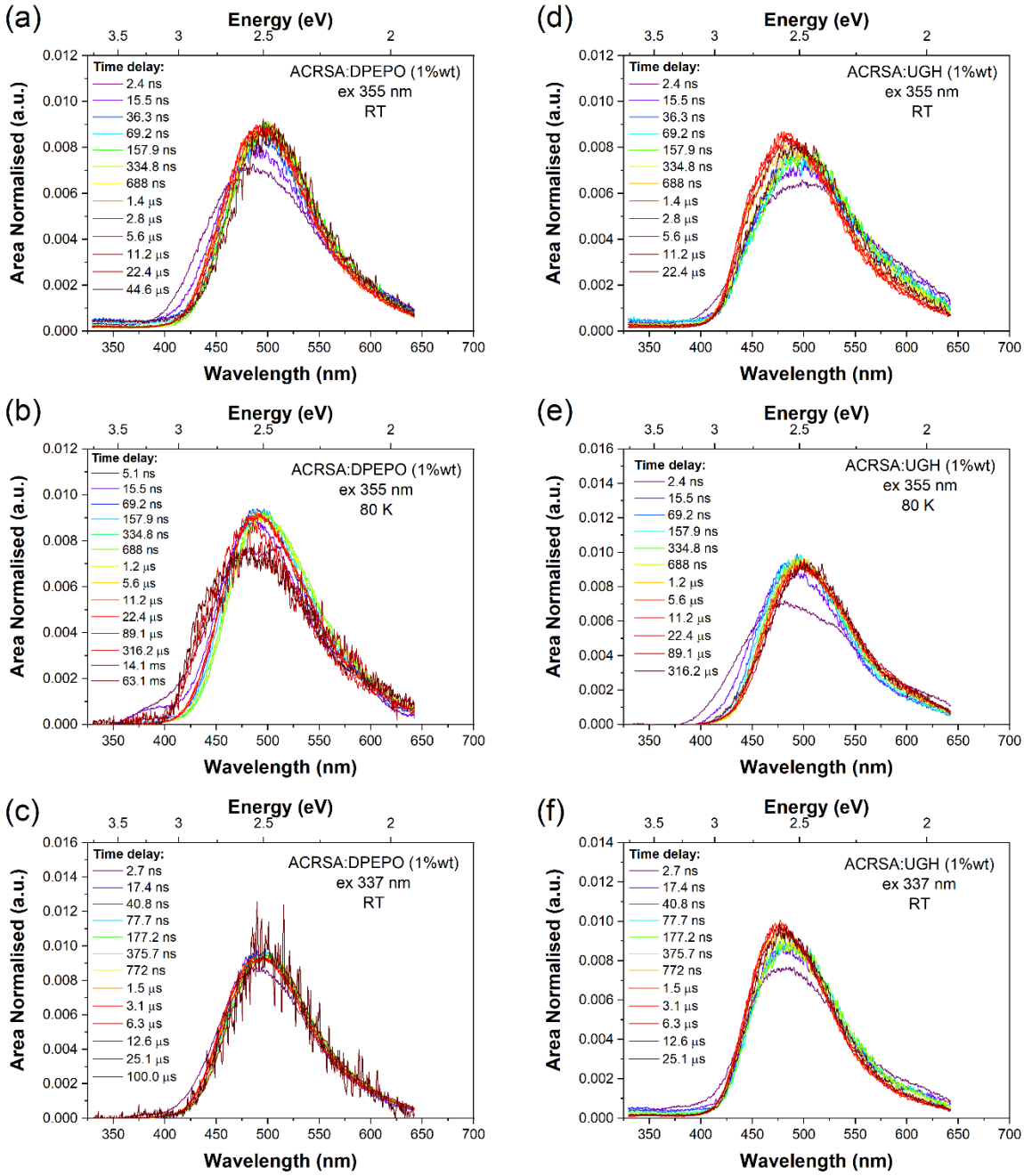

Figure 5.5: Area normalised of the time-resolved emission spectra of **ACRSA** in a DPEPO (shown in left panels) and UGH matrix (shown in right panels) both with a 1% loading concentration. These measurements were performed at room temperature and at 80 K, using 355 nm and 337 nm excitation.

When exciting at 337 nm, which populates the 1^1B_1 excited states, both UGH and DPEPO films exhibit relatively straightforward behaviour (Figure 5.5). The spectra remain relatively constant, showing minimal temporal shifts and maintaining consistent band shapes. In the case of UGH, there is an inhomogeneous broadening of 30 meV (an emission red shift over 20 µs).

While in DPEPO, this value is 35 meV. Within the first 10 ns, a small blue edge contribution is seen, attributed to ^{1}LE emission, along with a small contribution from the 1^1B_1 exciton at 350–400 nm.

Upon exciting at 355 nm (which populates the ^{1}LE/^{1}CT mixed transitions), the emission from UGH films within the first 100 ns reveals a relatively broad band, centred at around 500 nm. Furthermore, accompanied this emission band, a pronounced (but small contribution) of red tail in the 550–650 nm region was observed. However, the predominant emitting species, particularly within in the DF region, is a single band centred at around 484 nm, with an onset at 420 nm (2.95 eV). Whereas in DPEPO, the earliest emission is slightly blue shifted, with an onset at 400 nm (3.10 eV), consistent with emission from the ^{1}LE state. In this case, the predominant emitting species emerges from 100 ns onward and is centred at 490 nm. Overall, the spectral weight in UGH is concentrated more in the range of 450–475 nm, whereas in DPEPO, the majority of spectral weight falls between 475 nm and 510 nm.

At 80 K, the **ACRSA** UGH and DPEPO films also exhibited phosphorescence emission, as shown in Figure 5.5. The spectral shape and onset of this phosphorescence match those observed in zeonex, thereby confirming its origin as the anthracenone ^{3}LE π–π* triplet excited state. This triplet excited state represents the lowest monomolecular triplet state of **ACRSA**, regardless of the host material.

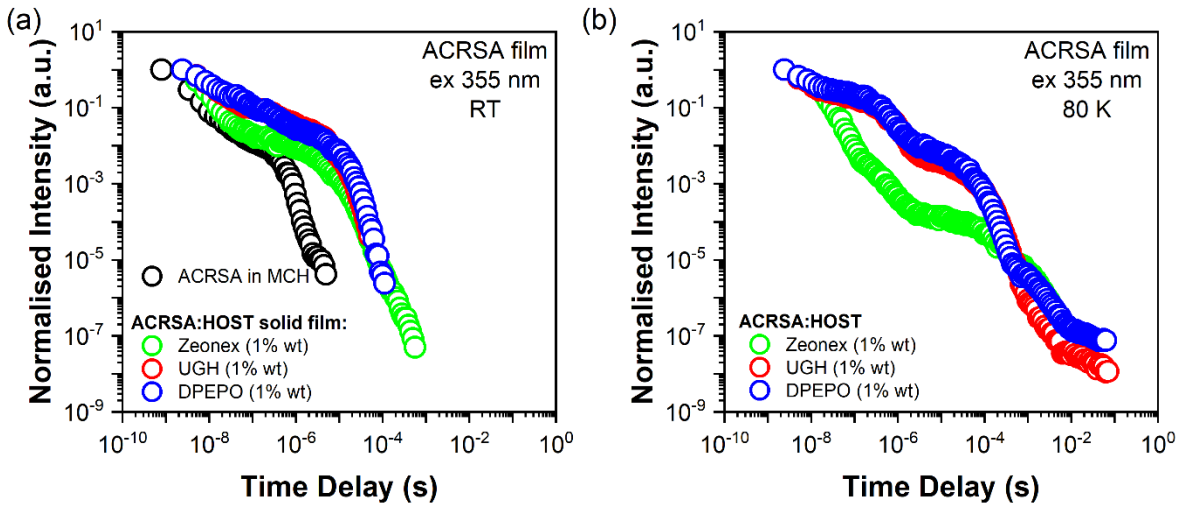

Figure 5.6: Time-resolved photoluminescence decay for **ACRSA** in different host matrices at 1% loading, (a) recorded at 300 K, and (b) 80 K. Decay trace of **ACRSA** in MCH solution (with 20 μM concentration) is shown in (a) for reference.

Figure 5.6 presents a comparison of all the decay traces for **ACRSA** in various host matrices. At room temperature, it is evident that zeonex shares similarities with **ACRSA** in MCH solution, particularly during the prompt regime. Additionally, the kinetic decays in both UGH and DPEPO films appears to follow a simple monoexponential function for both prompt

and DF regimes. The representation of the DF regime by a monoexponential function is a consequence of **ACRSA**'s spiro rigid structure. This implies that in the case of the typical D–A TADF materials, the significant apparent time-dependent red shifts in their CT emission and multiexponential decay in the DF regime arises from inhomogeneities in the D–A dihedral angle. The distinct D–A dihedral angles of CT states (with different energies) result in varied lifetimes, giving rise to dispersive ISC, rISC, and radiative decay rates. Consequently, the rigid spiro bridging of **ACRSA** prevents variation in D-A dihedral angles, resulting in the absence of distribution of the decay rates.[88]

At lower temperatures, the decay profiles become more complex, displaying four distinctive regimes. Notably, at low temperature, more pronounced changes were observed in zeonex, indicating that temperature has a stronger impact on the DF process in zeonex films.

5.2.2 Optical spectroscopy at 10% wt concentration and neat films:

The excitation-dependence steady-state emission spectra were also investigated for 10% wt **ACRSA** in UGH, DPEPO, and neat films, as shown in Figure 5.7. The emission spectra of these films displayed considerably less dependence on the excitation wavelengths. Across all cases, the ^{1}CT emission band dominated the overall emission, with peak at around 2.4 eV (520 nm). The ^{1}CT emission band was also accompanied by a blue shoulder at around 450 nm, which exhibited a higher sensitivity to the excitation wavelength. It is worth noting that the ^{1}CT emission of **ACRSA** in UGH, DPEPO, and neat film presented significant less red shift compared to what was previously observed in toluene (Figure 4.2).

Time-resolved photoluminescence spectra recorded at 300 K displayed a minor and rapid ^{1}LE emission contribution in the DPEPO, UGH (10% wt loading) and neat films (Figure 5.8), similar to the behaviour observed in degassed solution. At 10% loading films, distinct photophysics was observed compared to in the 1% loading films, while no significant differences among the various host matrices at 10% wt concentration and the neat film. Within these films, a gradual red shift was observed in the time-resolved emission spectra. An isoemissive point is clearly observed in the area-normalised time-resolved spectra at around 505 nm, suggesting the presence of two distinct emissive species in the films. The redder emission band exhibits slower decay with extended DF lifetimes, while the bluer emission band decays rapidly with fast DF. The longer lifetime species, which emerges gradually (peak at 2.4 eV), originates from a new excited state species exclusively found at 10% **ACRSA** loading. This species displays a red shifted and broader emission band compared to the 1% wt loading films.

Furthermore, it is evident that the blue edge of the emission decays as the red edge intensity increases, as shown in Figure 5.8. This indicates that the blue species converts to the red species in competition with radiative decay.[132]

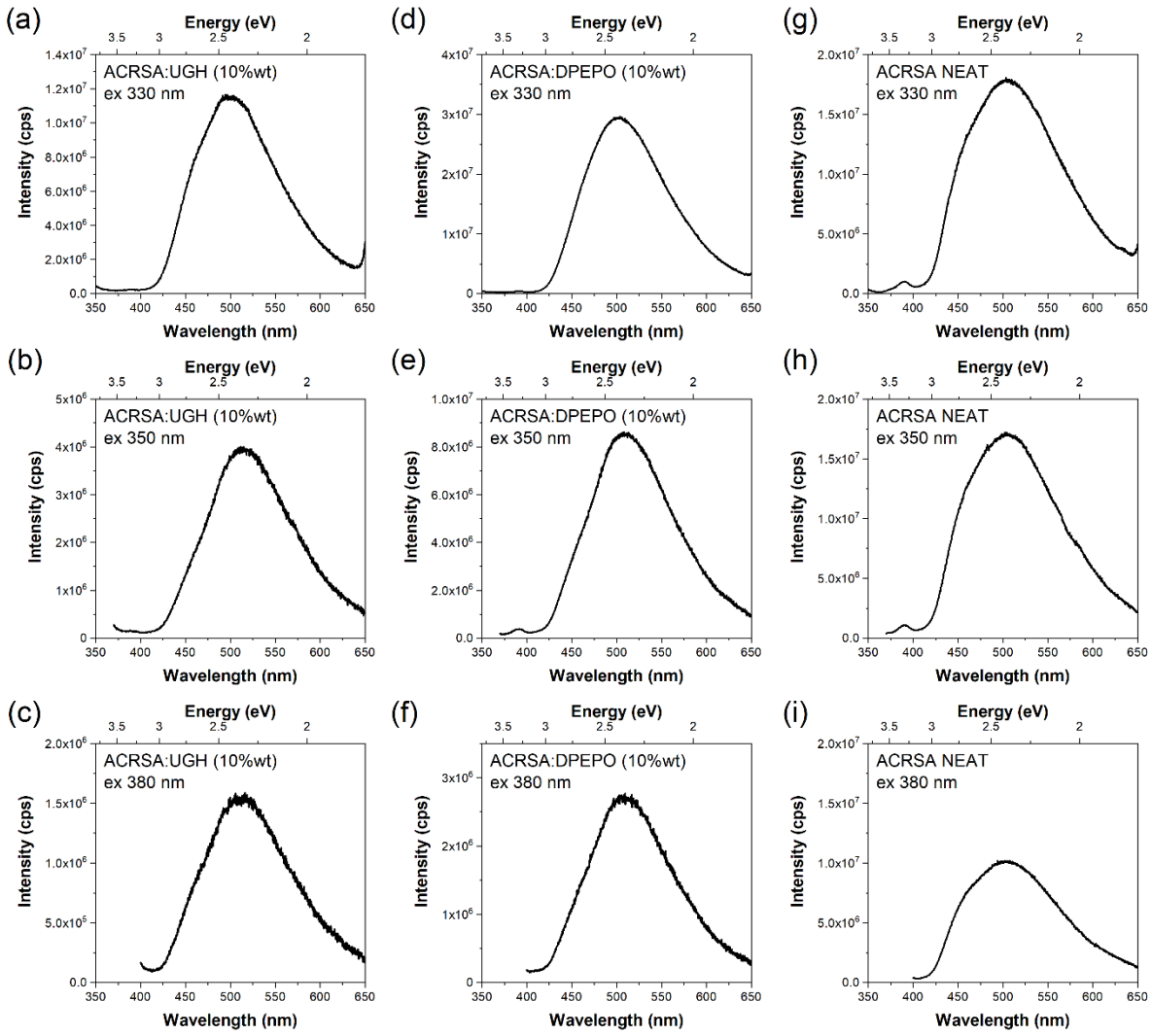

Figure 5.7: Steady-state emission spectra as function of excitation wavelength of **ACRSA** in UGH (a-c), DPEPO host matrices (d-f) at 10% wt loading, and neat films (g-i), recorded at room temperature and air conditions.

This new behaviour in the highly loaded films is interpreted as the formation of some weakly interacting excimer-like state between nearest neighbours. Such a weakly interacting state would be consistent with intermolecular interactions between two spiro molecules. The evolution of the time-resolved spectra contradicts any molecular confirmation changes (especially considering the rigidity of the **ACRSA** molecule) or dispersive rISC rates as found in non-spiro D–A TADF molecules.[126] DF in DPEPO, UGH (10% wt loading) and neat film exhibits the same trends and originates from the low energy CT emission band.

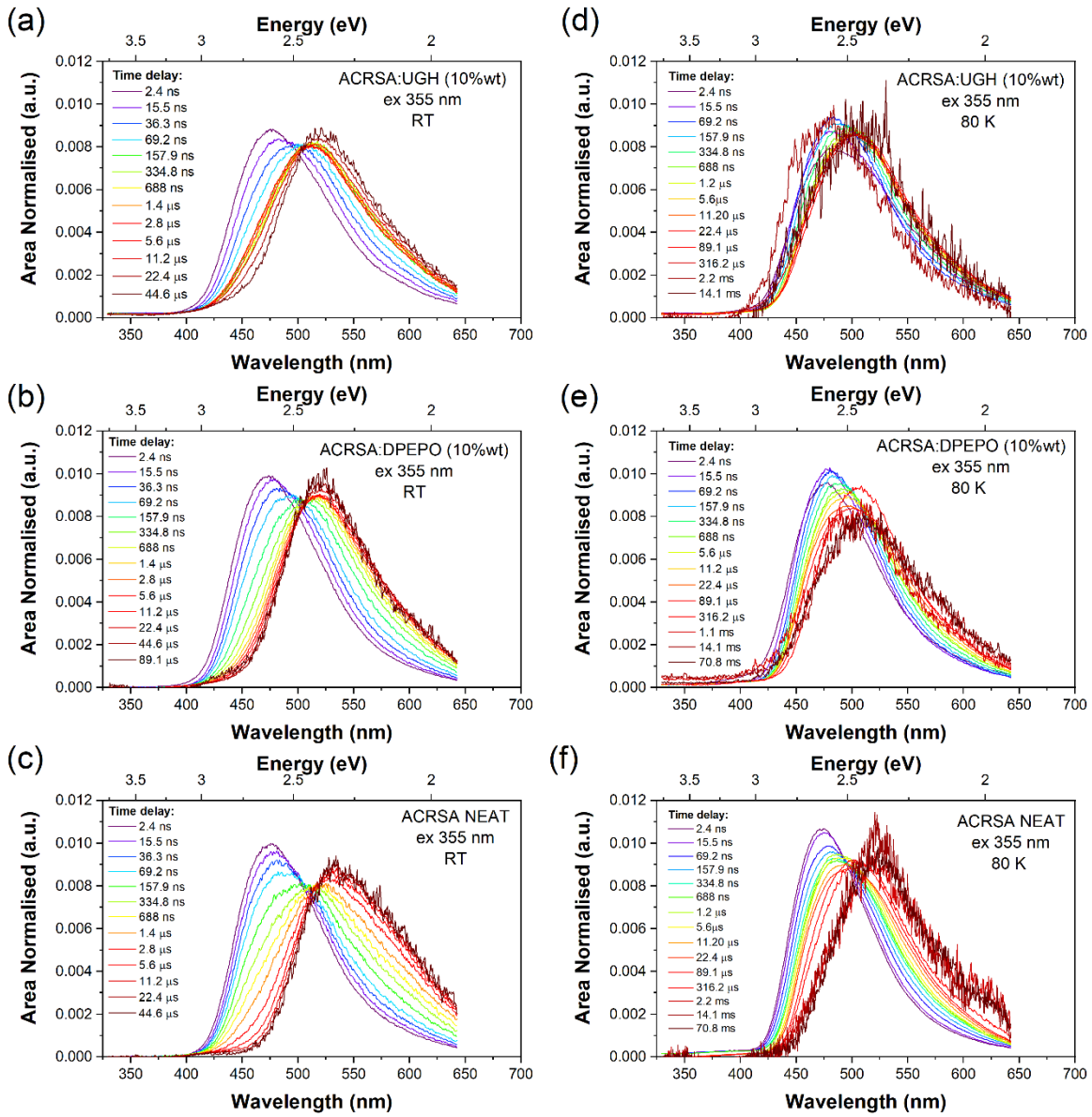

Figure 5.8: Area normalised of the time-resolved emission spectra of **ACRSA** in UGH, DPEPO host matrices at 10% wt loading, and neat films, recorded at room temperature (left panels) and 80 K (right panels). These measurements were performed using 355 nm excitation.

At 80 K measurements, the two distinct emission bands remain observable: one at around 470 nm (peak) in the early times and another at 500–510 nm (peak) in the later times. As observed at room temperature, an isoemissive point is observed (Figure 5.8). However, the whole spectral evolution takes approximately two orders of magnitude longer to occur at 80 K (Figure 5.9), indicating that this mechanism is thermally activated. Furthermore, considering that the redder species is at a higher energy compared to 300 K, this is interpreted as evidence of thermally activated excimer formation. In the case of UGH, the emission at early times presented an onset around 420 nm (peak at 475 nm) and exhibits some structural features

characteristic of a CT state. This emission strongly resembles the main emission band observed in zeonex films.

At later times, a different band shape emerges, centred at around 520 nm. The distinct new band with an onset at 2.73 eV is strongly observed in the neat film spectra and decays within very long lifetimes. This emission band is therefore attributed to the phosphorescence of the excimeric species. In the UGH, there is also evidence of phosphorescence originating from the monomeric species. An initial blue component with an onset at 405 nm (3.06 eV) emerges, which then decays and gives rise to a highly persistent phosphorescence at 426 nm (onset at 2.91 eV) lasting for over 70 ms.[91,131] This latter emission is attributed to the excimeric species. While monomeric phosphorescence is expected to arise from the ^{3}LE state of the acridine donor unit, similar to its observation in zeonex films at 80 K.

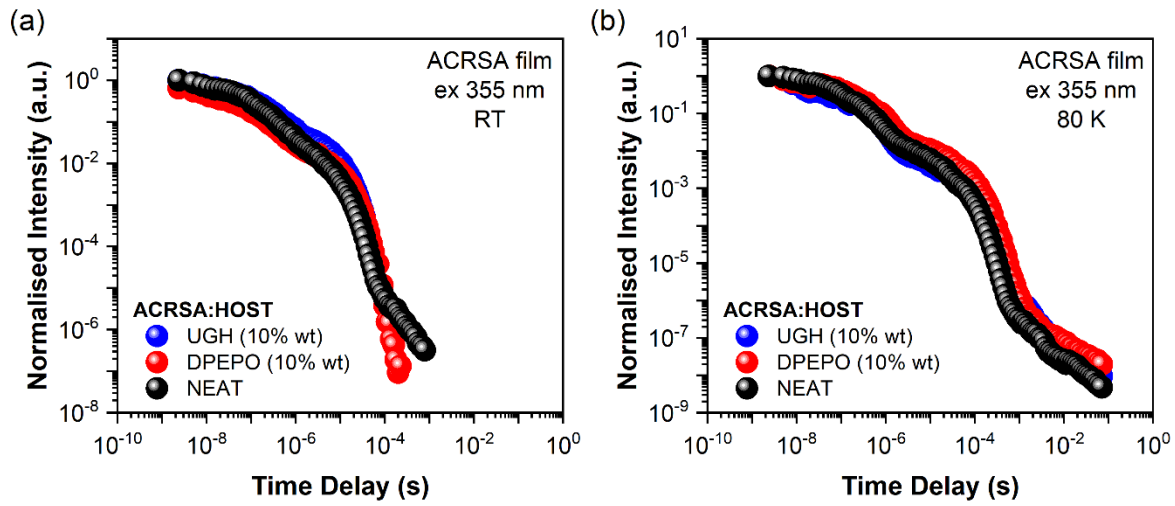

Figure 5.9: Time-resolved photoluminescence decay for **ACRSA** in UGH, DPEPO host matrices at 10% wt loading, and neat films, (a) recorded at 300 K, and (b) 80 K. These measurements were performed using 355 nm excitation.

Comparing the absolute intensity of DF regime as a function of temperature, it is evident that at 80 K, the intensity is approximately an order of magnitude lower than at 300 K. This suggests an efficient thermally activated rISC mechanism. Despite the similar kinetic decay traces for both 10% wt and 1% wt loaded films, the 10% loaded films demonstrate a quenching of the prompt emission and relatively less DF. This indicates that in these films, a portion of the initial excited states is being quenched.

5.2.3 DF emission as functions of the laser excitation dose in solid films:

To confirm that the origin of the DF emission is indeed from the TADF mechanism, an analysis of the intensity dependence of the DF emission within the DF region was investigated as a function of the laser excitation dose (Figure 5.10). Across all scenarios, regardless of

ACRSA concentration, host, or even neat film, a consistent linear relationship in excitation power dependence for the DF emission was observed. This finding suggests that in all cases, the DF emission arises from a monomolecular process, fully in line with rISC.

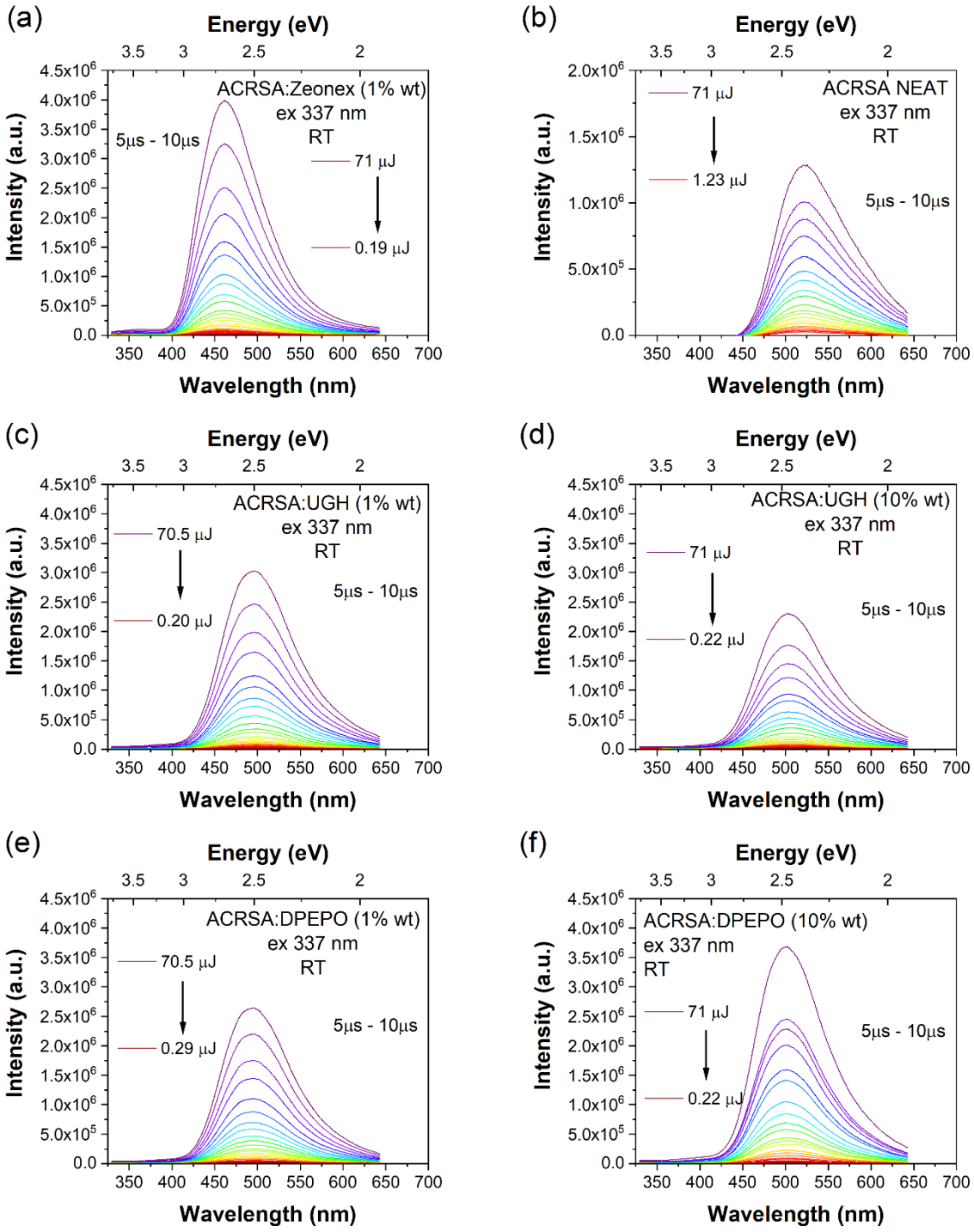

Figure 5.10: DF emission spectra as function the laser excitation dose of **ACRSA** in different host matrices at 1% and 10% wt loading, and neat films. These measurements were performed at room temperature, using 355 nm excitation wavelength.

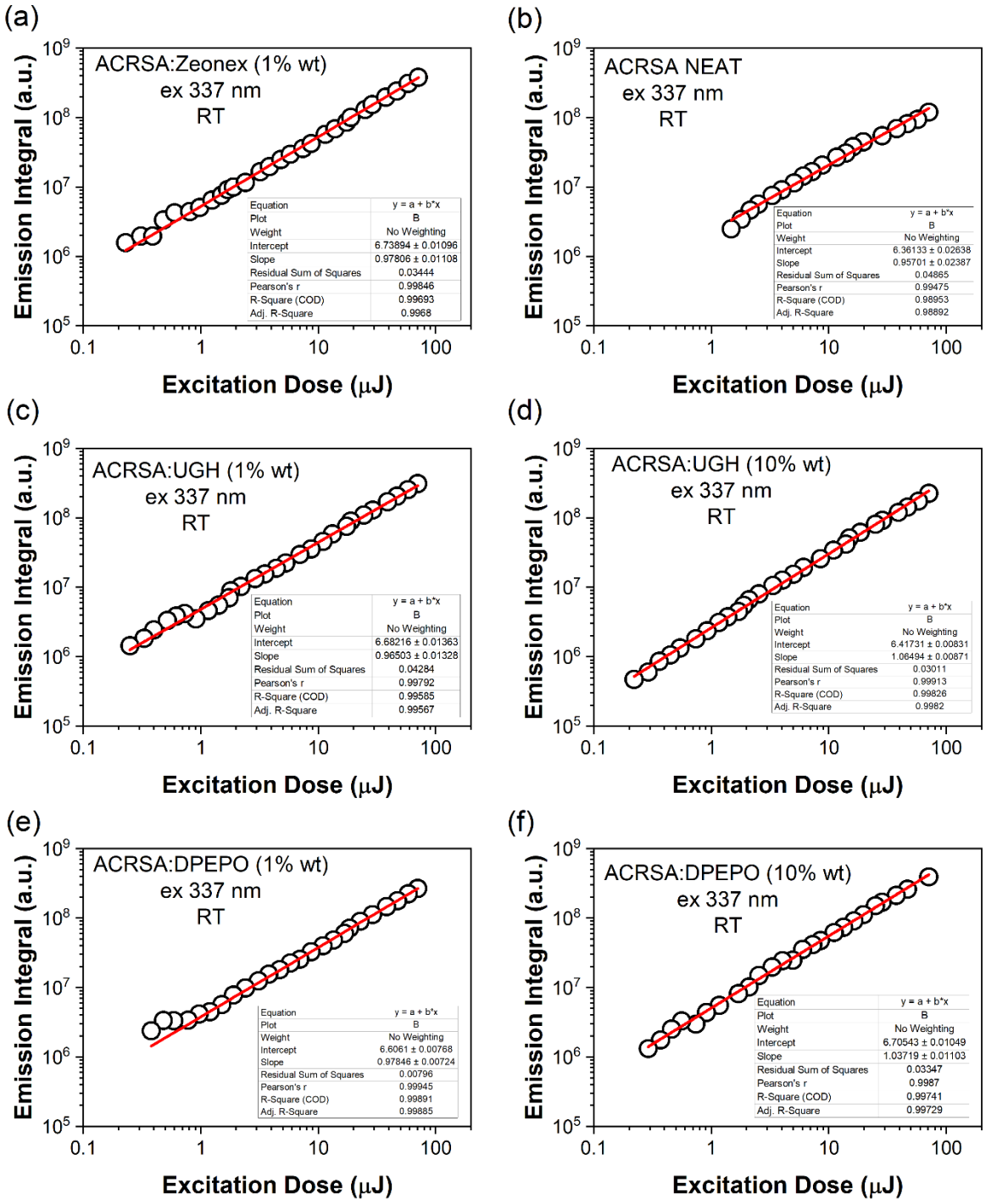

Figure 5.11: Linear fit of the DF emission intensity as a function of excitation power for **ACRSA** in different host matrices at 1% and 10% loading, and neat films. These measurements were performed at room temperature, using 355 nm excitation.

5.2.4 Energy ordering in solid films:

For deeper understanding of this energy ordering, the optical singlet–triplet gap, ΔE_{ST}, was determined for **ACRSA** in both zeonex (Figure 5.4) and DPEPO (Figure 5.5) at 1% wt concentration. As shown in the previous sections, the time-resolved emission spectra of **ACRSA**:zeonex film at room temperature reveals that the energy of the ^{1}CT energy state

stabilises (with no further red shifting observed) after *ca.* 36 ns with an onset of 400 nm. While the onset of the lowest triplet state energy from the phosphorescence was at 412 nm (3.01 eV). Thus, $|\Delta E_{ST}|_{zeonex}$ = 93 meV. In DPEPO, ^{1}CT stabilises with an onset of 419 nm after a similar time delay. Although a vibronic well-structured phosphorescence spectrum is not observed for this film, a weak phosphorescence spectrum is detected at long delay times, with a similar onset of 413 nm. This suggests that this emission also originates from the same triplet excited state, resulting in $|\Delta E_{ST}|_{DPEPO}$ = 41 meV. Therefore, similar to the behaviour in solution, the energy ordering in DPEPO changes so that both ^{1}CT and ^{3}CT have lower energy than the lowest ^{3}LE excited state (anthracenone (1^3A_2) nπ^*), classifying it as a type III TADF emitter (Figure 2.9iii).[80]

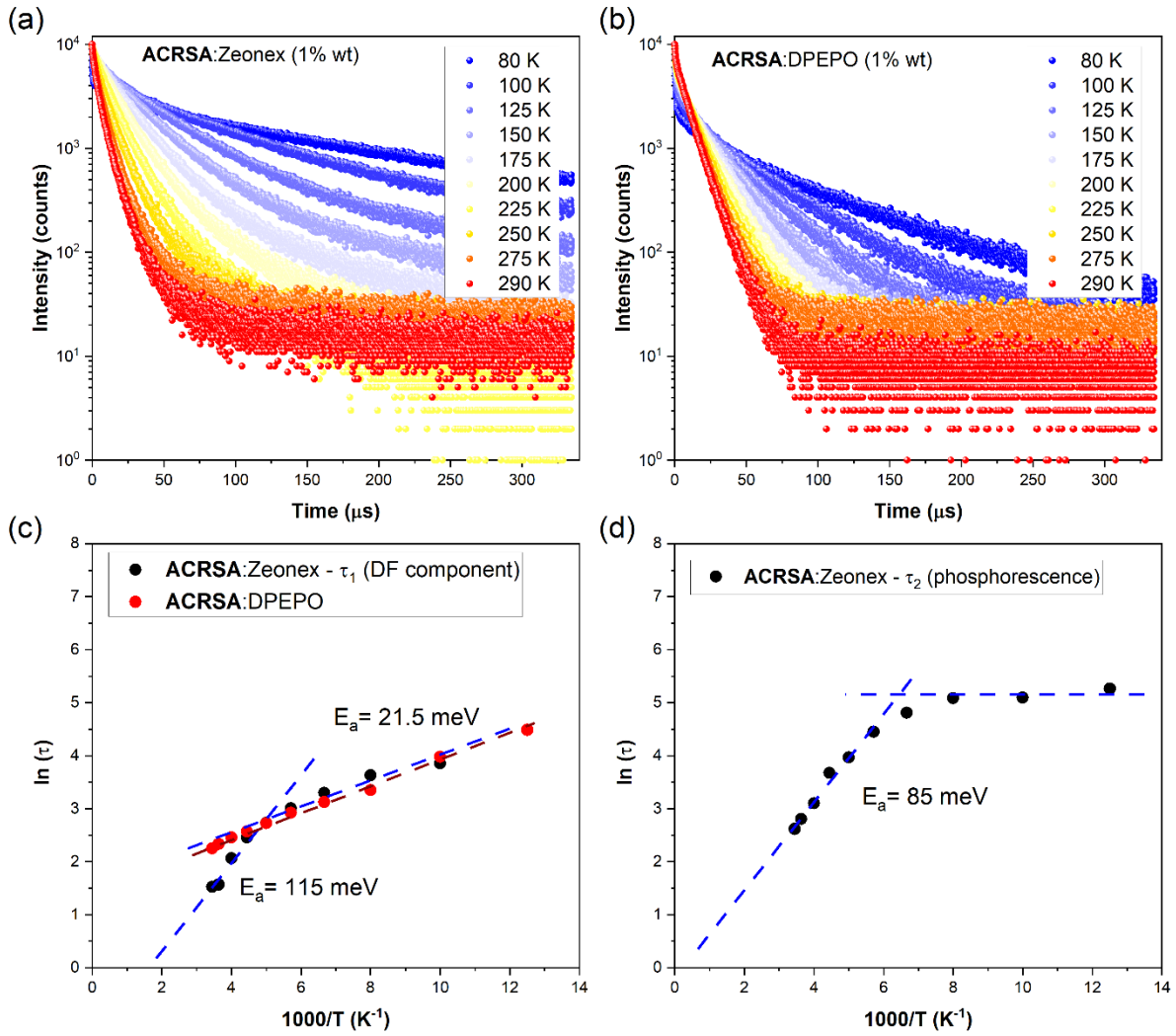

Figure 5.12: Photoluminescence decay as a function of the temperature in (a) **ACRSA**:zeonex and (b) **ACRSA**:DPEPO films (at 1% concentration), collected at 450 and 490 nm, respectively. All measurements were performed using an excitation source of 330 nm. Temperature dependence of the decay lifetime fitted using a model described in the section 3.4.3. (c) Comparison of the DF component lifetime of **ACRSA**:zeonex (τ_1) and **ACRSA**:DPEPO and (d) phosphorescence component lifetime of **ACRSA**:zeonex (τ_2).

To investigate the influence of temperature on this energy ordering, time-correlated single photon counting was performed in the DF regime as a function of temperature. Longer DF lifetimes were observed at low temperature for **ACRSA** in both matrices (Figure 5.1), consistent with the suppression of thermally activated rISC. While the DF regime of **ACRSA**:DPEPO (Figure 5.12b) follows monoexponential decay, the DF decay of **ACRSA**:zeonex (Figure 5.12a) was fitted with biexponential function (Table 5.1). In DPEPO, the DF lifetime increases from 9.5 μs at room temperature to 53.4 μs at 100 K. Similarly, both lifetimes in **ACRSA**:zeonex exhibit temperature dependence: τ_1 increases from 4.6 μs at room temperature to 47 μs at 100 K, while τ_2 increases from 13.7 μs at room temperature to 163.5 μs at 100 K, with τ_2 contributing more significantly on the overall decay at lower temperatures. Consequently, τ_1 is attribute to the DF regime, whereas τ_2 corresponds to the phosphorescence contribution.

Table 5.1: Lifetimes and amplitudes as a function of temperature. All data obtained by fitting photoluminescence decay of **ACRSA** in Zeonex (1%) and DPEPO (1%); with 330 nm excitation wavelength.

Temperatures (K)	**ACRSA:**Zeonex 1%		**ACRSA:**DPEPO 1%
	τ_1 (μs) / A_1 (%)	**τ_2 (μs) / A_2 (%)**	**τ_1 (μs)**
290	4.6/81	13.7/19	9.5
275	4.8/81	16.6/19	10.3
250	7.9/81	22.3/19	11.7
225	11.7/92	39.4/8	13.1
200	15.4/92	52.9/8	15.3
175	20.3/93	85.8/7	18.6
150	27.1/92	122.9/8	22.8
125	37.9/88	161.7/12	28.6
100	47.4/64	163.5/36	53.4

The temperature-dependent DF lifetimes (τ_1 component of **ACRSA**:zeonex) were fitted using an Arrhenius model to estimate the activation energy (E_a) for each process (Figure 5.12c). An activation energy of 21.5 meV was obtained for **ACRSA**:DPEPO, slightly lower than optically obtained ΔE_{ST}. For, **ACRSA**:zeonex, two activation energies were identified, along with a critical temperature of around 220 K. Below this critical temperature, a very similar behaviour to that of **ACRSA**:DPEPO was observed, with an activation energy of 21.5

meV. However, above the critical temperature, the DF accelerated significantly, resulting even shorter lifetimes than **ACRSA**:DPEPO, and an activation energy of 115 meV.

A small contribution from T_2 anthracenone (1^3A_1) $\pi\pi^*$ has been previously identified in the phosphorescence spectra of zeonex (Figure 5.4). Thus, the energy gap between T_1 anthracenone (1^3A_2) $n\pi^*$ and T_2 anthracenone (1^3A_1) $\pi\pi^*$ is estimated through the optical spectra to be around 115–145 meV. This indicates that the high temperature activation energy represents rIC between these two anthracenone triplet excited states. The presence of two E_a values and regimes implies that DF in **ACRSA**:zeonex arises from two mechanism. Below the critical temperature, the DF mechanism mirrors that of **ACRSA**:DPEPO. Given the type III TADF behaviour in DPEPO, this confirms the occurrence TADF through the second-order vibronic coupling mechanism. Indeed, this coupling, as demonstrated by Gibson *et al*,[78] displays weak temperature dependence, as the vibronic coupling dominates the interaction.

Above the critical temperature, effective and competitive rIC occurs between T_1 and T_2 triplet excited states. The population promoted into the T_2 state can then undergo El-Sayed-allowed rISC, populating from the anthracenone (2^1A_2) $\pi\pi^*$ triplet excited state to the singlet excited state, which subsequently emits light. Surprisingly, at higher temperatures, the DF lifetime in **ACRSA**:zeonex is accelerated, even faster than that observed in **ACRSA**:DPEPO. This result is unexpected, considering the larger ΔE_{ST} and the DF spectrum with mixed LE/CT character. However, the dual-channel DF competes more effectively with both radiative and non-radiative decays from the anthracenone (1^3A_2) $n\pi^*$ triplet excited state.

In contrast, for **ACRSA**:DPEPO classified as type III TADF, the lowest triplet state is ^{3}CT. This state has a very small (if any) phosphorescence rate and probably very weak non-radiative decay to the ground state. Consequently, it does not compete with rISC, only mediated by vibronic coupling. Thus, rIC to mediate DF is not observed at high temperatures, since the entire triplet population is in the ^{3}CT state instead of the anthracenone (1^3A_2) $n\pi^*$ local T_1 triplet excited state. As discussed in the previous chapter, due to the orthogonality of the D and A units, no IC between the local anthracenone singlet and ^{1}CT is observed. Consequently, it suggests that rIC is ineffective in populating the local T_2 state from ^{3}CT excited state.

When the τ_2 lifetime component (phosphorescence lifetime) is plotted as a function of the temperature, an initial strong temperature dependence is revealed. This suggests a non-radiative quenching with an E_a of 85 meV (685 cm^{-1}), possibly associate with the high-frequency C–H modes of anthracenone. This value is also close to the E_a for rIC. Consequently, this might indicate a competition between the rapid transfer of the triplet population of T_1 to

T_2 through rIC, and non-radiative and radiative decay of the triplet population of T_1 through phosphorescence. However, below 150 K, this competition switches off due to the suppression of both rIC and non-radiative decay. This leads to the phosphorescence lifetime approaching its natural lifetime of around 200 µs in this case (Figure 5.12d).

Lastly, Figure 5.13 illustrates the mechanism that drives the TADF mechanism in these both films: **ACRSA**:zeonex, classified as Type I, and **ACRSA**:DPEPO, classified as Type III TADF molecule.

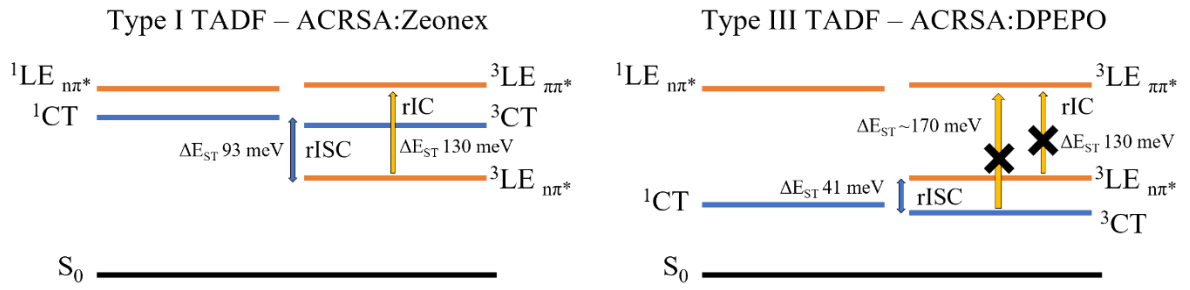

Figure 5.13: Schematic energy level diagrams of **ACRSA** in zeonex and DPEPO (1% wt loading).

5.3 Conclusions:

The spiro-TADF emitter, **ACRSA**, was studied in various host matrices with loading at 1% wt and 10% wt, and compared results to neat films. This study was also compared with the measurements of **ACRSA** in solution, as shown in the previous chapter, which revealed the emissive singlet and triplet excited states of **ACRSA**, as well as the changes in these states with the solvent polarity. In solid state at 1% wt loading, a single CT emission around 485 nm, consistent with all host matrices and without significant spectral changes over 20 µs. This shows that no variation in dihedral angle between the D and A units occurs due to the rigid spiro bridge, yielding consistent CT state energy and rISC rate, and avoiding power law tail in DF decay kinetics. This contrasts with D–A TADF systems utilising a flexible C–N bond bridge, which gives rise to significant inhomogeneous rISC rates and CT energies in solid state, causing unwanted spectral broadening. At 1% **ACRSA** loading, DPEPO, UGH, and neat films display minimal differences. Particularly, the pure ^{1}CT emission in these films is less red shifted compared to toluene solution.

In small molecule hosts with low **ACRSA** loadings, the host materials' higher dielectric constant stabilises the CT state, resulting in efficient processes and monoexponential decay for DF regime. This indicates a homogeneous system. Surprisingly, despite being a spiro TADF molecule, at a 10% loading and in a neat film, strong effects are attributed to the intermolecular interactions between neighbouring **ACRSA** molecules. Consequently, a lower energy CT state

emerges, contributing to slow DF. This state also induces low energy phosphorescence, potentially allowing this associated triplet excited state to independently mediate rISC.

At low temperatures, particularly in zeonex, the phosphorescence exhibits a well-defined structure with 0.19 eV vibronic progression, indicating a strong coupling to the acceptor's C=O stretching mode. Consequently, this identified the lowest energy local triplet state as an acceptor ^{3}nπ* state. Additionally, a prolonged, unstructured phosphorescence appears at higher energy levels, attributed to the acceptor $^3\pi\pi$* state.

The effect of the triplet excited states in the energy ordering has a significant impact on the TADF. In the case of DPEPO, the lowest energy state is the ^{3}CT triplet state, which has highly limited radiative and non-radiative decay paths. As a result, this state serves as a stable reservoir for the triplet population, leading to a straightforward rISC process driven by vibronic coupling, with weak temperature dependence. On the other hand, in zeonex, where the lowest energy state is the ^{3}LE, various competing DF processes emerge. The efficient and rapid phosphorescence of the lowest anthracenone (1^3A_2) nπ* local triplet state of **ACRSA** dominates at lower temperatures. As temperature rises, increased vibronic coupling accelerates the rISC rate, so the DF mechanism to overtake radiative decay from phosphorescence. At a critical temperature of 220 K, a different mechanism is observed in zeonex, where the T_2 originating from the anthracenone, (1^3A_1) $\pi\pi$* triplet excited state, is populated by rIC. This state can readily undergo El-Sayed-allowed rISC to the (2^1A_2) $\pi\pi$* singlet excited state, leading to DF emission. Despite its larger E_a, this allowed rISC exhibits a higher rate compared to vibronic coupling SOC, becoming dominant at higher temperatures. In contrast, in DPEPO at elevated temperatures, all triplet population still resides in the ^{3}CT state, which lacks coupling to the anthracenone (1^3A_2) nπ* local triplet excited states. Consequently, the ordering of triplet energy yields distinct TADF behaviours, with even subtle environmental changes can induce significant shifts in the TADF mechanism.

As a result, this study demonstrates that **ACRSA** establishes a new blueprint for highly efficient TADF emitters. This is attributed to its robust molecule and the elimination of the weak C–N bridging bond between D and A. The structural rigidity of **ACRSA** is of great importance, as it remains immune to distortions of the D-A dihedral bond induced by host packing. Consequently, it lacks a prolonged tail of slowly decaying DF states. The extended residency times of triplet excitations in these states would otherwise be more susceptible to triplet polaron annihilation, a major cause of emitter degradation. Therefore, **ACRSA** is expected to yield longer device operating lifetimes than C-N TADF molecules.

6 Probing non-emissive excited states: insights into the excited states involved in the TADF mechanism

This chapter uses pump-probe techniques because of their ability to provide an in-depth study of dark excited states, for mapping and providing insights into the excited states involved in the TADF mechanism. For better understanding of the techniques and the mechanism itself, I will study a benchmark emitter **DMAC-TRZ**, as substantial research has been conducted on this molecule. Initially, I will combine pump-probe techniques with standard photoluminescence measurements to identify the electronic excited states involved in key transitions and their nature. Given that increasing solvent polarity triggers a reorganisation of the excited state energy levels, I will investigate the dependence of the photoinduced absorption signal on polarity, as well as the impact on the oscillator strength of transitions. Specifically, I will explore the effect of the solvent in the local triplet excited state transition and its interaction with the ^{3}CT excited state. Subsequently, I will extend the understanding from the slow processes, studied by the nanosecond transient absorption, to the rapid processes using ultrafast transient absorption.

The work presented in this chapter has been recently submitted for publication.

6.1 Overview:

Due to the CT character of the excited states present in the TADF molecules, the emissive properties are highly dependent on the environment.[128] Given the different sensitivity of CT to the specific environmental properties when compared to the LE states, *e.g.* polarity/polarizability, a change in the relative energy ordering of the TADF molecular excited states is expected in different environments.[87,127] Thus, different scenarios for energy ordering can be achieved.[78,96] One scenario considers the CT states (both ^{1}CT and ^{3}CT) assuming energetically lower value than ^{3}LE and then quenching the ^{3}LE excited state (likely the emissive triplet excited state). Photoluminescence emission and lifetimes are often used to study the excited state of TADF molecules.[43,103] However, these methodologies rely heavily on the excited states being emissive, and do not easily give information about the dark excited states involved in the TADF process such as ^{3}CT.[133,134]

For this investigation, **DMAC-TRZ** (molecular structure shown in Figure 6.1) was selected as a TADF molecule benchmark, as considerable work has already been reported for this molecule. This molecule was initially introduced by Tsai *et al.*,[107] which showed efficient TADF emitter with high PLQY (≥90%) in doped films, along with highly efficient TADF

OLEDs (achieving EQE of 26.5%). Given its remarkable performance, this molecule gained our attention. In 2020, we conducted a study that explored interactions between **DMAC-TRZ** and diverse hosts, aiming to comprehend the influence of these interactions on photophysical properties.[87] In particular, my involvement in this work included performing optical spectroscopy on the solid-state films. Notably, our recently findings highlight the existence of two distinct stable conformers within the **DMAC-TRZ** molecule: a quasi-axial (QA) and a quasi-equatorial (QE) conformer.[135] The appearance of these two conformers was somewhat unexpected but has demonstrated its strong photophysical behaviour in non-polar solvents and solid-state. Surprisingly, under specific conditions, an emission band at 390 nm is observed, attributed to a QA conformer, despite the strong contribution of the QE conformer (around 450 nm). Given the spectral overlap between these two conformers, it has been demonstrated that Förster resonance energy transfer (FRET) is efficient, leading to a dominant contribution of emission from the QE conformer. In this research, my main contribution involved employing time-correlated single photon counting (TCSPC) techniques to explore the energy transfer between these two conformers. However, it is important to note that I will not provide a detailed description of these findings in this chapter, as they will constitute a separate section within another PhD thesis.

Therefore, in this chapter, I will explore photoinduced absorption techniques to map the excited states of **DMAC-TRZ** in different environments, unconstrained by the limitation of focussing only on emissive states. The transitions and the nature of the electronic excited states involved in rISC were identified by combining quasi-CW and transient photoinduced absorption (both flash photolysis and ultrafast) with standard photoluminescence measurements. Moreover, the reorganisation of excited states with increasing solvent polarity was observed, which leads to quenching of the $T_1 \rightarrow T_n$ induced absorption when ^{3}CT becomes the lowest triplet excited state. Lastly, the ultrafast transient absorption reveals evidence that rapid solvent reorganisation strongly affects the oscillator strength of the singlet excited state transitions.

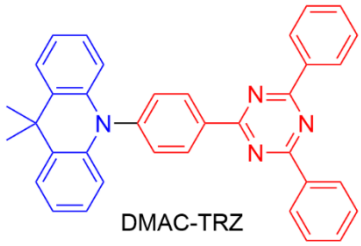

Figure 6.1: Molecular structure of the 10-(4-(4,6-Diphenyl-1,3,5-triazin-2-yl)phenyl)-9,9-dimethyl-9,10-dihydroacridine (**DMAC-TRZ**).

6.2 Results and Discussion:

6.2.1 Quasi-CW photoinduced absorption:

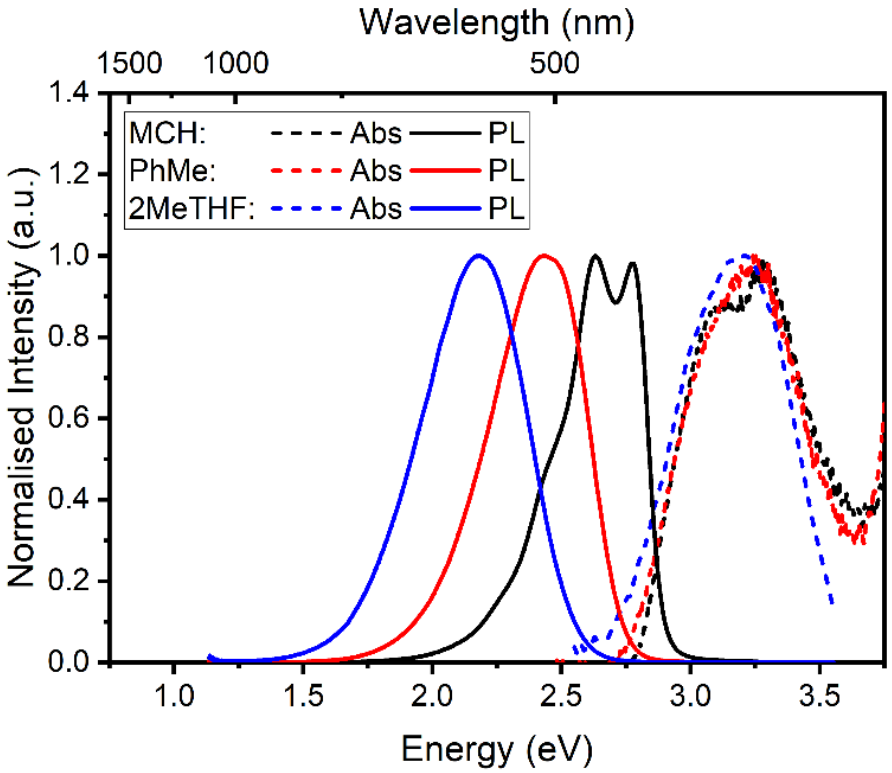

Figure 6.2: Normalised absorption (dashed lines, 20 µM) and emission spectra (solid lines, 0.8 mM) of **DMAC-TRZ** in methylcyclohexane (MCH), toluene (PhMe), and 2-methyltetrahydrofuran (2MeTHF). λ_{exc} = 365 nm.

For reference, linear absorption and emission as a function of solvent are given in Figure 6.2, highlighting the CT characteristics of the molecule by increasing solvent polarity. Quasi-CW photoinduced absorption (PIA) measurements were performed on concentrated (0.8 mM) solutions to study the energy ordering of the electronic excited states in **DMAC-TRZ**. All measurements were made at room temperature in oxygen-free solution. Using PIA measurements, both emissive and non-emissive excited states can be probed, which broadens insight into the excited state landscape beyond the information obtained from emission spectroscopy alone. The apparatus is described in the section 3.3.3, and allows absorbance features of the excited states (including absorbance features of triplet excited states, photoinduced by the 375 nm pump beam) to be detected through changes in transmission of an overlapping probe beam. The phase of the lock-in amplifier signal also allows to broadly distinguish spectral features which are either directly in-phase (X channel) with the pulsed pump beam, as well as those occurring indirectly (out of phase, Y channel).

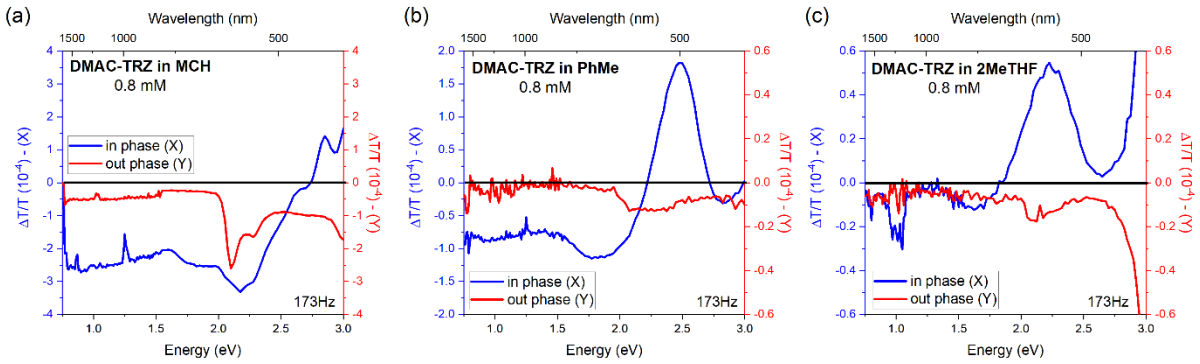

Figure 6.3: Quasi-CW photoinduced absorption of **DMAC-TRZ** in (a) methylcyclohexane (MCH), (b) toluene (PhMe) and (c) 2-methyltetrahydrofuran (2MeTHF) solutions at 0.8 mM. λ_{exc} (pump) = 375 nm.

Figure 6.3 shows the PIA spectra of **DMAC-TRZ** in three different solvents: methylcyclohexane (MCH), toluene (PhMe) and 2-methyltetrahydrofuran (2MeTHF) at 0.8 mM. At this relatively high concentration, necessary for achieving good PIA signal to noise, additionally time-resolved photoluminescence measurements were performed. The results showed similar spectra and lifetimes as in very low concentration solutions,[87] indicating no significant dimer/excimer formation occurs at the higher concentrations (Figure 6.4). The PIA spectra of **DMAC-TRZ** in all solvents gave signals in phase (X) as well as out of phase signal (Y) with respect to the excitation pulse train (in this case f =173 Hz). The signals observed in phase arise from transitions of short lifetime (relative to 1/f of the excitation pulse train, i.e. around 6 ms), whereas the out of phase signals are from long lifetime transitions (usually related to triplet transitions). The PIA spectra for all solutions showed a positive ΔT/T feature in the X channel at high energies (Figure 6.3), which is observed to spectrally overlap with the photoluminescence (PL) spectra in each solvent, Figure 6.2. This is ascribed to either the direct collection of a photoluminescence signal or stimulated emission (SE) of **DMAC-TRZ**, which follows the PL solvatochromism (as seen in Figure 6.2). At higher energy above the SE we observe a ΔT/T contribution from photobleaching of the ground state transition, e.g. in PhMe the PIA becomes negative above 2.7 eV, Figure 6.3b. Induced absorption (-ΔT/T) was also observed in both X and Y channels. In both MCH and PhMe, a broad negative induced absorption in the X channel indicates an overlap of signals originating from various electronic transitions.

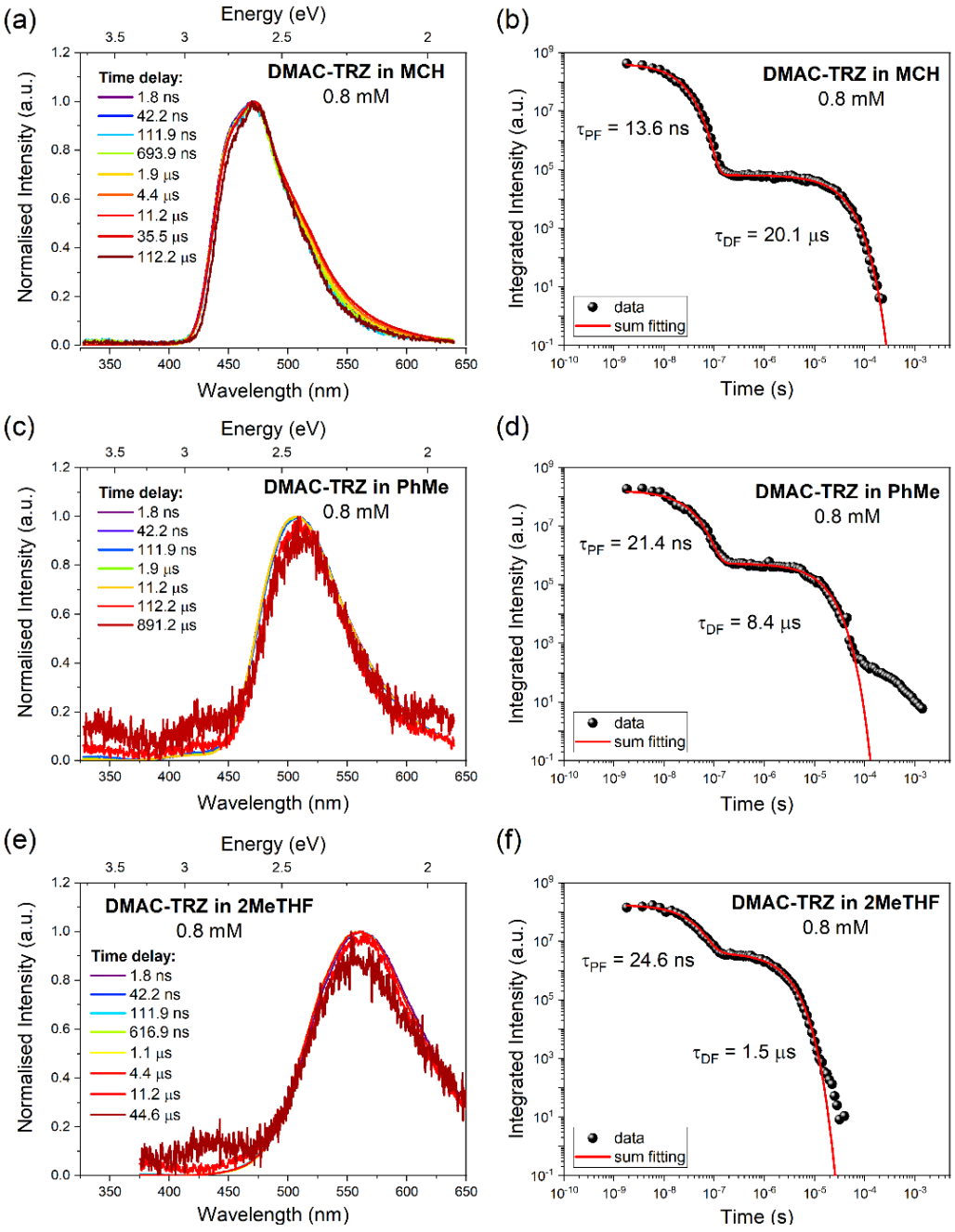

Figure 6.4: Time-resolved emission spectra and kinetic decays of **DMAC-TRZ** in (a-b) MCH, (c-d) PhMe, and (e-f) 2MeTHF solutions, at 0.8 mM concentration. All measurements were performed in degassed solutions at room temperature, using a 355 nm excitation source. The data are fitted using a biexponential function.

The induced absorption in both X and Y channels become significantly weaker with increasing solvent polarity. Higher polarity solvents decrease the oscillator strength (f) of CT transitions, indicating that the PIA bands observed here in the X-channel are most likely from the first excited CT states to upper high energy CT states (i.e. $^1CT_1 \rightarrow {}^1CT_n$). Two induced bands (~1.75 eV and ~1.0 eV) have much lower intensity in higher polarity solvents (2MeTHF), but their band positions remain the same. As the transition energies are unaffected in all solvents this confirms that these two transitions, ($S_1 \rightarrow S_n$ and $S_1 \rightarrow S_m$) are between states having the

same character, i.e. LE to LE or CT to CT, but not LE to CT or CT to LE (which would be affected differently by solvent polarity, thus shifting the band position). In the Y channel, a well-defined structured induced absorption band around 2.1 eV is observed in MCH solution, indicating a state with strong local character and with long lifetime, a transition likely coming from the lowest triplet excited state of the molecule ($T_1 \rightarrow T_n$). As mentioned previously, our recent report demonstrated that **DMAC-TRZ** in non-polar solvent displays two distinct stable excited state conformers:[135] a quasi-axial (QA) and a quasi-equatorial (QE) conformer (Figure 6.5). By exciting at 3.30 eV (375 nm, the pump wavelength), both QA and QE can be independently populated. Also, Dexter energy transfer from the QE to the QA triplet excited state populates the lowest triplet excited state in MCH, which shown to be the QA triplet excited state.[135] Thus, the strong and vibronic transition observed in the Y channel ($T_1 \rightarrow T_n$) we assign to the $^3LE_1 \rightarrow {}^3LE_n$ of the QA conformer. This is in good agreement with previous calculations, which demonstrates the triplet excited state of QA have a stronger LE character, while QE have CT character.[135]

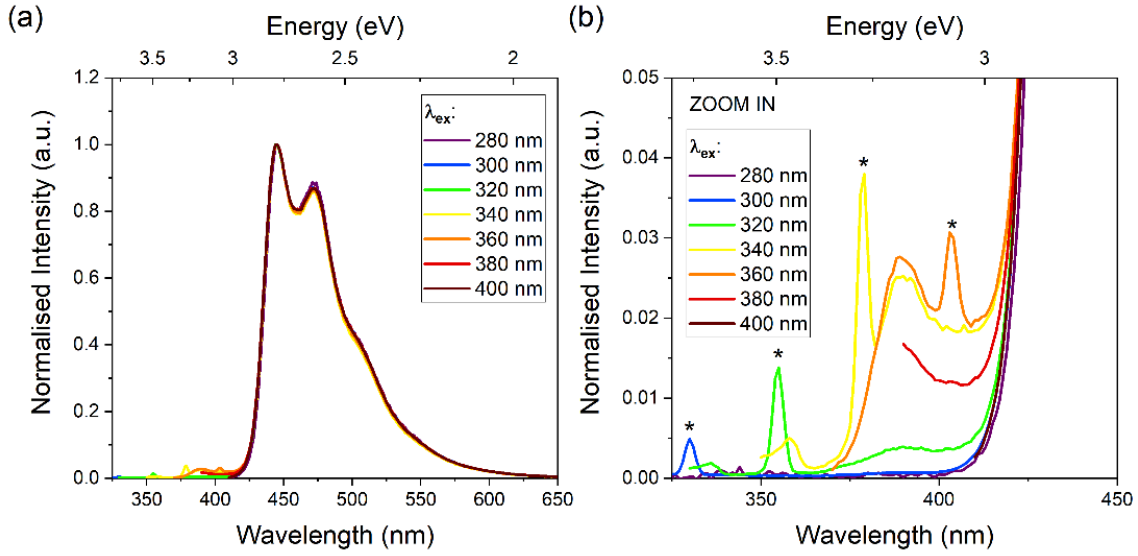

Figure 6.5: (a) Photoluminescence spectra of **DMAC-TRZ** in MCH solution excited at different wavelengths, at 20 µM concentration. (b) Zoom in on the photoluminescence spectra to highlight the QA conformer dependence on the excitation wavelength. *Solvent Raman peaks.

As solvent polarity increases, this structured long lived signal is effectively quenched, e.g. in 2MeTHF, where a little excited state population in Y channel can be seen (longer lifetimes). The higher polarity solvents not only destabilise the QA conformer, but also significantly increase the CT character and relaxes the energy of the QE conformer which then becomes the lowest excited triplet state of the system (^3CT).

6.2.2 Transient photoinduced absorption (nsTA):

Transient photoinduced absorption measurements (nsTA) were performed on the same solutions to help assign these transitions observed in the CW-PIA spectra (Figure 6.6). In this technique, the lock-in detection of CW-PIA is replaced with a fast photodiode and oscilloscope, in order to monitor the kinetics of a specific transition directly. Measurements were collected both with the white light probe beam off (pump only background, also corresponding to PL) and with both pump and probe beams overlapping (TA), which allows to obtain both photoluminescence and the induced absorption lifetime, respectively. Decay traces obtained by probing different energies of MCH, PhMe and 2MeTHF solutions are shown in Table 6.1, with the selected energies informed by the previous CW-PIA spectra. Note that in some measurements the oscilloscope vertical scale was deliberately chosen in a way that saturates the early signal (corresponding to prompt fluorescence), in order to achieve adequate resolution of the delayed signal.

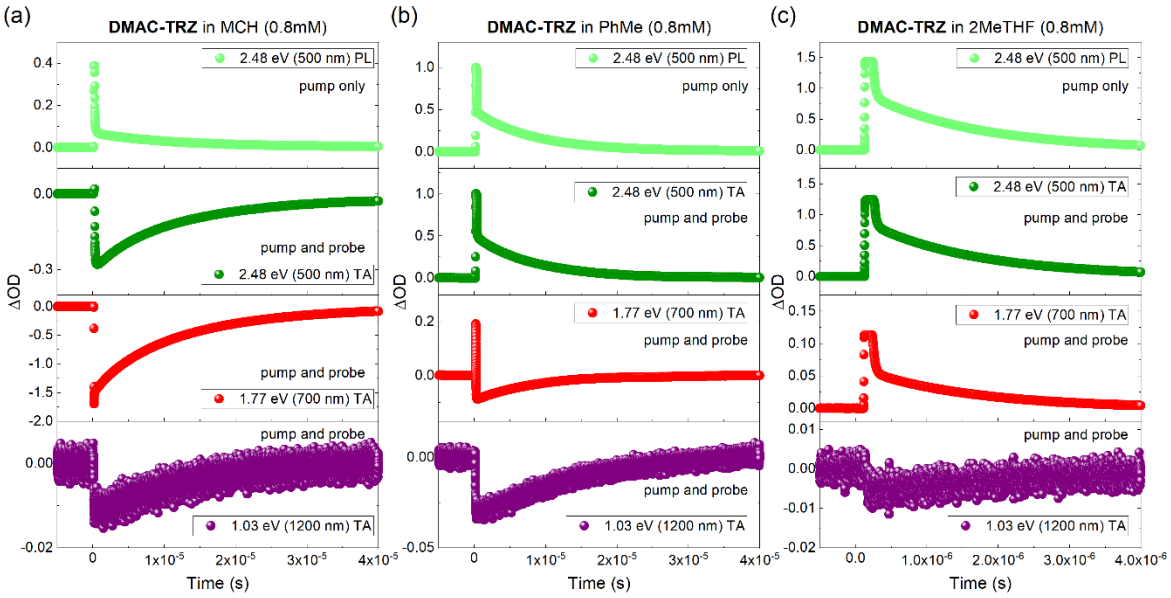

Figure 6.6: Transient photoinduced absorption of **DMAC-TRZ** in (a) MCH, (b) PhMe and (c) 2MeTHF. The measurements were collected at 2.48 eV (500 nm), with the pump only (PL) and pump and probe (TA), at 1.77 eV (700 nm) with the pump and probe (TA) and at 1.03 eV (1200 nm) with the pump and probe (TA). λ_{exc} (pump) = 355 nm.

Lifetimes estimated from the fitting of nsTA measurements are in good agreement with the lifetimes estimated from the fitting of time-resolved photoluminescence decay (Figure 6.4). The broad negative band (-ΔT/T) observed in the X channel of PIA (at *ca*. 2.2 eV and 1.77 eV) has a lifetime of around 11.6 µs for MCH, 8.4 µs for PhMe and 1.5 µs for 2MeTHF. By comparing with the photoluminescence decay, these species were assigned to be responsible for the delayed fluorescence (DF). As previously reported,[87] the DF component of **DMAC-TRZ** is a radiative decay from ^{1}CT, mediated by the triplet excited states. Therefore, the X

channels PIA signal is related to an induced absorption transition from ^{1}CT to upper singlet excited states (S_n), and this transition in nsTA measurements decays at the same rate as the PL itself. As discussed above, the nature of the upper singlet excited states is identified by the unchanged energy transition at different solvent polarities. This confirms that the energy transitions observed in the PIA X channel induced absorption are $^1CT_1 \rightarrow {}^1CT_n$ and $^1CT_1 \rightarrow {}^1CT_m$ transitions. In the Y channel, the peak of induced absorption presented a lifetime of around 0.14 ms in both MCH ($-\Delta T/T = 2.5\times10^{-4}$) and PhMe ($-\Delta T/T = 0.5\times10^{-4}$) solvents, which is assigned to be a transition from the QA conformer $^3LE_1$ to upper triplet states (^3LE_n) based on the strong vibronic character of the transition. In 2MeTHF, this longer lifetime Y channel signal is significantly weaker ($-\Delta T/T = 0.1\times10^{-4}$) because the ^{3}CT state of QE becomes the lowest triplet excited state of the molecule, relaxed energetically below the ^{3}LE state, which quenches the ^{3}LE QA state.

Table 6.1: Lifetimes obtained from the fitting of transient photoinduced absorption of **DMAC-TRZ** in MCH, PhMe and 2MeTHF solutions at 0.8mM. The lifetime and the estimated rates were obtained from the kinetics of the photoluminescence decay (λ_{exc} = 355 nm) (Figure 6.4).

DMAC-TRZ		**MCH**	**PhMe**	**2MeTHF**
2.48 eV/500 nm	PL	13.3 µs	8.6 µs	1.5 µs
	TA	11.6 µs (91.4%)/ 0.14 ms (8.6%)	8.2 µs	1.5 µs
2.06 eV/600 nm	PL	-	8.6 µs	1.6 µs
	TA	11.5 µs (92.2%)/ 0.16 ms (7.8%)	8.4 µs (93%)/ 0.12 ms (7%)	1.5 µs
1.77 eV/700 nm	PL	-	-	1.5 µs
	TA	13.2 µs	8.1 µs	1.5 µs
1.55 eV/800 nm	PL	-	-	1.5 µs
	TA	-	-	1.6 µs
1.03 eV/1200 nm	PL	-	-	-
	TA	11.5 µs	9.1 µs	2.9 µs
	Time-resolved photoluminescence decay			
^{1}CT (eV)		2.91	2.75	2.61
ΔE_{ST} (eV)		0.16	0	-0.14
PF		13.6 ns	21.4 ns	24.6 ns
DF		20.1 µs	8.4 µs	1.5 µs
k_F (s^{-1}) x10^7		6.03	2.05	1.69
k_{ISC} (s^{-1}) x10^7		1.33	2.63	2.37
k_{rISC} (s^{-1}) x10^4		6.05	27.1	163

In summary of this section, the proposed energy ordering of the excited states of **DMAC-TRZ** in MCH, PhMe and 2MeTHF is shown in Figure 6.7. By increasing the solvent polarity, a reordering of the excited states is observed, manifesting in a total change of the long lifetime signal, and monotonic decrease of band intensity with increasing polarity observed in the short lifetime signals. In the higher polarity medium, the significant reduction of *f* decreases the photoinduced absorption signal intensity as well as relaxing the absolute energies of all CT

states, so that the lowest energy ^{3}CT triplet state becomes the lowest overall triplet excited state, quenching the ^{3}LE state. Effectively, an alternative perspective on the mechanism is that, as the polarity increases, the lowest triplet excited state of the QA conformer, with its mixed LE/CT character, enhances the contribution of CT and relaxes to lower energies, driving the conformational change that impacts the populations of the different triplet states/conformers. These changes affect the lifetime of the triplet states, leading to the weaker absorption feature in the Y channel ($T_1 \rightarrow T_n$). Further experiments and calculations may be required to obtain additional information about the proposed mechanism. Consequently, the well-structured long-lifetime PIA band at 2.1 eV is only observed in MCH. This reordering of excited states then has a direct effect on the rISC rate; in MCH and PhMe, the rISC rates are 6×10^4 and 27×10^4 s^{-1} respectively, whereas in 2MeTHF it rises considerably to 1.6×10^6 s^{-1} (Table 6.1). The rISC rates values were estimated from the photoluminescence lifetimes, which was applied in a kinetic modelling according to *Haase et al.*[103] Thus, it is observed that as the energy ordering of the different triplet states changes, and the rISC rate can increase by two orders of magnitude, achieving a very high rISC rate in 2MeTHF. The increase in rISC rate when ^{3}CT relaxes below ^{3}LE is in very good agreement with the theoretical predictions of Gibson and Penfold.[79]

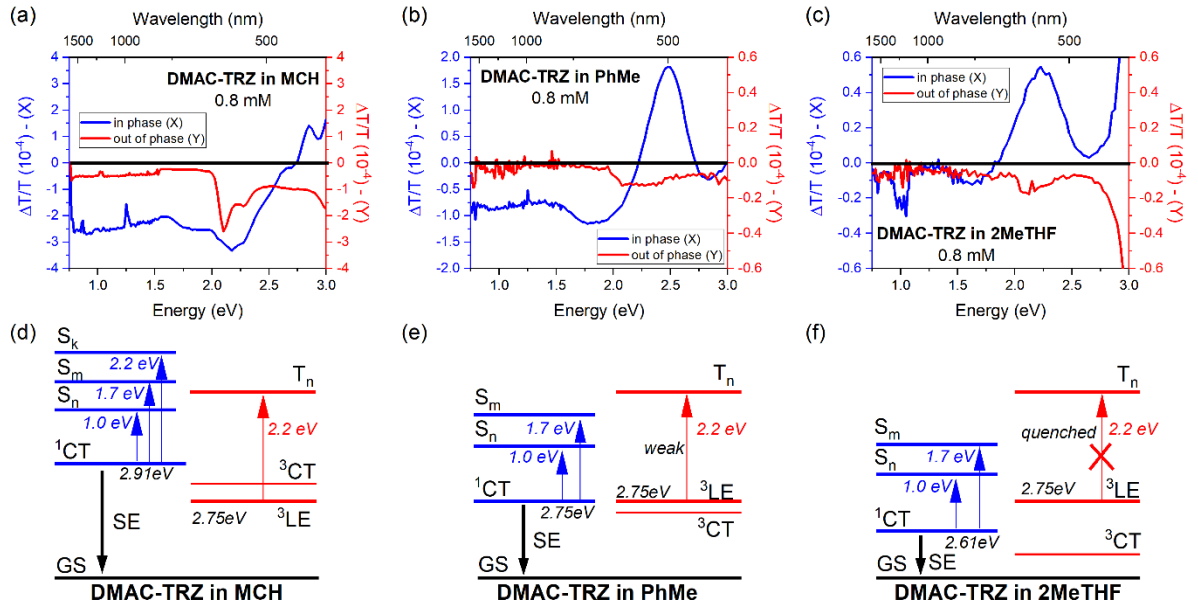

Figure 6.7: Proposed excited state energy diagram, representing the spectra obtained by the quasi-CW photoinduced absorption of **DMAC-TRZ** in different solvents.

6.2.3 Transient photoinduced absorption (fsTA):

To further analyse the broad negative PIA signal (-ΔT/T) in the X channel, ultrafast transient absorption (fsTA) on the sub-picosecond (top panel in Figure 6.8) as well as nanosecond time resolution (bottom panel in Figure 6.8) were performed. Figure 6.8a shows

an instantaneous vibronic structured induced absorption of **DMAC-TRZ** in MCH, with maxima at *ca.* 1.7 eV and 1.9 eV and the onset of a further feature at 1.5 eV. While the two peaks at 1.7 eV and 1.9 eV have similar decay lifetimes, the 1.5 eV TA feature has a different kinetic (Figure 6.9). This combined with the appearance of an isosbestic point at 1.6 eV suggests that two different species are present with overlapping induced absorption. As mentioned before, the QA and QE conformer of **DMAC-TRZ** can be seen in non-polar solvents. The QE conformer has a long fluorescence lifetime and so we attribute the vibronic absorption band with maxima of 1.7 and 1.9 eV to this conformer. While the very short lifetime QA conformer contribution gives rise to the short lived photoinduced absorption feature at 1.5 eV, which decays within 20 ps. This rapid decay of the QA conformer is likely due to a singlet excited state interconversion between the QA to the QE conformer. Despite a very small QA population observed in non-polar solvent,[135] as seen in Figure 6.5, strong absorption transitions are expected for this conformer due to its stronger *f* when compared to the QE conformer. Rapid decay at 1.5 eV of the induced absorption and the isosbestic point at 1.6 eV indicates interconversion between these two stable conformers. However, no evident grow in of the intensity of the photoinduced absorption feature at 1.7 and 1.9 eV coming from a ^{1}CT transition of the QE conformer was observed. This corroborates with no significant increase in the QE population from the QA interconversion, as its relative population is known to be very small. Interestingly, the singlet excited state interconversion of QA to QE conformer is highly dependent of the excitation wavelength. As shown in Figure 6.5b, the excess energy provided by the higher energy excitation accelerate the interconversion between the two conformers, leading to no detected emission from the QA conformer by exciting at 300 and 280 nm. Even though interconversion of the singlet excited state from the QA conformer were observed, in the triplet excited state the picture is different. The triplet excited state of the QA conformer is the lowest triplet excited state in MCH and it is mainly populated via Dexter energy transfer from the QE conformer. Its longer lifetimes (around hundred microseconds) suggests that the triplet excited state of the QA conformer do not interconvert to the QE conformer. Furthermore, as discussed above, the broad induced negative absorption ($-\Delta T/T$) measured in the quasi-CW photoinduced absorption comes from a ^{1}CT transition, which based on the transient absorption has strong mixed LE/CT character. Consequently, in a non-polar solvent MCH, it has a higher contribution of LE character, consistent with the strong vibronic structure observed for this transition.

While in MCH little reorganisation of the solvent dipoles around the excited **DMAC-TRZ** is expected, in a polar solvent, such as PhMe, this effect is much larger. Figure 6.8b (and

kinetic traces, Figure 6.9) shows that the vibronic structure band at 1.7 and 1.9 eV display an apparent intensity build-in time, *ca.* 17 ps. This could be due to solvent reorganisation upon excitation; an initial population of ^{1}CT is generated, which induces the reorganisation of the solvent dipole moment of the surrounding solvent shell. In this case, the solvent reorganisation stimulates a more LE character on this excited state, which consequently increases the *f* of the $^1CT_1 \rightarrow {}^1CT_n$ transition. A change in *f* as the build-in within 17 ps in the transient absorption signal can be detected, although this seems rather slow for such a process. Alternatively, this could also be achieved by a change in the dihedral angle between the donor and acceptor units away from 90^o to a smaller angle that gives more LE character and again higher *f*. This would be controlled by both solvent dipole strength and viscosity and could also account for the high PLQY of **DMAC-TRZ** in solution. Noteworthy, there is no increase observed in the SE intensity, suggesting that the population of the ^{1}CT excited state remains the same, indicating that the grow in of intensity of the PIA is not caused by an increase in the excited state population. Further, the QA contribution (induced absorption at 1.5 eV) becomes less pronounced in higher solvent polarity, as already reported.[135]

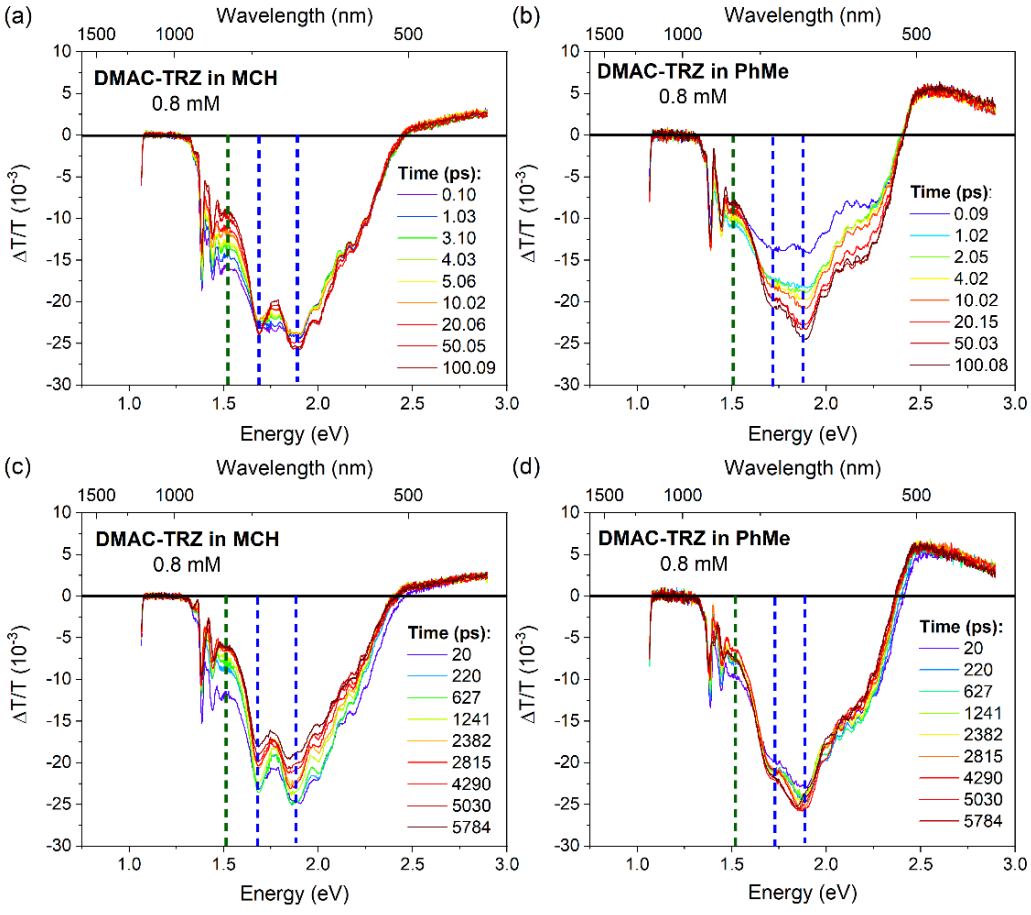

Figure 6.8: Picosecond transient absorption spectra (top panel) and nanosecond transient absorption spectra (bottom panel) of **DMAC-TRZ** in (a) MCH and (b) PhMe solutions at 0.8 mM. λ_{exc} (pump) = 343 nm (which direct excites CT transitions).

In the longer timescale fsTA (bottom panel in Figure 6.8c), a simple decay was observed decay in the transient absorption band of **DMAC-TRZ** in MCH. By fitting the decay curve (Figure 6.9), the lifetime was estimated to be around 18 ns, which is in good agreement with the 13.6 ns lifetime of the prompt component in the PL decay curve (Table 6.1). This indicates that we are probing the induced absorption from the ^{1}CT to ^{1}CT$_n$/^{1}CT$_m$ transition, as it has an identical lifetime as the ^{1}CT state. However, no decay in the transient absorption within the 6 ns time window of our PIA measurement in PhMe were observed (Figure 6.8). This indicates that the decay lifetime of this state has a much longer lifetime, which is expected for **DMAC-TRZ** from emission measurements to be around 21 ns in PhMe. Thus, the ultrafast transient absorption not only confirms the excited states responsible for photoinduced absorption signal in the X channel from quasi-CW photoinduced absorption, but also verifies the contributions two stable conformers. The ultrafast transient absorption provided insights on the dynamics of the solvent and /or molecular reorganisation induced by the polarity and how it can strongly affect the f by increasing the proportion of LE character on the singlet upper excited state transitions.

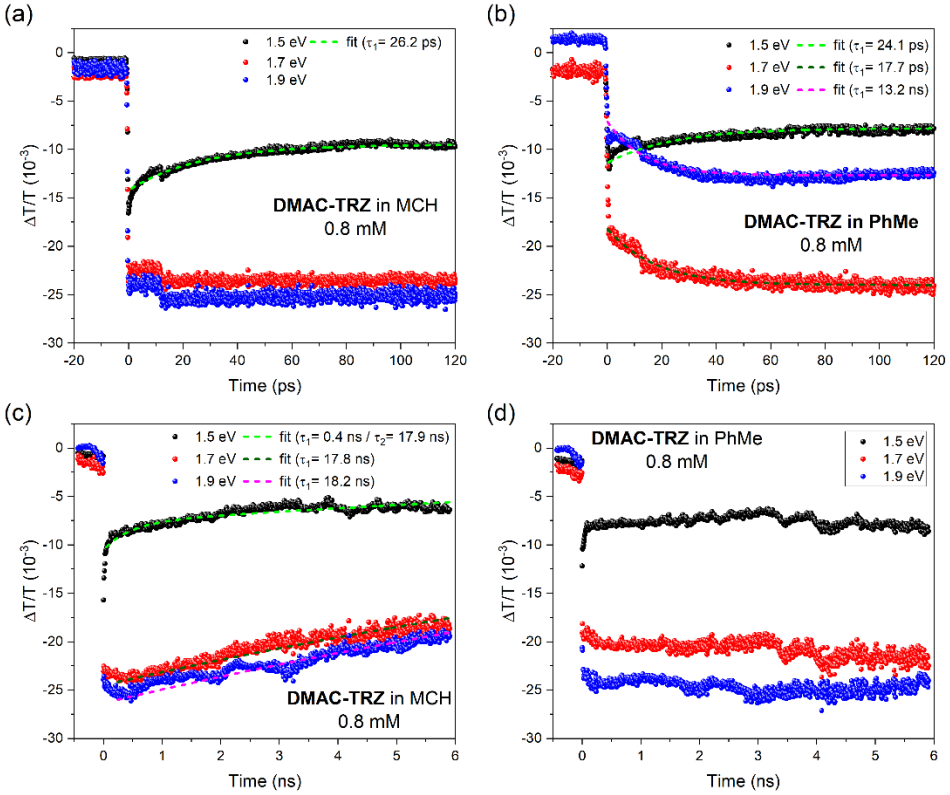

Figure 6.9: Picosecond transient absorption decay curves (top panel) and nanosecond transient absorption decay curves (bottom panel) of **DMAC-TRZ** in MCH (a and c) and PhMe (b and d) solutions at 0.8 mM, collected at 1.5, 1.7 and 1.9 eV. The data are fitted using monoexponential and biexponential functions. *The effects of double pulse/reflection do not affect the signals due to the large timescale.

6.3 Conclusions:

In this chapter, photoinduced absorption techniques were utilised to investigate the excited states of the TADF molecule **DMAC-TRZ** in solution. By performing quasi-CW photoinduced absorption and transient absorption experiments, the transitions and the nature of the electronic excited states involved were identified. The photoinduced absorption signals exhibit a high dependence on the solvent polarity, as expected, with stronger oscillator strength in MCH. Surprisingly, the different solvent polarity does not change the peak positions, implying that the transitions are between upper and lower excited states of the same orbital character, *i.e.* CT to CT in this case. In the Y channel of quasi-CW photoinduced absorption in MCH, a strong and vibronic structured absorption band from ^{3}LE to upper triplet states (^3LE_n) was observed. This transition $^3LE_1 \rightarrow {}^3LE_n$ is quenched by increasing solvent polarity, indicating that the ^{3}CT becomes the lowest triplet state in PhMe and 2MeTHF.

Using ultrafast transient absorption measurements, the nature of the broad photoinduced band observed in the X channel was revealed. Isosbestic points are observed in MCH solution, indicating the presence of two species with overlapping induced absorption, originating from the two stable conformers **DMAC-TRZ**, axial and equatorial conformers previously reported. The QA conformer rapidly decay within 20 ps, indicating a singlet excited state interconversion from the QA to the QE conformer. By increasing the polarity of the solvent, smaller contribution of the QA conformer is expected, thus less pronounced effect of the singlet excited state interconversion between these two stable conformers was observed.

Moreover, a solvent reorganisation induced by the higher polarity of PhMe or rotation of the donor and acceptor about the dihedral bridging C-N band away from orthogonality increases the proportion of LE character in the mixed LE/CT initial state of the transition, evidenced by a significant build-in of the intensity of the PIA band within 17 ps but no changed in the intensity of the SE band. This indicates that the excited state population does not increase so the increase in induced absorption intensity must be due to a change in the oscillator strength of the transition giving rise to the induced absorption band.

Therefore, this chapter has demonstrated that photoinduced absorption measurements can act as a powerful technique for studying TADF molecules. This includes the identification of conformers, which have been shown to be important sources for energy transfer in hyperfluorescence OLED devices.

7 Probing emissive excited states: identifying through-space charge transfer states in TADF molecules

The previous chapters discussed the design of TADF emitter based on a twisted donor-acceptor structure. These molecules rely on electronic communication through-bond via π-conjugation. However, there exists another class of TADF emitters where electronic communication between donor and acceptor moieties is mediated through space. In these through-space charge-transfer (TSCT) architectures, the donor and acceptor groups are disposed in a pseudo-co-facial orientation, connected by a bridging group. This chapter focuses on investigating the interplay between through-bond localized excited (LE) and charge-transfer (CT) states and the TSCT in a rationally designed emitter, **TPA-ace-TRZ**, and cross-compare its photophysical behaviour with a family of model compounds.

The work presented in this chapter has been already published:

i. Kumar, S.; Franca, L. G.; Stavrou, K.; Crovini, E.; Cordes, D. B.; Slawin, A. M. Z.; Monkman, A. P.; Zysman-Colman, E. Investigation of Intramolecular Through-Space Charge-Transfer States in Donor–Acceptor Charge-Transfer Systems. *J. Phys. Chem. Lett.* **2021**, *12* (11), 2820–2830.

7.1 Overview:

A wide variety of TADF emitter have been developed,[25,136] and one alternative approach to achieve TADF is by designing emitter molecules based on through-space charge-transfer (TSCT).[137,138] In contrast to the conventional twisted intramolecular charge transfer TADF emitter design, where D and A moieties are directly attached to each other and the CT transition takes place through-bond, the TSCT-TADF emitter utilizes an electronically benign spacer to separate the D and A moieties.[139] Moreover, the distances between them are maintained in close proximity, facilitating electronic communication, and electron transfer mediated through-space in an analogous manner to exciplexes.[62] By adopting this approach, emitters with small ΔE_{ST} are obtained, and it effectively addresses the challenges related to inhomogeneous D-A dihedral angle within thin films.

This chapter presents a photophysical study of five compounds using acenaphthene as a scaffold, and triphenylamine (TPA) as the donor to investigate TSCT (Figure 7.1). TSCT TADF in **TPA-ace-TRZ** is confirmed by comparison to the family of materials investigated. The structural, electrochemical and photophysical properties of **TPA-ace-TRZ** were investigated and compared with model compounds **TPA-ace-CN, TPA-ace, TPA-ace-Br,** and **2TPA-ace**. From the photophysical studies, changes in local and CT emission character was

observed, as well as delayed fluorescence and phosphorescence emission, even at room temperature. With a focus on CT excited states, a mechanistic approach has been attempted to establish the structure-property relationship in these molecules.

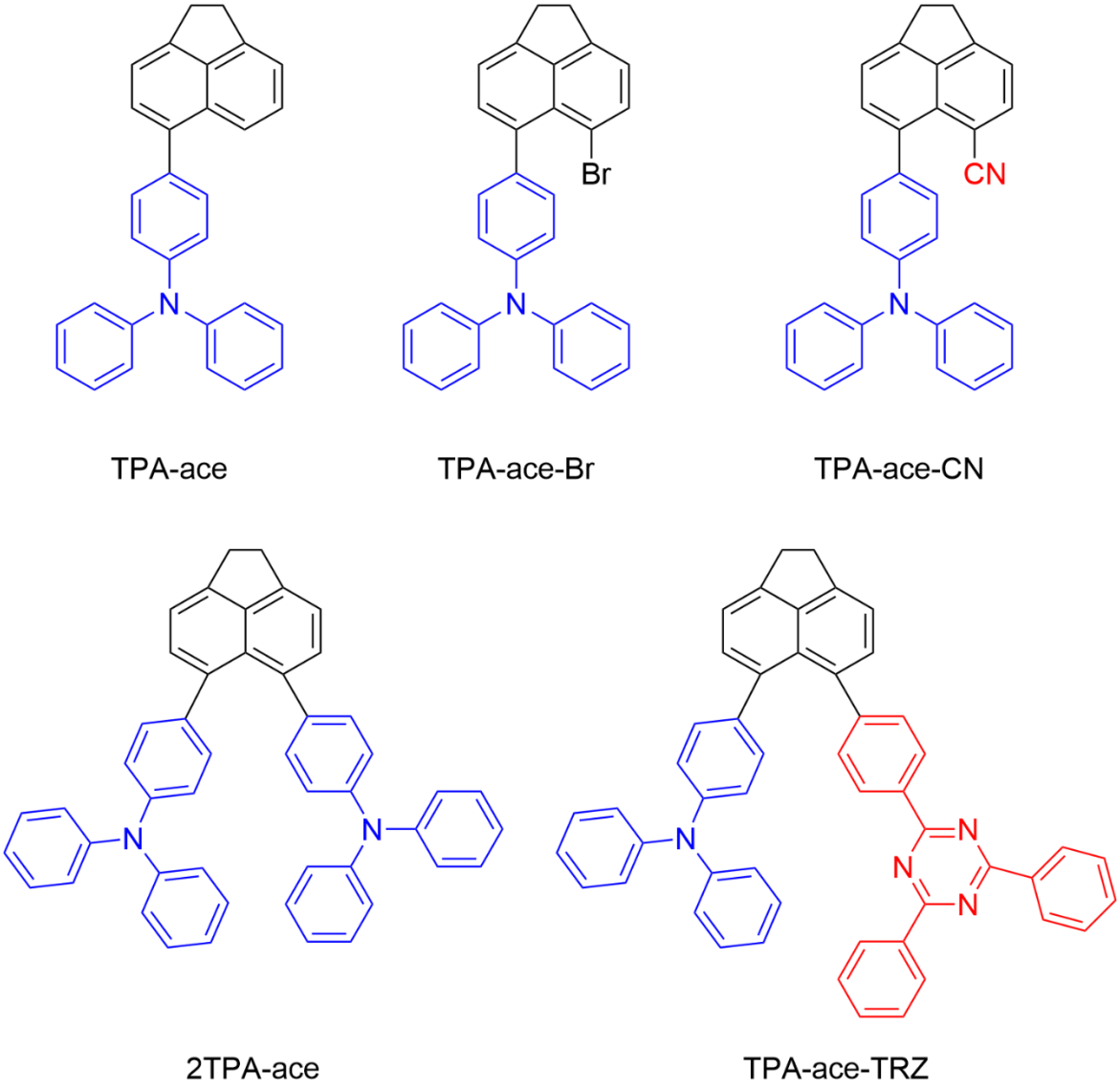

Figure 7.1: Molecular structure of the five compounds studied in this chapter: **TPA-ace**, **TPA-ace-Br**, **TPA-ace-CN**, **2TPA-ace** and **TPA-ace-TRZ**.

7.2 Results and Discussion:

7.2.1 Solution measurements:

To explore the behaviour of those molecules, steady-state photophysical analysis was initially performed in dilute solution. Figure 7.2 shows the normalised optical absorption and emission spectra of **TPA-ace** molecule in three different solvents. The absorption spectrum of **TPA-ace** exhibits two peaks: a band centered around 310 nm related to the acenaphthene scaffold,[62,140] and a second peak, at lower energy, associated to the $\pi \rightarrow \pi^*$ transition of the

delocalised **TPA-ace** system. As the solvent polarity increases, a minor red shift is observed in the latter transition. The photoluminescence (PL) spectra show a weak bathochromic shift and a change from a structured emission band to a Gaussian shape emission band. The small red shift could suggest that the bridge (**ace)** is not neutral and forms a weak through-bond charge transfer (TBCT) state with the donor unit (**TPA)**. This is proposed to be a highly mixed ^{1}LE/^{1}CT state with low CT character as there is conjugation between D and A since they are not orthogonal positioned.

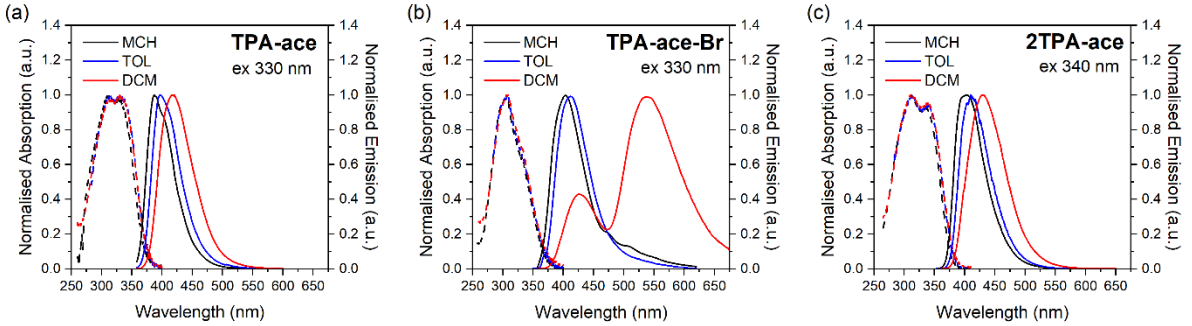

Figure 7.2: Normalized UV–vis absorption (dashed lines) and PL spectra (solid lines) of (a) **TPA-ace**, (b) **TPA-ace-Br** and (c) **2TPA-ace** molecules in different solvents at concentration of 20 µM (λ_{exc} = 330 nm for **TPA-ace** and **TPA-ace-B**r ; λ_{exc} = 340 nm for **2TPA-ace**).

In Figure 7.2b, the absorption feature of the **TPA-ace** fragment in **TPA-ace-Br** is blue shifted, indicating weaker through conjugation between the **TPA** and **ace-Br** units**.** The emission spectra of **TPA-ace-Br** exhibit dual emission in high polar solvent (DCM, dichloromethane). The high energy band red shifts slightly with increasing solvent polarity, matching with the mixed ^{1}LE/^{1}CT TBCT state observed in **TPA-ace**. The second band at around 540 nm observed in DCM is attributed to a state with stronger CT character state (stabilised by the high polarity) in line with the stronger acceptor strength of the **ace-Br** unit. With the addition of a second **TPA** donor unit, **2TPA-ace**, changing from D-B to a D-B-D structure, the absorption and emission spectra are still found to be similar to **TPA-ace** (Figure 7.2c). This similarity in optical behaviour is expected, as the new **TPA** unit does not significantly increase the strength of the donor, and the bridge still acts as very weak acceptor unit, leading to the formation of similar TBCT state. However, careful inspection of the spectra show that the emission onset is red shifted by 102 meV (822 cm^{-1}) in MCH (methylcyclohexane) and the band shape remains structureless. This is identified as the effect of an interaction between the two TPA units, *i.e.* a weak intramolecular dimer state, supported by the X-ray structure presented in the published manuscript.[141] Furthermore, concentration-dependent measurements (Figure 7.3) confirm the presence of a weak intramolecular dimer state hence emission spectra remain unchanged even at very low concentrations (0.06 µM).

These findings fully support the assumption that this interaction between the two weakly overlapping TPA units is a cofacial intramolecular.

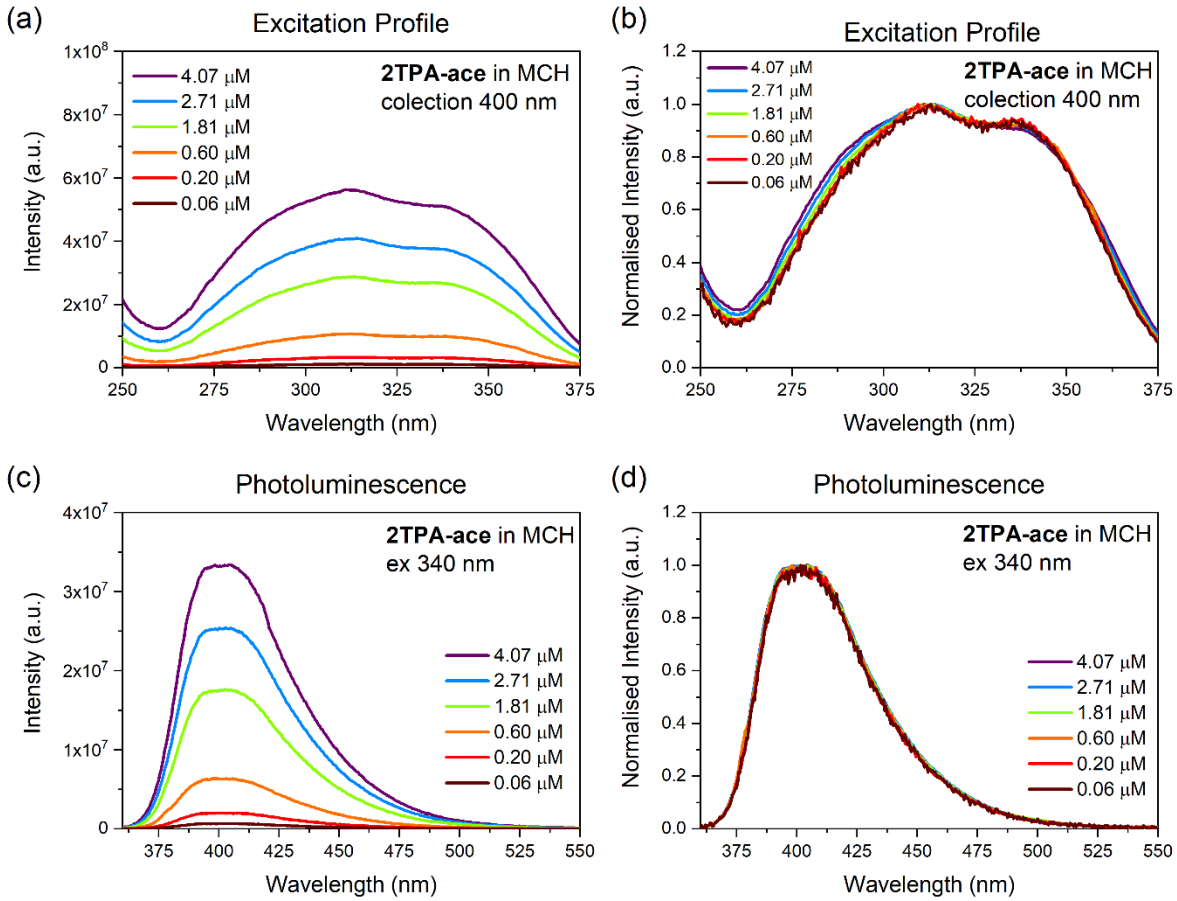

Figure 7.3: Concentration dependence of **2TPA-ace** in MCH (methylcyclohexane) solution. Excitation profile (top panels) and emission spectra (bottom panels) are shown in both non-normalised and normalised spectra.

Similar to the **TPA-ace-Br**, the absorption of the **TPA-ace-CN** (Figure 7.4a) also exhibits a weak lowest-energy transition, ascribed to the delocalised **TPA-ace** unit, but it is much less intense compared to the **TPA-ace** and **2TPA-ace**. In the case of **TPA-ace-TRZ** (Figure 7.4b), the absorption spectra show the presence of the **TRZ** group with the appearance of a strong **TRZ** absorption band at 270 nm.[142] Alongside, like the other compounds, a lower energy band appears at 340 nm, originating from the **TPA-ace** system. Furthermore, unlike the other compounds, a low intensity tail/band from 390 nm to 440 nm is observed in **TPA-ace-TRZ**, which is characteristic of a direct CT transition.[91] This strongly suggests a ground state through-space interaction between the **TRZ** and the **TPZ** units.[62]

With the introduction of stronger acceptor groups, cyano (**CN**) and **TRZ**, a broader emission band is observed even in non-polar solvent as MCH (Figure 7.4a). Additionally, a larger red shift is obtained with increasing solvent polarity, indicating that the presence of the electron accepting **ace-CN** unit contributes to the formation of a stronger CT character excited

state. DFT calculations reveals that this is a through-bond CT state between a stronger D-A pair. **TPA-ace-TRZ** emission spectra (Figure 7.4b) exhibit a red shifted maximum and a significantly stronger positive solvatochromism, suggesting that **TRZ** unit has a much stronger acceptor character than the bridge. This different behaviour strongly implies that this is a TSCT state between the **TRZ** and **TPA** units, with ground state electronic coupling.

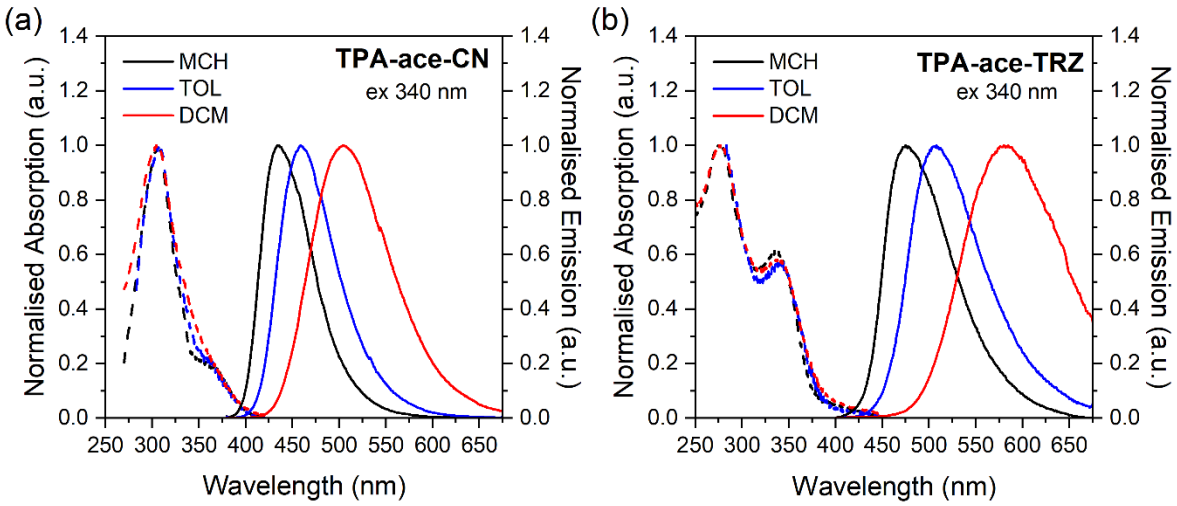

Figure 7.4: Normalised UV–vis absorption (dashed lines) and PL spectra (solid lines) of (a) **TPA-ace-CN** and (b) **TPA-ace-TRZ** molecules in different solvents (λ_{exc} = 340 nm) at concentration of 20 µM.

To investigate the dynamics of the excited states of the five compounds, time-resolved photoluminescence spectra in toluene solution were performed. Figure 7.5a shows the time-resolved normalised emission spectra of the **TPA-ace** in toluene solution at room temperature. In the initial few nanoseconds, an emission band centered at 425 nm is observed, associated with a short-lived LE state on the **TPA** (donor unit) mixed with a small amount of CT character. The local emission decays rapidly, and a broader band at around 500 nm grows, indicating the presence of a weak prompt intramolecular charge transfer (ICT) state. To resolve the ICT band, the spectrum of pure LE contribution was subtracted (first nanoseconds) from the emission spectrum containing a mixed contribution of both LE and CT states (Figure 7.6). This CT state is transient and rapidly decays within 30 ns. This behaviour is characteristic of a twisted intramolecular charge transfer (TICT) state[143] between the **TPA** and **ace** units, where the phenyl ring linking the **TPA** and ace units rotates to near orthogonal position, breaking the conjugation of the two and stabilising the CT state for a short duration.

Similarly, **2TPA-ace** (Figure 7.5c) exhibits a very similar time-resolved spectrum to **TPA-ace**, with a minor enhancement of the CT contribution, potentially due to the weak cofacial intramolecular interaction between the two donor units. All decay curves of these molecules are shown in Figure 7.5f and the lifetimes are obtained by fitting with the

monoexponential or biexponential functions, as shown in Figure 7.7. Both **TPA-ace** and **2TPA-ace** exhibit fast emission decay from the mixed LE/CT state contribution, with τ_{PL} of 1.57 ns and 2.34 ns, respectively, indicating the predominant LE character of this state.

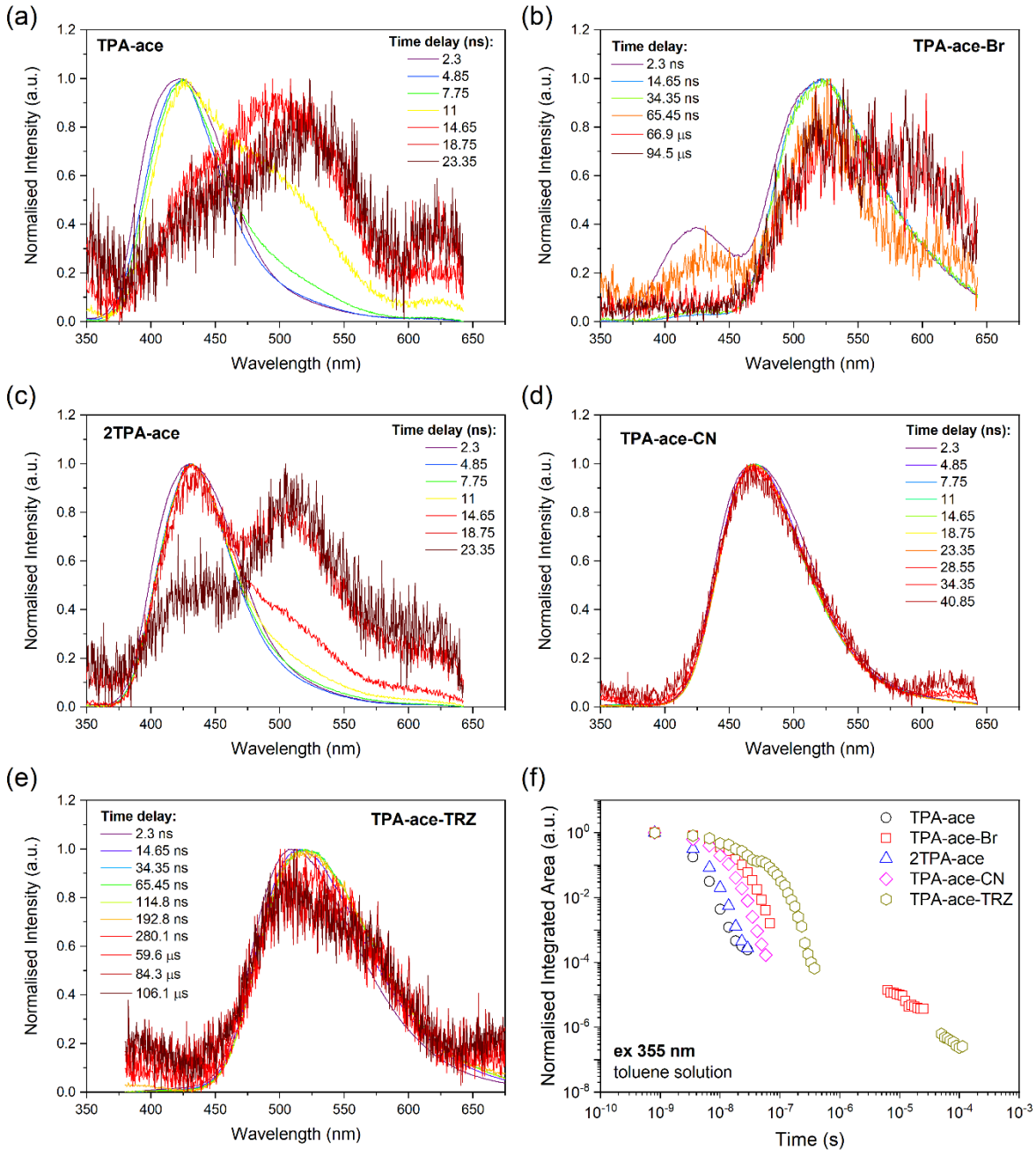

Figure 7.5: Time-resolved normalised PL spectra of (a) **TPA-ace**, (b) **TPA-ace-Br**†, (c) **2TPA-ace**, (d) **TPA-ace-CN** and (e) **TPA-ace-TRZ** in toluene solution at concentration of 20 µM. (f) Time-resolved PL decay curves in the entire region of analysis. λ_{exc} = 355 nm. (†The spectrum recorded at 66 ns is very weak and the feature between 380 nm and 460 nm is the dark signal from the iCCD, not LE emission from the **TPA-ace-Br**).

For **TPA-ace-Br**, at early times, two emission bands are simultaneously observed: an analogous LE/CT emission at 425 nm (only observed in the initial time window) similar to that seen for **TPA-ace** and **2TPA-ace**, as well as a prompt low energy CT emission at 525 nm, with τ_{PL} of 9.4 ns (Table 7.1). The CT band (at 525 nm) in the **TPA-ace-Br** is significantly more

intense than the higher energy band (at 425 nm), and it exhibits a longer lifetime. This indicates that the **ace-Br** is a sufficiently strong acceptor, enabling the formation of a stable and red shifted TBCT.

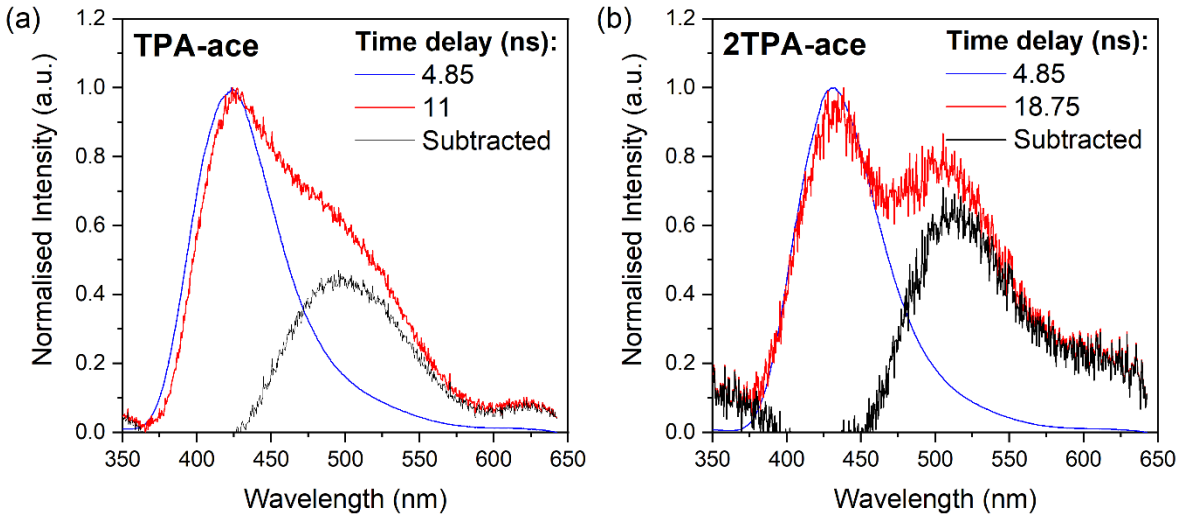

Figure 7.6: Peak of time-resolved spectra of (a) **TPA-ace** and (b) **2TPA-ace** in toluene solution, subtracting their respectively pure LE spectra.

Following an interval without emission (below the noise level of the iCCD), two emission bands were observed: a delayed fluorescence (DF) emission appearing after 50 µs with the same onset energy as the prompt CT band, and a second emission band centered around 590 nm, which is attributed to phosphorescence. As the energy gap between the triplet and singlet state (ΔE_{ST}) is large (approximately 260 meV), rISC would be very weak and slow. Consequently, dual emission coming from TADF and RTP is observed in this case. The dual emission behaviour is due to the heavy atom effect of the **Br**, which enhances ISC leading to a substantial triplet population, which also allowed weak rISC. Again, through the enhanced spin-orbit coupling, the radiative decay of the phosphorescence increases, enabling to simultaneously RTP from the large triplet population.

In the figure 7.5d, the time-resolved PL spectra of **TPA-ace-CN** showed a single emission band over the time, originating from the prompt CT state with lifetime of about 6 ns.

Despite the CT state of **TPA-ace-CN** has higher energy than the transient CT state of **TPA-ace**, the introduction of the **CN** unit led to a stronger and longer-lived CT state with fast electron transfer. As a result, no LE emission was observed within the time resolution. These findings suggest that the CT state in the **TPA-ace-CN** has greater spatial charge separation, resulting in a smaller Coulomb attraction energy and a larger CT state population compared to the transient species in **TPA-ace**.[144]

Figure 7.5e shows the time-resolved PL spectra of **TPA-ace-TRZ**. Initially, an emission

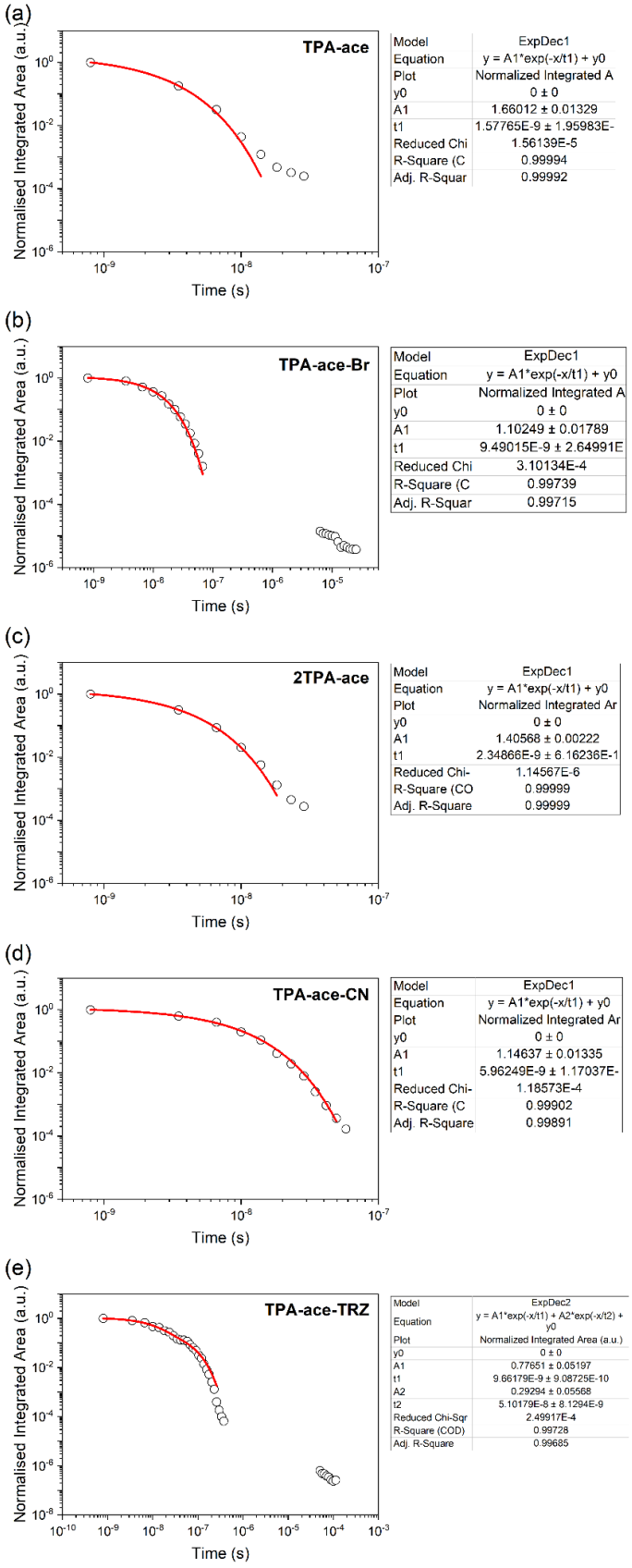

Figure 7.7: Kinetic decays of the five compounds in toluene solution, at 20 µM concentration. (a) **TPA-ace**, (b) **TPA-ace-Br**, (c) **2TPA-ace**, (d) **TPA-ace-CN** and (e) **TPA-ace-TRZ**. All measurements were performed in degassed solutions at room temperature, using a 355 nm excitation source. The data are fitted using either a monoexponetial or a biexponential function.

band around 500 nm is observed, related to the transient CT state as in the **TPA-ace**. By increasing the time delay, a slight red shift is observed, with an isoemissive point at 515 nm. An isoemissive point in the time-resolved PL spectra indicates that the red shift is due two emissive species decaying independently of each other. This observation is supported by the clear biexponential decay from the kinetics curve, with lifetimes (τ_{PL}) of 9.6 ns and 51 ns, indicating emission from two different CT states. An initial through-bond CT state (similar than in **TPA-ace**) decaying rapidly, and a more stable TSCT state, evidencing by the isoemissive point at 515 nm with the change in CT state occurring over 35 ns. At later delay times, a measurable emission is observed over 100 µs, showing the same emission spectrum as the prompt regime attributed to the delayed fluorescence (DF). As these measurements were performed in dilute toluene solution, the DF contribution is unlikely via triplet-triplet annihilation (TTA). As a result, these findings provide experimental evidence for the TADF mechanism originating from the TSCT, observed exclusively in **TPA-ace-TRZ**. Moreover, the weak DF is resulted from a very slow rISC due to the large ΔE_{ST}.

Table 7.1: Photophysical properties of the molecules in toluene solution, at 20 µM concentration.

Emitter	E_g / eV	CT_{abs}		^1CT		Φ_{PL} [c]	τ_{PL} [d] / ns
		/ nm	/ eV	/ nm	/ eV		
TPA-ace	3.29	344	3.60	495[a]	2.50	0.67	1.57
TPA-ace-Br	3.33	324	3.82	522[b]	2.37	0.02	9.49
2TPA-ace	3.26	350	3.54	513[a]	2.41	0.51	2.34
TPA-ace-CN	3.09	352	3.52	470[b]	2.63	0.67	5.96
TPA-ace-TRZ	3.22	348	3.56	518[b]	2.39	0.17	9.6 (72.6%) and 51.0 (27.4%)

[a] Values obtained from peak of the time-resolved PL spectra at around 11 ns delay, subtracting the pure LE spectra (Figure 7.6). [b] Values obtained from peak of the time-resolved spectra at around 14 ns delay, after stabilization of the CT state. [c] Photoluminescence quantum yield in degassed solution at room temperature. (Standard: Quinine Sulfate in 0.1M H_2SO_4, Φ_{PL} = 0.54. [f] Lifetimes associated with the monoexponential or biexponential decay fitting (Figure 7.7).

Table 7.1 summarises the photophysical properties of the five molecules in toluene solution (at 20 µM concentration). Overall, the optical band gaps remained relatively constant at approximately 3.3 eV, except for the **TPA-ace-CN**, which exhibited a slightly smaller gap of 3.09 eV. This difference can be attributed to the influence of the stronger electron-accepting cyano group. Despite **TPA-ace-CN** having strong acceptor character due to the cyano group, it displayed weaker positive solvatochromism compared to **TPA-ace-TRZ**. This outcome can be explained by the larger charge-separation distance in **TPA-ace-CN**, resulting in a smaller

induced dipole moment. Furthermore, **TPA-ace-Br** and **TPA-ace-TRZ** presented smaller Φ_{PL} values, confirming the increased intersystem crossing and triplet population of these materials.

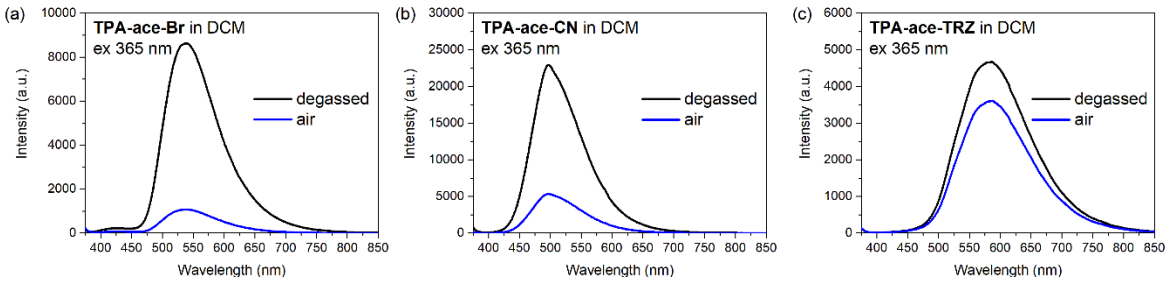

Figure 7.8: Oxygen quenching of total luminescence signal from for (a) **TPA-ace-Br**, (b) **TPA-ace-CN** and (c) **TPA-ace-TRZ** in DCM solution.

To further understand the properties of these materials, the three molecules with higher contribution of CT character excited state were investigated in high-polarity solution (dichloromethane, DCM). For the **TPA-ace-Br**, a small spectral shift of around 20 nm in the low-energy band is observed by increasing the solvent polarity, from toluene to DCM solution (Figure 7.8a). The observed small red shift is lower than expected, raising doubts about the strength of the CT character in this excited state. Comparing with the phosphorescence spectra of this molecule, it is evident that the ΔE_{ST} in DCM exhibit a significant reduction. Figure 7.8 shows the oxygen-dependent emission spectra for **TPA-ace-CN**, **TPA-ace-Br**, and **TPA-ace-TRZ** in DCM. While both **TPA-ace-CN** and **TPA-ace-Br** exhibited significant emission quenching in the presence of oxygen, **TPA-ace-TRZ** displayed much less oxygen sensitivity, which can be attributed to singlet quenching by oxygen in the latter compound. Figure 7.9 presents the kinetic decays and time-resolved emission spectra of the compounds in DCM. All compounds demonstrated only prompt decay in DCM, except for a very minor contribution of delayed emission in **TPA-ace-Br**. **TPA-ace-Br** and **TPA-ace-TRZ** present similar lifetime in DCM and toluene, with the latter having two components, which the longest lifetime is around 40-50 ns. In contrast, **TPA-ace-CN** shows a threefold increase in lifetime in DCM compared to that in toluene. Hence, the oxygen quenching of the **TPA-ace-CN** and **TPZ-ace-Br** does not arise from triplet state (given the absence of significant delayed fluorescence) but rather from an efficient quenching of singlet state in solution, as these excited states have significant long lifetimes.

7.2.2 Solid state measurements:

The solid state photophysical properties of the emitters were studied in drop casting films with a concentration 1 wt % in the zeonex matrix, a low polarity neutral polymer host. Similar to that observed in the solution measurements, **TPA-ace** showed a short lifetime ^{1}LE/^{1}CT

emission at earlier times, which decays rapidly to leave a residual broad ^{1}CT band. The broad ^{1}CT band is centred around 480 nm and it decays within 20 ns (Figure 7.10a). Despite **2TPA-ace** always presenting similar behaviour as **TPA-ace**, the time-resolved spectra (Figure 7.10c) showed the mixed LE/CT emission band, which again decays rapidly to leave a red shifted ^{1}CT band (ca. 15 nm), with higher intensity as compared to **TPA-ace**. The red shift ^{1}CT emission

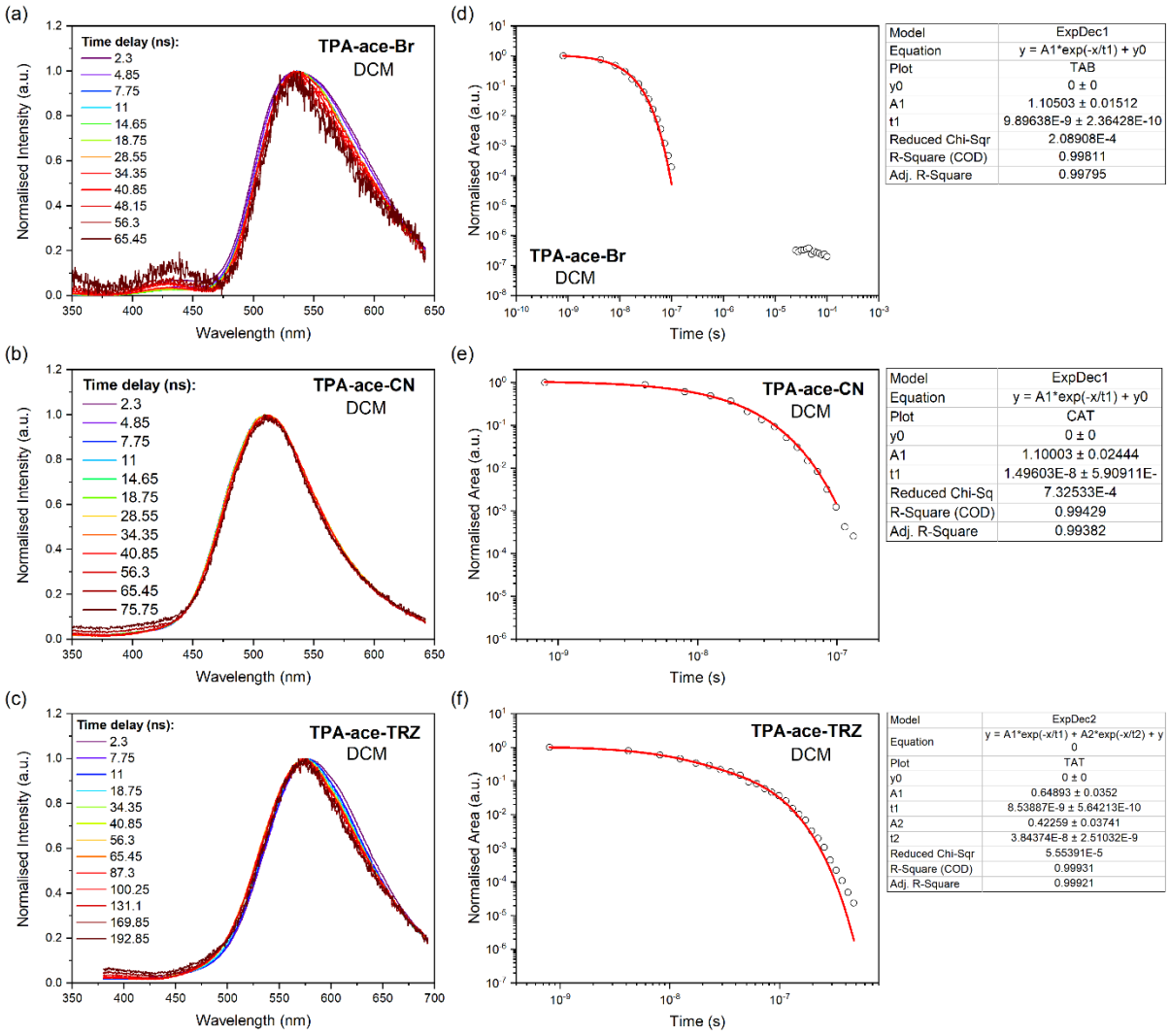

Figure 7.9: Time-resolved normalised PL spectra (left panels) and kinetic decays (right panels) of **TPA-ace-Br** ((a)-(d)), **TPA-ace-CN** ((b)-(e)) and **TPA-ace-TRZ** ((c)-(f)) in DCM solution, at 20 µM concentration.

band supports the view that the interaction between the two **TPA** units enhances the probability of emission from the CT state. In the case of **TPA-ace-CN** (Figure 7.10b), the time-resolved emission spectra show the initial ^{1}CT emission red shifts with increasing time delay, indicating apparent relaxation of ^{1}CT emission due to a distribution of different molecular conformations with different decay times.[91,128] This red shift is a typical behaviour for a TADF molecule where various conformer with different D-A dihedral angle forms CT state with a range of energy values. Phosphorescence spectra (black lines) were measured at long time delays (80 ms), at

80 K, where the onsets of the spectra were used to obtain the ^{3}LE energy of the molecules (Table 7.2). In all cases a large ΔE_{ST} were obtained. The PL kinetic decay curves of the **TPA-ace**, **2TPA-ace** and **TPA-ace-CN** exhibit a rapid decay, giving only prompt emission at room temperature, and no long-lived DF was found, similar to the results in solution.

Figure 7.10d shows the time-resolved PL spectrum of **TPA-ace-Br** in the zeonex matrix, where its behaviour was found to be very similar to that observed in solution. At early times, a very short lived band around 400 nm was observed, while a highly red shifted band at 500 nm emits within 65 ns. In the first time window, a clear dual emission was observed. The low energy band has a pronounced blue edge component and is structured, indicating a mixed LE/CT character. Followed by a pure CT state, which can be also observed within time resolution even at 80 K. After 100 µs, room temperature phosphorescence (RTP) grows in, contrary to solution measurement where mixed DF and phosphorescence emissions are seen at these times. This suggests a greater stabilisation of the CT state in toluene through the solvatochromic stabilisation effect. Figure 7.10e shows the time-resolved PL spectra of **TPA-ace-TRZ**. Initially, during the prompt fluorescence regime, there is an observable relaxation of the ^{1}CT band, which decays within few hundred nanoseconds. The onset of the CT emission is blue-shifted by 20 meV in zeonex when compared to toluene solution results (Figure 7.5). Additionally, a consistent isoemissive point at 505 nm is observed, see Figure 7.11. This suggests that the CT emission observed in zeonex primarily originates from the through-bond state, while the formation of the (lower energy) TSCT state is hindered by the host matrix. As a consequence, this implies that reorganisation of the **TPA** and **TRZ** moieties of the **TPA-ace-TRZ** is necessary to enable access to the TSCT state, which is hindered in zeonex. At later times, a very weak emission appears with similar energy onset as the phosphorescence (observed at late delayed times and at 80 K). This emission indicates inefficient room temperature phosphorescence (RTP) and not DF.

Two different regimes were observed in the decay curves of **TPA-ace-Br** and T**PA-ace-TRZ** (Figure 7.10f), assigned to prompt ^{1}CT emission and a delayed emission component. While the delayed emission component of **TPA-ace-TRZ** is only observable at very late times (around 10 ms) and has a very weak contribution ascribed to phosphorescence, the **TPA-ace-Br** exhibits a strong RTP contribution. This confirms that attaching a heavy atom such as Br into the molecule significantly enhances intersystem crossing (ISC) within this system.

Table 7.2 summarises the photophysical data of the 1 wt% zeonex films. The onset energies of the S_1 and T_1 states were determined through time-resolved spectra at room temperature (S_1) and low temperature (80 K) (T_1), respectively. The ^{3}LE values of all molecules

are slightly different but within error around 2.53 eV for **TPA-ace**, **TPA-ace-TPA** and **TPA-ace-Br**. This suggests that the structural modifications have minimal influence on the energy and location of the local triplet state.

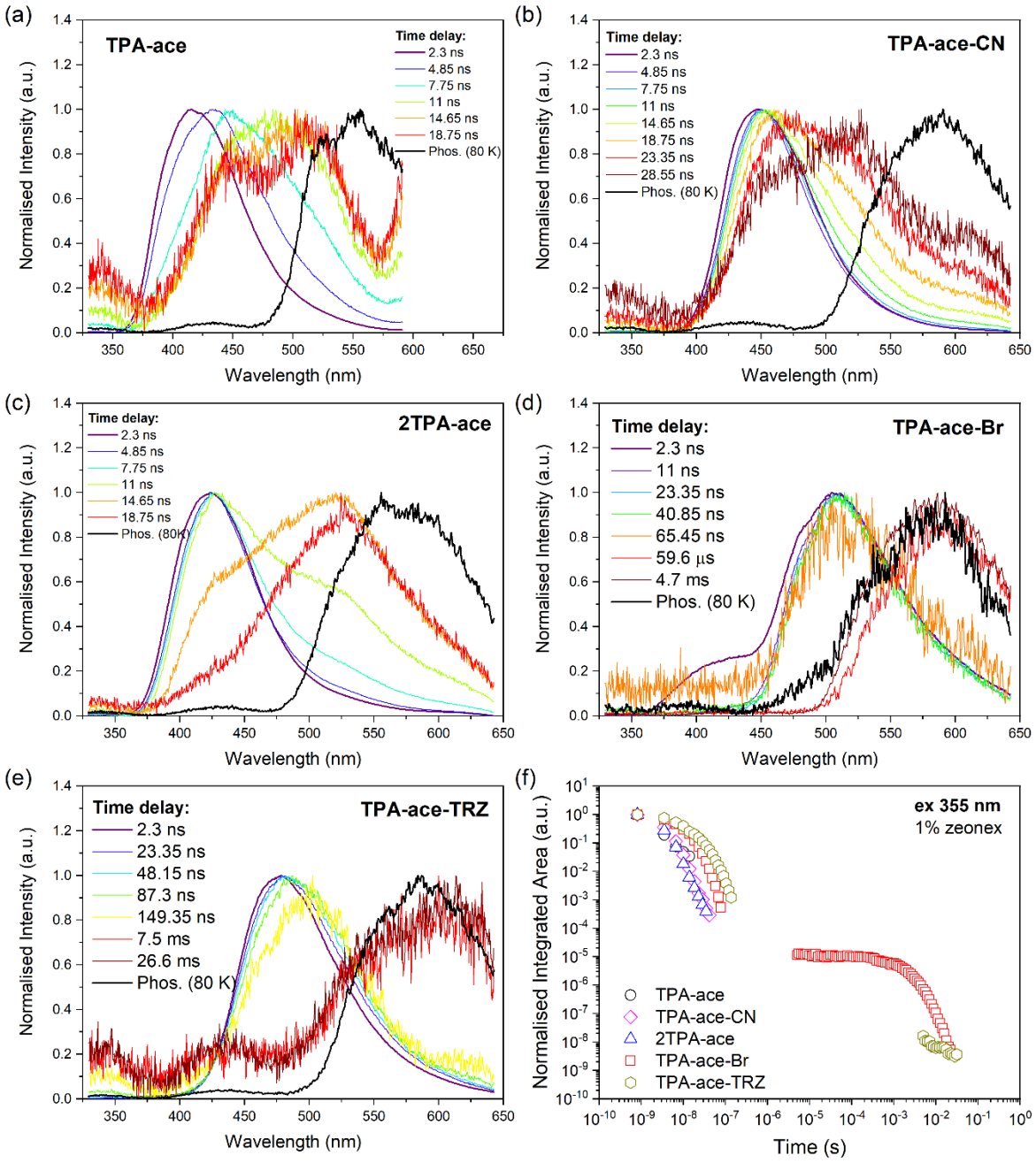

Figure 7.10: Time-resolved normalised PL spectra of (a) **TPA-ace**, (b) **TPA-ace-CN**, (c) **2TPA-ace**, (d) **TPA-ace-Br** and (e) **TPA-ace-TRZ** in 1 wt% zeonex films. (f) Time-resolved PL decay curves in the entire region of analysis. λ_{exc} = 355 nm.

However, **TPA-ace-CN** and **TPA-ace-TRZ** exhibit a lower triplet energy value by approximately 5-10 meV. At 80 K, **TPA-ace** and **2TPA-ace** demonstrate structured phosphorescence attributed to the lowest energy ^{3}LE state of the **ace** unit.[145] Nonetheless, when the acenaphthene is further substituted, the structured feature disappears. This is consistent with the large heavy atom effects observed in **TPA-ace-Br**, which enhances the **ace**

phosphorescence. The ΔE_{ST} values are higher than 0.4 eV in all cases except for **TPA-ace-Br**, where the value is 0.26 eV. Consequently, it is not surprising that little or no DF is found in these compounds apart from **TPA-ace-Br** where it is weak. The Φ_{PL} values in films, measured under a N_2 atmosphere, are higher for **TPA-ace** and **2TPA-ace** than the other compounds, which have emission mainly coming from a mixed ^{1}LE/^{1}CT state. For the molecules displaying more pronounced CT characteristics, such as **TPA-ace-CN** and **TPA-ace-TRZ**, the Φ_{PL} is significantly lower. This indicates that the more stable CT states result in higher ^{3}CT triplet state formation, which cannot be harvested by rISC.

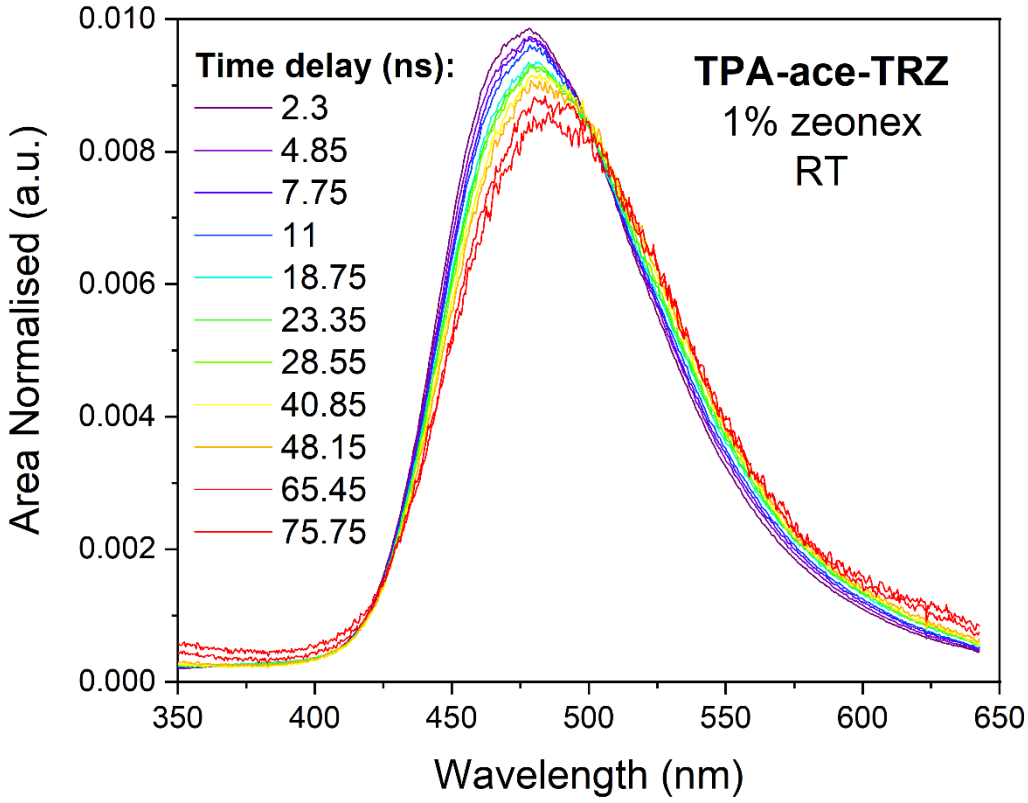

Figure 7.11: Area normalised emission spectra of **TPA-ace-TRZ** in 1 wt% zeonex film at room temperature.

The transient PL decay curves were fitted by single or double exponentials. The rapid decay of the emission of **TPA-ace** restricted accurate estimation of the prompt lifetime. **2TPA-ace** presented two different lifetimes: a faster one with larger contribution of around 2 ns arising from the mixed LE/CT state, and a slower, smaller contribution with lifetime around 4 ns, originating from the CT state. The prompt emission observed in **TPA-ace-CN** also has two components ascribed to the mixed LE/CT state and the relaxed ^{1}CT. **TPA-ace-TRZ** has two distinct characteristic lifetimes: one corresponding to the fast decaying through-bond CT state, and the other long lived TSCT state. In contrast, **TPA-ace-Br** exhibited a single CT state

lifetime in the prompt regime, while in the delayed regime, two exponential lifetimes on the order of milliseconds, and assigned to RTP.

Table 7.2: Photophysical properties of the five molecules in drop casting films with a concentration of 1 wt% in the zeonex matrix.

Emitter	^{1}CT[a] / eV	^{3}LE[b] / eV	ΔE_{ST}[c] / eV	Φ_{PL}[d]	τ_p[e] / ns	τ_d[e] / ns
TPA-ace	2.99	2.53	0.46	0.37	-	-
TPA-ace-Br	2.77	2.51	0.26	-	8.05	0.33 (90.6%) 2.05 (9.4%)
2TPA-ace	2.95	2.55	0.40	0.36	1.93 (92.1%) 4.39 (7.9%)	-
TPA-ace-CN	2.99	2.47	0.52	0.20	2.55 (97.0%) 7.50 (3.0%)	-
TPA-ace-TRZ	2.94	2.46	0.48	0.12	6.9 (73.0%) 2.05 (27.0%)	-

[a] Values estimated from the onset of time-resolved PL spectra after stabilisation of ^{1}CT or deconvoluted in order to obtain only ^{1}CT onset. [b] Values estimated from the onset of phosphorescence spectra, spectra were collected with 80 ms time delay and measured at 80 K. [c] $\Delta E_{ST} = {}^1$CT - ^{3}LE. [d] Φ_{PL} measured for spin-coated films with concentration of 1 wt% in zeonex matrix using an integrated sphere connected to a Fluorolog-3. [e] Lifetimes estimated from monoexponential or biexponential decay fitting of the prompt and delayed regimes (Figure 7.12).

Time-resolved PL decays were also performed on the zeonex films at 80 K (Figure 7.13). For **TPA-ace**, **2TPA-ace** and **TPA-ace-CN**, similar to the behaviour at room temperature, the rapid decay of the mixed ^{1}LE/^{1}CT state at 490 nm was observed, leaving a transient CT state at 520 nm which decays within 100 ns. In particular, **TPA-ace-CN** presented a weak, shorter lifetime prompt CT state emission at 80 K, compared to the data at room temperature. This indicates that a twisting motion is necessary, also possible in the zeonex polymer, to stabilise the CT state in **TPA-ace-CN**, where the steric hindrance caused by the **CN** group is thermally activated. Phosphorescence was observed in the ms time range. The CT emission from **TPA-ace-Br** at 80 K was found to be highly structured with the same onset energy as at RT. This surprising observation suggests that this low energy (weakly) CT state is of mixed LE/CT character with high LE contribution at 80 K.[146] Finally, similar to the observed RT behaviour, **TPA-ace-TRZ** showed initial CT emission, changing to a second low energy CT state around 10 ns. An isoemissive point was observed, but the processes occur over a slower time scale, *ca.* 200 ns. This is an indicative of a conformational reorganisation of the **TPA** and **TRZ** moieties to stabilise the TSCT state. In all cases, well-resolved phosphorescence is observed at long times from which accurate ^{3}LE energies are calculated.

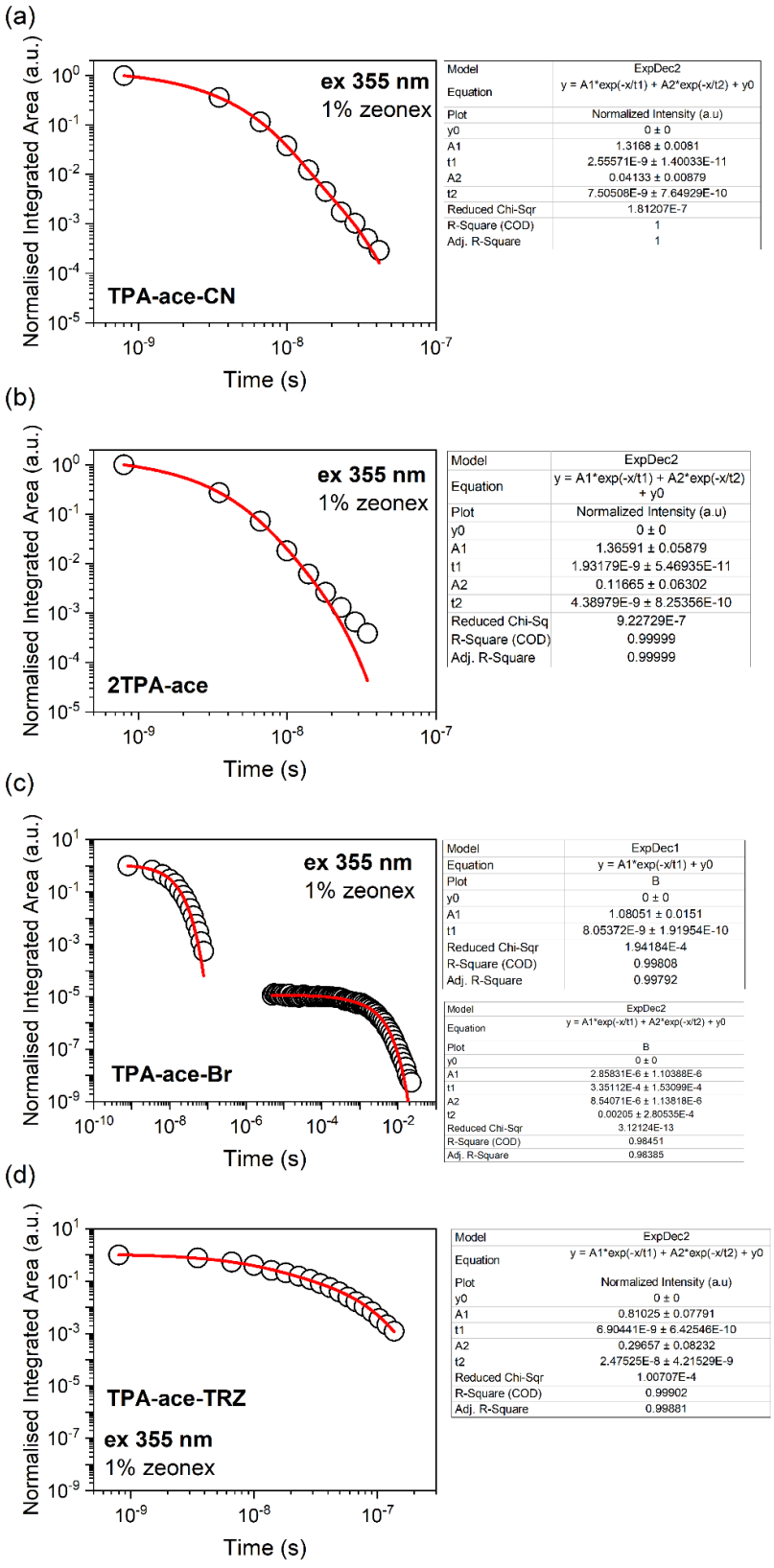

Figure 7.12: Kinetic decays of the compounds doped in 1 wt% zeonex films. (a) **TPA-ace-CN**, (b) **2TPA-ace**, (c) **TPA-ace-Br** and (d) **TPA-ace-TRZ**. All measurements were performed under vacuum atmosphere, using a 355 nm excitation source. The data are fitted using either a monoexponetial or a biexponential function.

To elucidate the reasons behind the little or absent TADF from the TSCT state in **TPA-ace-TRZ**, even in DCM where the ΔE_{ST} becomes relatively small, the lowest energy triplet state of the molecule needs to be considered. As previously mentioned, the local triplet state is found to be localised in the **ace** bridge (thus a **Br** attached to the ace gives a heavy atom enhancement to the ace phosphorescence). However, in **TPA-ace-TRZ**, the **ace** unit is orthogonal and electronically decoupled from D and A, especially in the TSCT conformation. Consequently, in this conformation ^{1}CT and ^{3}CT become degenerate[147] and triplet harvesting must occur through the vibronic-coupling spin-orbit coupling (SOC) mechanism,[78,80] similar to D-A and exciplex TADF systems.[110] Nevertheless, the potentially mediating isoenergetic local triplet state in **TPA-ace-TRZ** is the **ace** bridge triplet, which is orthogonal to both D and A and thus cannot efficiently couple to the TSCT states. Therefore, despite the strong TSCT observed in **TPA-ace-TRZ**, it cannot produce TADF because of the lack of coupling to a mediating triplet state. This reveals that TSCT D-A pairs, similar to through bond D-A systems and exciplex molecules, give rise to TADF via the vibronic coupling SOC mechanism.[148]

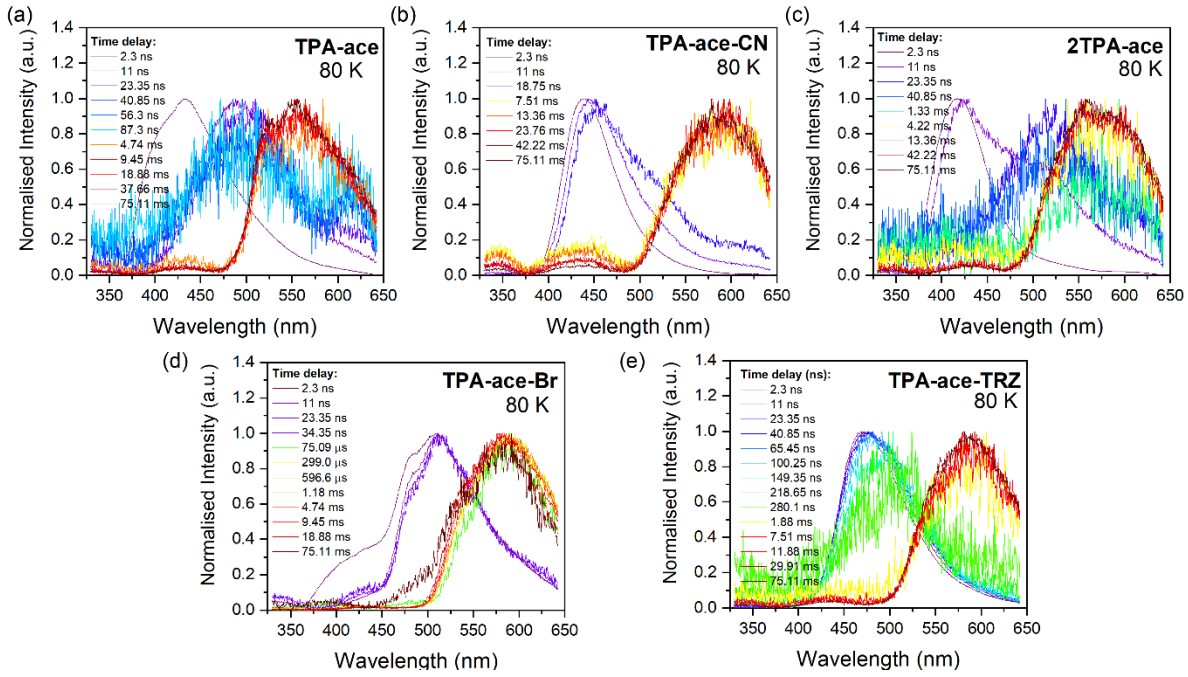

Figure 7.13: Time-resolved normalised PL spectra of (a) **TPA-ace**, (b) **TPA-ace-CN**, (c) **2TPA-ace**, (d) **TPA-ace-Br** and (e) **TPA-ace-TRZ** in 1 wt% zeonex films. Measurements performed at 80 K. λ_{exc} = 355 nm.

7.3 Conclusions:

To summarise, this chapter illustrates the use of optical spectroscopy to demonstrate that the compound **TPA-ace-TRZ** emits via a TSCT state. A comparative analysis of the photophysical properties of this compound is performed alongside several model systems: **TPA-ace**, **TPA-ace-Br**, **2TPA-ace**, and **TPA-ace-CN**. In all five compounds, there is an

emissive mixed through-bond LE/CT state, with varying levels of LE and CT mixing. Notable, **TPA-ace** displays the highest degree of LE character while **TPA-ace-TRZ** exhibits the strongest CT character. Time-resolved measurement showed that the introduction of a second **TPA** donor onto the ace unit in **2TPA-ace** leads to an intramolecular dimer formation causing a relative enhancement to the oval ICT contribution. Conversely, the addition of the electron-accepting **CN** unit in **TPA-ace-CN** resulted in a pure blue ICT emission. **TPA-ace-Br** also was shown a strong ICT state in the prompt region, due to the nearly orthogonal conformation between the **TPA** and the **ace-Br** groups in the ground state. However, thanks to the relatively large ΔE_{ST} and the presence of the heavy bromine atom, a dual TADF/RTP emission appeared weakly in solution, and predominantly RTP character in solid state. The TSCT state, uniquely observed in **TPA-ace-TRZ**, exhibited a minor delayed contribution in toluene solution, attributed to a large ΔE_{ST} of around 200 meV. Therefore, this study provides one of the few clear experimental demonstrations of the existence of a TSCT state through optical spectroscopy, and also reveals the intimate interplay that the bridging **ace** group has in mediating both the through-bond ICT state and the TSCT state. Through this work, a mechanistic approach has been attempted to establish the structure-property relationship in these TADF molecules based on TSCT states, providing insights into the designing of new TADF emitter molecules for OLED applications.

8 General Conclusions

Throughout the course of this thesis, various advanced optical spectroscopy techniques were employed to gain a better understanding of highly-efficient emitter molecules. These molecules exhibit very complex photophysics properties, which were uncovered through the use of these techniques. Environmental, conformational and design aspects of TADF molecules were also studied.

The first study highlighted the main effects of using a rigid spiro bridging and how this bridging structure strongly affected the TADF properties by effectively decoupling the D and A units. Broadly speaking, the results showed that through this critical decoupling of the D and A units, facilitated by the spiro-centre, Kasha's rule remained applicable to each subunit locally. However, this rule can be disregarded when considering the photophysics of the entire molecule.

The subsequent study focused on the environment impact on TADF mechanism. This work showed that the orthogonal and fixed structure of the spiro compounds prevent the distribution of the rISC. This phenomenon is evident in C-N linked TADF molecules, but as shown here, not in spiro TADF, confirming that the variation of D-A dihedral angle causes the rISC rate dispersion. On the other hand, the configuration of energy levels was notably affected by the host molecules. This influence had a significant impact on both vibronic and SOC coupling, resulting in distinct decay channels that governed the rISC rates.

Pump-probe techniques were also employed to investigate the dark excited states of the TADF molecules. By combining these techniques with photoluminescence spectroscopy, it was possible to identify the assignment and nature characteristics of the electronic excited state transitions. Additionally, the impact on the TADF mechanism on the oscillator strength and reorganization of the electronic excited states, especially on the triplet excited states, was determined by changing the solvent polarity.

To extend this knowledge, these advanced optical spectroscopy measurements were used to identify an alternative design of TADF molecules, known as through-space TADF molecules. A comparative analysis of the photophysical properties, conducted alongside model systems, allowed for a clear experimental demonstration of the TSCT state and the role of the bridge in mediating the CT state formation.

Therefore, this research has achieved a better understanding of the emission mechanism in these molecules, providing valuable information for the establishment of new design rules and the identification of crucial parameters for the TADF mechanism.

9 References

(1) Hong, G.; Gan, X.; Leonhardt, C.; Zhang, Z.; Seibert, J.; Busch, J. M.; Bräse, S. A Brief History of OLEDs—Emitter Development and Industry Milestones. *Adv. Mater.* **2021**, *33* (9), 2005630. https://doi.org/10.1002/adma.202005630.

(2) Geffroy, B.; le Roy, P.; Prat, C. Organic Light-Emitting Diode (OLED) Technology: Materials, Devices and Display Technologies. *Polym. Int.* **2006**, *55* (6), 572–582. https://doi.org/10.1002/pi.1974.

(3) Coffey, V. C. The Age of OLED Displays. *Opt. Photonics News* **2017**, No. November, 34–41.

(4) Corrêa Santos, D.; Vieira Marques, M. de F. Blue Light Polymeric Emitters for the Development of OLED Devices. *J. Mater. Sci. Mater. Electron.* **2022**, *33* (16), 12529–12565. https://doi.org/10.1007/s10854-022-08333-3.

(5) Pei, K. Recent Advances in Molecular Doping of Organic Semiconductors. *Surfaces and Interfaces* **2022**, *30* (February), 101887. https://doi.org/10.1016/j.surfin.2022.101887.

(6) Liu, Y. F.; Feng, J.; Bi, Y. G.; Yin, D.; Sun, H. B. Recent Developments in Flexible Organic Light-Emitting Devices. *Adv. Mater. Technol.* **2019**, *4* (1), 1–19. https://doi.org/10.1002/admt.201800371.

(7) Commercial production of large format flexible displays coming soon? https://www.inavateonthenet.net/features/article/commercial-production-of-large-format-flexible-displays-coming-soon.

(8) Transparent OLED Signage https://www.lg.com/uk/business/transparent-oled-signage.

(9) Galaxy Z Fold4 https://www.samsung.com/uk/smartphones/galaxy-z-fold4/.

(10) Samsung researchers demonstrate a “commercializable” stretchable OLED display https://www.oled-info.com/samsung-researchers-demonstrate-commercializable-stretchable-oled-display.

(11) Devices, O. L. *Organic Light-Emitting Devices*; 2004. https://doi.org/10.1007/978-0-387-21720-8.

(12) Méhes, G.; Goushi, K.; Potscavage, W. J.; Adachi, C. Influence of Host Matrix on Thermally-Activated Delayed Fluorescence: Effects on Emission Lifetime, Photoluminescence Quantum Yield, and Device Performance. *Org. Electron.* **2014**, *15* (9), 2027–2037. https://doi.org/10.1016/j.orgel.2014.05.027.

(13) Albrecht, K.; Matsuoka, K.; Fujita, K.; Yamamoto, K. Carbazole Dendrimers as Solution-Processable Thermally Activated Delayed-Fluorescence Materials ** Angewandte. **2015**, 1–7. https://doi.org/10.1002/anie.201500203.

(14) Kawamura, Y.; Brooks, J.; Brown, J. J.; Sasabe, H.; Adachi, C. Intermolecular Interaction and a Concentration-Quenching Mechanism of Phosphorescent Ir(III) Complexes in a Solid Film. *Phys. Rev. Lett.* **2006**, *96* (1), 11–14. https://doi.org/10.1103/PhysRevLett.96.017404.

(15) Jung, Y. K.; Choi, H. S.; Ahn, S. Y.; Kim, S.; Choi, H.; Han, C. W.; Kim, B.; Kim, S. J.; Kim, J.; Choi, J. H.; Yoon, S.; Tak, Y. H.; Choi, H. C.; Ahn, B. C.; Kang, I. B. 52-3: Distinguished Paper : 3 Stacked Top Emitting White OLED for High Resolution OLED TV. *SID Symp. Dig. Tech. Pap.* **2016**, *47* (1), 707–710. https://doi.org/10.1002/sdtp.10781.

(16) Choi, H.-S.; Kim, T.-S.; Han, C.-W.; Choi, H.-C.; Ahn, B.-C.; Kang, I.-B.; Oh, C.-H.; Yeo, S.-D. 45-1:

Invited Paper : Recent Progress of White Light-Emitting Diodes for an Application to New Models of OLED TV. *SID Symp. Dig. Tech. Pap.* **2016**, *47* (1), 605–608. https://doi.org/10.1002/sdtp.10756.

(17) Baldo, M. A.; O'Brien, D. F.; Thompson, M. E.; Forrest, S. R. Excitonic Singlet-Triplet Ratio in a Semiconducting Organic Thin Film. *Phys. Rev. B* **1999**, *60* (20), 14422–14428. https://doi.org/10.1103/PhysRevB.60.14422.

(18) Wilson, J. S.; Dhoot, A. S.; Seeley, A. J. A. B.; Khan, M. S.; Köhler, A.; Friend, R. H. Spin-Dependent Exciton Formation in π-Conjugated Compounds. *Nature* **2001**, *413* (6858), 828–831. https://doi.org/10.1038/35101565.

(19) *Highly Efficient OLEDs with Phosphorescent Materials*; Yersin, H., Ed.; Wiley, 2007. https://doi.org/10.1002/9783527621309.

(20) Pander, P.; Bulmer, R.; Martinscroft, R.; Thompson, S.; Lewis, F. W.; Penfold, T. J.; Dias, F. B.; Kozhevnikov, V. N. 1,2,4-Triazines in the Synthesis of Bipyridine Bisphenolate ONNO Ligands and Their Highly Luminescent Tetradentate Pt(II) Complexes for Solution-Processable OLEDs. *Inorg. Chem.* **2018**, *57* (7), 3825–3832. https://doi.org/10.1021/acs.inorgchem.7b03175.

(21) Chang, C.-F.; Cheng, Y.-M.; Chi, Y.; Chiu, Y.-C.; Lin, C.-C.; Lee, G.-H.; Chou, P.-T.; Chen, C.-C.; Chang, C.-H.; Wu, C.-C. Highly Efficient Blue-Emitting Iridium(III) Carbene Complexes and Phosphorescent OLEDs. *Angew. Chemie Int. Ed.* **2008**, *47* (24), 4542–4545. https://doi.org/10.1002/anie.200800748.

(22) Baldo, M. A.; O'Brien, D. F.; You, Y.; Shoustikov, A.; Sibley, S.; Thompson, M. E.; Forrest, S. R. Highly Efficient Phosphorescent Emission from Organic Electroluminescent Devices. *Nature* **1998**, *395* (6698), 151–154. https://doi.org/10.1038/25954.

(23) Volz, D.; Wallesch, M.; Fléchon, C.; Danz, M.; Verma, A.; Navarro, J. M.; Zink, D. M.; Bräse, S.; Baumann, T. From Iridium and Platinum to Copper and Carbon: New Avenues for More Sustainability in Organic Light-Emitting Diodes. *Green Chem.* **2015**, *17* (4), 1988–2011. https://doi.org/10.1039/C4GC02195A.

(24) Schmidbauer, S.; Hohenleutner, A.; König, B. Chemical Degradation in Organic Light-Emitting Devices: Mechanisms and Implications for the Design of New Materials. *Adv. Mater.* **2013**, *25* (15), 2114–2129. https://doi.org/10.1002/adma.201205022.

(25) Wong, M. Y.; Zysman-Colman, E. Purely Organic Thermally Activated Delayed Fluorescence Materials for Organic Light-Emitting Diodes. *Adv. Mater.* **2017**, *29* (22), 1605444. https://doi.org/10.1002/adma.201605444.

(26) Dias, F. B.; Bourdakos, K. N.; Jankus, V.; Moss, K. C.; Kamtekar, K. T.; Bhalla, V.; Santos, J.; Bryce, M. R.; Monkman, A. P. Triplet Harvesting with 100% Efficiency by Way of Thermally Activated Delayed Fluorescence in Charge Transfer OLED Emitters. *Adv. Mater.* **2013**, *25* (27), 3707–3714. https://doi.org/10.1002/adma.201300753.

(27) Qin, T.; Liu, B.; Zhu, K.; Luo, Z.; Huang, Y.; Pan, C.; Wang, L. Organic Fluorescent Thermometers: Highlights from 2013 to 2017. *TrAC Trends Anal. Chem.* **2018**, *102*, 259–271. https://doi.org/10.1016/j.trac.2018.03.003.

(28) McMurry, J. *Organic Chemistry*, Ninth edit.; Boston, MA : Cengage Learning, 2016.

(29) Razeghi, M. The Carbon Atom. In *The Mystery of Carbon*; IOP Publishing, 2019; pp 1-1-1–12. https://doi.org/10.1088/2053-2563/ab35d1ch1.

(30) Köhler, A.; Bässler, H. *Electronic Processes in Organic Semiconductors: An Introduction*; Wiley:

Weinheim, Germany, 2015. https://doi.org/10.1002/9783527685172.

(31) I. L. Finar. *Organic Chemistry Volume 01: The Fundamental Principles*; Longmans, 1963.

(32) Lamoureux, G.; Ogilvie, J. F. A Critical History of Hybrid Atomic Orbitals and Hybridization. *SSRN Electron. J.* **2022**, *4* (2), 1932–1950. https://doi.org/10.2139/ssrn.4288679.

(33) Atkins, P. 1Matter from the Inside. *Physical Chemistry: A Very Short Introduction*. Oxford University Press April 24, 2014, p 0. https://doi.org/10.1093/actrade/9780199689095.003.0001.

(34) Graham Patrick. *BIOS Instant Notes in Organic Chemistry*; CRC Press LLC, 2004.

(35) Brütting, W. *Physics of Organic Semiconductors*; Brütting, W., Ed.; Wiley, 2005. https://doi.org/10.1002/3527606637.

(36) Yadav, R. A. K.; Dubey, D. K.; Chen, S.-Z.; Liang, T.-W.; Jou, J.-H. Role of Molecular Orbital Energy Levels in OLED Performance. *Sci. Rep.* **2020**, *10* (1), 9915. https://doi.org/10.1038/s41598-020-66946-2.

(37) Valeur, B. .; Berberan-Santos, M. N. . *Molecular Fluorescence Principles and Applications*, 2nd ed.; Weinheim : Wiley-VCH, 2013.

(38) Bertolucci; C, D.; Harris; D, M. *Symmetry Spectroscopy*; 1989.

(39) DOS-SANTOS, PALOMA, L. The Study of Thermally Activated Delayed Fluorescence Mechanism in Mono and Bimolecular Systems, Durham University, 2018.

(40) Pauli, W. Exclusion Principle and Quantum Mechanics: Nobel Lecture, December 13, 1946. *Nobel Lect. Phys. 1942-1961* **1994**, No. 8, 27–43.

(41) Wang, Z.; Dai, Y.; Ding, L.; Dong, B.; Jiang, S.; Wang, J.; Pei, J. A Stable Triplet-Ground-State Conjugated Diradical Based on a Diindenopyrazine Skeleton. *Angew. Chemie Int. Ed.* **2021**, *60* (9), 4594–4598. https://doi.org/10.1002/anie.202012989.

(42) Turro, N. J. .; Ramamurthy, V. .; Scaiano, J. C. (Juan C. . *Principles of Molecular Photochemistry : An Introduction*; Sausalito, Calif. : University Science Books, 2009.

(43) Dias, F. B.; Penfold, T. J.; Monkman, A. P. Photophysics of Thermally Activated Delayed Fluorescence Molecules. *Methods Appl. Fluoresc.* **2017**, *5* (1), 012001. https://doi.org/10.1088/2050-6120/aa537e.

(44) Tao, Y.; Yuan, K.; Chen, T.; Xu, P.; Li, H.; Chen, R.; Zheng, C.; Zhang, L.; Huang, W. Thermally Activated Delayed Fluorescence Materials Towards the Breakthrough of Organoelectronics. *Adv. Mater.* **2014**, *26* (47), 7931–7958. https://doi.org/10.1002/adma.201402532.

(45) Joseph R. Lakowicz. *Principles of Fluorescence Spectroscopy*; Springer, 1999.

(46) Franck, J.; Dymond, E. G. Elementary Processes of Photochemical Reactions. *Trans. Faraday Soc.* **1926**, *21* (February), 536. https://doi.org/10.1039/tf9262100536.

(47) Condon, E. A Theory of Intensity Distribution in Band Systems. *Phys. Rev.* **1926**, *28* (6), 1182–1201. https://doi.org/10.1103/PhysRev.28.1182.

(48) Schwartz, S. E. The Franck-Condon Principle and the Duration of Electronic Transitions. *J. Chem. Educ.* **1973**, *50* (9), 608. https://doi.org/10.1021/ed050p608.

(49) Viswanath, G.; Kasha, M. Confirmation of the Anomalous Fluorescence of Azulene. *J. Chem. Phys.* **1956**, *24* (3), 574–577. https://doi.org/10.1063/1.1742548.

(50) Halls, M. D.; Schlegel, H. B. Molecular Orbital Study of the First Excited State of the OLED Material Tris(8-Hydroxyquinoline)Aluminum(III). *Chem. Mater.* **2001**, *13* (8), 2632–2640. https://doi.org/10.1021/cm010121d.

(51) Jaffe, H. H.; Miller, A. L. The Fates of Electronic Excitation Energy. *J. Chem. Educ.* **1966**, *43* (9), 469. https://doi.org/10.1021/ed043p469.

(52) Baldo, M. A.; Lamansky, S.; Burrows, P. E.; Thompson, M. E.; Forrest, S. R. Very High-Efficiency Green Organic Light-Emitting Devices Based on Electrophosphorescence. *Appl. Phys. Lett.* **1999**, *75* (1), 4–6. https://doi.org/10.1063/1.124258.

(53) Kasha, M. Characterization of Electronic Transitions in Complex Molecules. *Discuss. Faraday Soc.* **1950**, *9*, 14. https://doi.org/10.1039/df9500900014.

(54) Delorme, R.; Perrin, F. Durées de Fluorescence Des Sels d'uranyle Solides et de Leurs Solutions. *J. Phys. le Radium* **1929**, *10* (5), 177–186. https://doi.org/10.1051/jphysrad:01929001005017700.

(55) Lewis, G. N.; Kasha, M. Phosphorescence and the Triplet State. *J. Am. Chem. Soc.* **1944**, *66* (12), 2100–2116. https://doi.org/10.1021/ja01240a030.

(56) Parker, C. A.; Hatchard, C. G. Triplet-Singlet Emission in Fluid Solutions. Phosphorescence of Eosin. *Trans. Faraday Soc.* **1961**, *57*, 1894–1904. https://doi.org/10.1039/TF9615701894.

(57) Endo, A.; Sato, K.; Yoshimura, K.; Kai, T.; Kawada, A.; Miyazaki, H.; Adachi, C. Efficient Up-Conversion of Triplet Excitons into a Singlet State and Its Application for Organic Light Emitting Diodes. *Appl. Phys. Lett.* **2011**, *98* (8), 10–13. https://doi.org/10.1063/1.3558906.

(58) Uoyama, H.; Goushi, K.; Shizu, K.; Nomura, H.; Adachi, C. Highly Efficient Organic Light-Emitting Diodes from Delayed Fluorescence. *Nature* **2012**, *492* (7428), 234–238. https://doi.org/10.1038/nature11687.

(59) Zhang, Q.; Li, J.; Shizu, K.; Huang, S.; Hirata, S.; Miyazaki, H.; Adachi, C. Design of Efficient Thermally Activated Delayed Fluorescence Materials for Pure Blue Organic Light Emitting Diodes. *J. Am. Chem. Soc.* **2012**, *134* (36), 14706–14709. https://doi.org/10.1021/ja306538w.

(60) Stachelek, P.; Ward, J. S.; dos Santos, P. L.; Danos, A.; Colella, M.; Haase, N.; Raynes, S. J.; Batsanov, A. S.; Bryce, M. R.; Monkman, A. P. Molecular Design Strategies for Color Tuning of Blue TADF Emitters. *ACS Appl. Mater. Interfaces* **2019**, *11* (30), 27125–27133. https://doi.org/10.1021/acsami.9b06364.

(61) Saragi, T. P. I.; Spehr, T.; Siebert, A.; Fuhrmann-Lieker, T.; Salbeck, J. Spiro Compounds for Organic Optoelectronics. *Chem. Rev.* **2007**, *107* (4), 1011–1065. https://doi.org/10.1021/cr0501341.

(62) Woon, K. L.; Yi, C. L.; Pan, K. C.; Etherington, M. K.; Wu, C. C.; Wong, K. T.; Monkman, A. P. Intramolecular Dimerization Quenching of Delayed Emission in Asymmetric D-D'-A TADF Emitters. *J. Phys. Chem. C* **2019**, *123* (19), 12400–12410. https://doi.org/10.1021/acs.jpcc.9b01900.

(63) Hatakeyama, T.; Shiren, K.; Nakajima, K.; Nomura, S.; Nakatsuka, S.; Kinoshita, K.; Ni, J.; Ono, Y.; Ikuta, T. Ultrapure Blue Thermally Activated Delayed Fluorescence Molecules: Efficient HOMO-LUMO Separation by the Multiple Resonance Effect. *Adv. Mater.* **2016**, *28* (14), 2777–2781. https://doi.org/10.1002/adma.201505491.

(64) Shizu, K.; Kaji, H. Comprehensive Understanding of Multiple Resonance Thermally Activated Delayed Fluorescence through Quantum Chemistry Calculations. *Commun. Chem.* **2022**, *5* (1),

53. https://doi.org/10.1038/s42004-022-00668-6.

(65) Madayanad Suresh, S.; Hall, D.; Beljonne, D.; Olivier, Y.; Zysman-Colman, E. Multiresonant Thermally Activated Delayed Fluorescence Emitters Based on Heteroatom-Doped Nanographenes: Recent Advances and Prospects for Organic Light-Emitting Diodes. *Adv. Funct. Mater.* **2020**, *30* (33), 1908677. https://doi.org/10.1002/adfm.201908677.

(66) Eisenthal, K. B. Intermolecular and Intramolecular Excited State Charge Transfer. *Laser Chem.* **1983**, *3* (1–6), 145–162. https://doi.org/10.1155/LC.3.145.

(67) Ward, J. S.; Nobuyasu, R. S.; Batsanov, A. S.; Data, P.; Monkman, A. P.; Dias, F. B.; Bryce, M. R. The Interplay of Thermally Activated Delayed Fluorescence (TADF) and Room Temperature Organic Phosphorescence in Sterically-Constrained Donor–Acceptor Charge-Transfer Molecules. *Chem. Commun.* **2016**, *52* (12), 3–6. https://doi.org/10.1039/C5CC09645F.

(68) Pander, P.; Swist, A.; Soloducho, J.; Dias, F. B. Room Temperature Phosphorescence Lifetime and Spectrum Tuning of Substituted Thianthrenes. *Dye. Pigment.* **2017**, *142*, 315–322. https://doi.org/10.1016/j.dyepig.2017.03.049.

(69) Dias, F. B. Kinetics of Thermal-Assisted Delayed Fluorescence in Blue Organic Emitters with Large Singlet–Triplet Energy Gap. *Philos. Trans. R. Soc. A Math. Phys. Eng. Sci.* **2015**, *373* (2044), 20140447. https://doi.org/10.1098/rsta.2014.0447.

(70) Marian, C. M. Mechanism of the Triplet-to-Singlet Upconversion in the Assistant Dopant ACRXTN. *J. Phys. Chem. C* **2016**, *120* (7), 3715–3721. https://doi.org/10.1021/acs.jpcc.6b00060.

(71) Henry, B. R.; Siebrand, W. Spin–Orbit Coupling in Aromatic Hydrocarbons. Analysis of Nonradiative Transitions between Singlet and Triplet States in Benzene and Naphthalene. *J. Chem. Phys.* **1971**, *54* (3), 1072–1085. https://doi.org/10.1063/1.1674940.

(72) Lim, B. T.; Okajima, S.; Chandra, A. K.; Lim, E. C. Radiationless Transitions in Electron Donor-Acceptor Complexes: Selection Rules for S1 → T Intersystem Crossing and Efficiency of S1 → S0 Internal Conversion. *Chem. Phys. Lett.* **1981**, *79* (1), 22–27. https://doi.org/10.1016/0009-2614(81)85280-3.

(73) Penfold, T. J.; Gindensperger, E.; Daniel, C.; Marian, C. M. Spin-Vibronic Mechanism for Intersystem Crossing. *Chem. Rev.* **2018**, *118* (15), 6975–7025. https://doi.org/10.1021/acs.chemrev.7b00617.

(74) Marian, C. M. Understanding and Controlling Intersystem Crossing in Molecules. *Annu. Rev. Phys. Chem.* **2021**, *72* (1), 617–640. https://doi.org/10.1146/annurev-physchem-061020-053433.

(75) Metz, S.; Marian, C. M. Modulation of Intersystem Crossing by Chemical Composition and Solvent Effects: Benzophenone, Anthrone and Fluorenone. *ChemPhotoChem* **2022**, *6* (9). https://doi.org/10.1002/cptc.202200098.

(76) Urban, M.; Marek-Urban, P. H.; Durka, K.; Luliński, S.; Pander, P.; Monkman, A. P. TADF Invariant of Host Polarity and Ultralong Fluorescence Lifetimes in a Donor-Acceptor Emitter Featuring a Hybrid Sulfone-Triarylboron Acceptor**. *Angew. Chemie Int. Ed.* **2023**, *62* (9). https://doi.org/10.1002/anie.202217530.

(77) Kong, F.-F.; Tian, X.-J.; Zhang, Y.; Yu, Y.-J.; Jing, S.-H.; Zhang, Y.; Tian, G.-J.; Luo, Y.; Yang, J.-L.; Dong, Z.-C.; Hou, J. G. Probing Intramolecular Vibronic Coupling through Vibronic-State Imaging. *Nat. Commun.* **2021**, *12* (1), 1280. https://doi.org/10.1038/s41467-021-21571-z.

(78) Gibson, J.; Monkman, A. P.; Penfold, T. J. The Importance of Vibronic Coupling for Efficient Reverse Intersystem Crossing in Thermally Activated Delayed Fluorescence Molecules. *ChemPhysChem* **2016**, *17* (19), 2956–2961. https://doi.org/10.1002/cphc.201600662.

(79) Gibson, J.; Penfold, T. J. Nonadiabatic Coupling Reduces the Activation Energy in Thermally Activated Delayed Fluorescence. *Phys. Chem. Chem. Phys.* **2017**, *19* (12), 8428–8434. https://doi.org/10.1039/c7cp00719a.

(80) Etherington, M. K.; Gibson, J.; Higginbotham, H. F.; Penfold, T. J.; Monkman, A. P. Revealing the Spin–Vibronic Coupling Mechanism of Thermally Activated Delayed Fluorescence. *Nat. Commun.* **2016**, *7* (1), 13680. https://doi.org/10.1038/ncomms13680.

(81) Feng, R.; Duignan, T. J.; Autschbach, J. Electron–Nucleus Hyperfine Coupling Calculated from Restricted Active Space Wavefunctions and an Exact Two-Component Hamiltonian. *J. Chem. Theory Comput.* **2021**, *17* (1), 255–268. https://doi.org/10.1021/acs.jctc.0c01005.

(82) Glazov, M. M. *Hyperfine Interaction of Electron and Nuclear Spins*; Oxford University Press, 2018; Vol. 1. https://doi.org/10.1093/oso/9780198807308.003.0004.

(83) Benniston, A. C.; Harriman, A.; Rostron, J. P. The Effect of Solvent Polarity on the Photophysical Properties of 4-Cyano-(4'-Methylthio)Diphenylacetylene: A Prototypic Donor–Acceptor System. *Phys. Chem. Chem. Phys.* **2005**, *7* (16), 3041. https://doi.org/10.1039/b506776f.

(84) Balzani, V.; Ceroni, P.; Juris, A. *Photochemistry and Photophysics : Concepts, Research, Applications*, 1st ed.; John Wiley & Sons, Incorporated, 2014.

(85) Nigam, S.; Rutan, S. Principles and Applications of Solvatochromism. *Appl. Spectrosc.* **2001**, *55* (11), 362A-370A. https://doi.org/10.1366/0003702011953702.

(86) Reichardt, C. Solvatochromic Dyes as Solvent Polarity Indicators. *Chem. Rev.* **1994**, *94* (8), 2319–2358. https://doi.org/10.1021/cr00032a005.

(87) Stavrou, K.; Franca, L. G.; Monkman, A. P. Photophysics of TADF Guest–Host Systems: Introducing the Idea of Hosting Potential. *ACS Appl. Electron. Mater.* **2020**, *2* (9), 2868–2881. https://doi.org/10.1021/acsaelm.0c00514.

(88) Kelly, D.; Franca, L. G.; Stavrou, K.; Danos, A.; Monkman, A. P. Laplace Transform Fitting as a Tool To Uncover Distributions of Reverse Intersystem Crossing Rates in TADF Systems. *J. Phys. Chem. Lett.* **2022**, *13* (30), 6981–6986. https://doi.org/10.1021/acs.jpclett.2c01864.

(89) Coubeils, J. L.; Pullman, B. Molecular Orbital Study of the Conformational Properties of Phenothiazines. *Theor. Chim. Acta* **1972**, *24* (1), 35–41. https://doi.org/10.1007/BF00528308.

(90) Tanaka, H.; Shizu, K.; Nakanotani, H.; Adachi, C. Dual Intramolecular Charge-Transfer Fluorescence Derived from a Phenothiazine-Triphenyltriazine Derivative. *J. Phys. Chem. C* **2014**, *118* (29), 15985–15994. https://doi.org/10.1021/jp501017f.

(91) Dias, F. B.; Santos, J.; Graves, D. R.; Data, P.; Nobuyasu, R. S.; Fox, M. A.; Batsanov, A. S.; Palmeira, T.; Berberan-Santos, M. N.; Bryce, M. R.; Monkman, A. P. The Role of Local Triplet Excited States and D-A Relative Orientation in Thermally Activated Delayed Fluorescence: Photophysics and Devices. *Adv. Sci.* **2016**, *3* (12), 1600080. https://doi.org/10.1002/advs.201600080.

(92) Phan Huu, D. K. A.; Saseendran, S.; Dhali, R.; Franca, L. G.; Stavrou, K.; Monkman, A.; Painelli, A. Thermally Activated Delayed Fluorescence: Polarity, Rigidity, and Disorder in Condensed Phases. *J. Am. Chem. Soc.* **2022**, *144* (33), 15211–15222.

https://doi.org/10.1021/jacs.2c05537.

(93) Northey, T.; Stacey, J.; Penfold, T. J. The Role of Solid State Solvation on the Charge Transfer State of a Thermally Activated Delayed Fluorescence Emitter. *J. Mater. Chem. C* **2017**, *5* (42), 11001–11009. https://doi.org/10.1039/C7TC04099G.

(94) Woo, S.-J.; Kim, Y.-H.; Kim, J.-J. Dihedral Angle Distribution of Thermally Activated Delayed Fluorescence Molecules in Solids Induces Dual Phosphorescence from Charge-Transfer and Local Triplet States. *Chem. Mater.* **2021**, *33* (14), 5618–5630. https://doi.org/10.1021/acs.chemmater.1c01011.

(95) dos Santos, P. L.; Ward, J. S.; Batsanov, A. S.; Bryce, M. R.; Monkman, A. P. Optical and Polarity Control of Donor–Acceptor Conformation and Their Charge-Transfer States in Thermally Activated Delayed-Fluorescence Molecules. *J. Phys. Chem. C* **2017**, *121* (30), 16462–16469. https://doi.org/10.1021/acs.jpcc.7b03672.

(96) Samanta, P. K.; Kim, D.; Coropceanu, V.; Brédas, J.-L. Up-Conversion Intersystem Crossing Rates in Organic Emitters for Thermally Activated Delayed Fluorescence: Impact of the Nature of Singlet vs Triplet Excited States. *J. Am. Chem. Soc.* **2017**, *139* (11), 4042–4051. https://doi.org/10.1021/jacs.6b12124.

(97) Stavrou, K.; Danos, A.; Hama, T.; Hatakeyama, T.; Monkman, A. Hot Vibrational States in a High-Performance Multiple Resonance Emitter and the Effect of Excimer Quenching on Organic Light-Emitting Diodes. *ACS Appl. Mater. Interfaces* **2021**, *13* (7), 8643–8655. https://doi.org/10.1021/acsami.0c20619.

(98) Cho, E.; Hong, M.; Coropceanu, V.; Brédas, J. The Role of Intermolecular Interactions on the Performance of Organic Thermally Activated Delayed Fluorescence (TADF) Materials. *Adv. Opt. Mater.* **2021**, *9* (14), 2002135. https://doi.org/10.1002/adom.202002135.

(99) Pander, P.; Data, P.; Dias, F. B. Time-Resolved Photophysical Characterization of Triplet-Harvesting Organic Compounds at an Oxygen-Free Environment Using an ICCD Camera. *J. Vis. Exp.* **2018**, *142* (142). https://doi.org/10.3791/56614.

(100) Brouwer, A. M. Standards for Photoluminescence Quantum Yield Measurements in Solution (IUPAC Technical Report). *Pure Appl. Chem.* **2011**, *83* (12), 2213–2228. https://doi.org/10.1351/PAC-REP-10-09-31.

(101) Jankus, V.; Chiang, C. J.; Dias, F.; Monkman, A. P. Deep Blue Exciplex Organic Light-Emitting Diodes with Enhanced Efficiency; P-Type or E-Type Triplet Conversion to Singlet Excitons? *Adv. Mater.* **2013**, *25* (10), 1455–1459. https://doi.org/10.1002/adma.201203615.

(102) Scientific, H. Time-resolved Fluorescence Lifetime Measurements Technical Note. **2018**.

(103) Haase, N.; Danos, A.; Pflumm, C.; Morherr, A.; Stachelek, P.; Mekic, A.; Brütting, W.; Monkman, A. P. Kinetic Modeling of Transient Photoluminescence from Thermally Activated Delayed Fluorescence. *J. Phys. Chem. C* **2018**, *122* (51), 29173–29179. https://doi.org/10.1021/acs.jpcc.8b11020.

(104) Yersin, H.; Rausch, A. F.; Czerwieniec, R.; Hofbeck, T.; Fischer, T. The Triplet State of Organo-Transition Metal Compounds. Triplet Harvesting and Singlet Harvesting for Efficient OLEDs. *Coord. Chem. Rev.* **2011**, *255* (21–22), 2622–2652. https://doi.org/10.1016/j.ccr.2011.01.042.

(105) Nasu, K.; Nakagawa, T.; Nomura, H.; Lin, C.-J.; Cheng, C.-H.; Tseng, M.-R.; Yasuda, T.; Adachi, C. A Highly Luminescent Spiro-Anthracenone-Based Organic Light-Emitting Diode Exhibiting Thermally Activated Delayed Fluorescence. *Chem. Commun.* **2013**, *49* (88), 10385. https://doi.org/10.1039/c3cc44179b.

(106) Wang, Y. K.; Huang, C. C.; Ye, H.; Zhong, C.; Khan, A.; Yang, S. Y.; Fung, M. K.; Jiang, Z. Q.; Adachi, C.; Liao, L. S. Through Space Charge Transfer for Efficient Sky-Blue Thermally Activated Delayed Fluorescence (TADF) Emitter with Unconjugated Connection. *Adv. Opt. Mater.* **2020**, *8* (2), 1–7. https://doi.org/10.1002/adom.201901150.

(107) Tsai, W.-L.; Huang, M.-H.; Lee, W.-K.; Hsu, Y.-J.; Pan, K.-C.; Huang, Y.-H.; Ting, H.-C.; Sarma, M.; Ho, Y.-Y.; Hu, H.-C.; Chen, C.-C.; Lee, M.-T.; Wong, K.-T.; Wu, C.-C. A Versatile Thermally Activated Delayed Fluorescence Emitter for Both Highly Efficient Doped and Non-Doped Organic Light Emitting Devices. *Chem. Commun.* **2015**, *51* (71), 13662–13665. https://doi.org/10.1039/C5CC05022G.

(108) Lyskov, I.; Marian, C. M. Climbing up the Ladder: Intermediate Triplet States Promote the Reverse Intersystem Crossing in the Efficient TADF Emitter ACRSA. *J. Phys. Chem. C* **2017**, *121* (39), 21145–21153. https://doi.org/10.1021/acs.jpcc.7b06187.

(109) Franca, L. G.; Long, Y.; Li, C.; Danos, A.; Monkman, A. The Critical Role of Nπ* States in the Photophysics and Thermally Activated Delayed Fluorescence of Spiro Acridine-Anthracenone. *J. Phys. Chem. Lett.* **2021**, *12* (5), 1490–1500. https://doi.org/10.1021/acs.jpclett.0c03314.

(110) dos Santos, P. L.; Dias, F. B.; Monkman, A. P. Investigation of the Mechanisms Giving Rise to TADF in Exciplex States. *J. Phys. Chem. C* **2016**, *120* (32), 18259–18267. https://doi.org/10.1021/acs.jpcc.6b05198.

(111) Kaminski, J. M.; Rodríguez-Serrano, A.; Dinkelbach, F.; Miranda-Salinas, H.; Monkman, A. P.; Marian, C. M. Vibronic Effects Accelerate the Intersystem Crossing Processes of the Through-Space Charge Transfer States in the Triptycene Bridged Acridine–Triazine Donor–Acceptor Molecule TpAT-TFFO. *Chem. Sci.* **2022**, *13* (23), 7057–7066. https://doi.org/10.1039/D1SC07101G.

(112) Simmons, H. E.; Fukunaga, T. Spiroconjugation. *J. Am. Chem. Soc.* **1967**, *89* (20), 5208–5215. https://doi.org/10.1021/ja00996a022.

(113) Katoh, T.; Ogawa, K.; Inagaki, Y.; Okazaki, R. Evidence for Spiro-Conjugation in Perpendicularly-Linked Pentamethinestreptocyanine Dimers. *Bull. Chem. Soc. Jpn.* **1997**, *70* (5), 1109–1114. https://doi.org/10.1246/bcsj.70.1109.

(114) Zhu, L.; Zhong, C.; Liu, Z.; Yang, C.; Qin, J. New Intramolecular Through-Space Charge Transfer Emission: Tunable Dual Fluorescence of Terfluorenes. *Chem. Commun.* **2010**, *46* (36), 6666. https://doi.org/10.1039/c0cc00136h.

(115) Wössner, J. S.; Grenz, D. C.; Kratzert, D.; Esser, B. Tuning the Optical Properties of Spiro-Centered Charge-Transfer Dyes by Extending the Donor or Acceptor Part. *Org. Chem. Front.* **2019**, *6* (21), 3649–3656. https://doi.org/10.1039/C9QO01134J.

(116) Jankus, V.; Aydemir, M.; Dias, F. B.; Monkman, A. P. Generating Light from Upper Excited Triplet States: A Contribution to the Indirect Singlet Yield of a Polymer OLED, Helping to Exceed the 25% Singlet Exciton Limit. *Adv. Sci.* **2016**, *3* (1), 1500221. https://doi.org/10.1002/advs.201500221.

(117) Hintschich, S. I.; Rothe, C.; King, S. M.; Clark, S. J.; Monkman, A. P. The Complex Excited-State Behavior of a Polyspirobifluorene Derivative: The Role of Spiroconjugation and Mixed Charge Transfer Character on Excited-State Stabilization and Radiative Lifetime. *J. Phys. Chem. B* **2008**, *112* (51), 16300–16306. https://doi.org/10.1021/jp8044884.

(118) Nakagawa, T.; Ku, S.-Y.; Wong, K.-T.; Adachi, C. Electroluminescence Based on Thermally Activated Delayed Fluorescence Generated by a Spirobifluorene Donor–Acceptor Structure.

Chem. Commun. **2012**, *48* (77), 9580. https://doi.org/10.1039/c2cc31468a.

(119) Serevičius, T.; Skaisgiris, R.; Dodonova, J.; Jagintavičius, L.; Bucevičius, J.; Kazlauskas, K.; Juršėnas, S.; Tumkevičius, S. Emission Wavelength Dependence on the RISC Rate in TADF Compounds with Large Conformational Disorder. *Chem. Commun.* **2019**, *55* (13), 1975–1978. https://doi.org/10.1039/C8CC08906J.

(120) Olivier, Y.; Yurash, B.; Muccioli, L.; D'Avino, G.; Mikhnenko, O.; Sancho-García, J. C.; Adachi, C.; Nguyen, T. Q.; Beljonne, D. Nature of the Singlet and Triplet Excitations Mediating Thermally Activated Delayed Fluorescence. *Phys. Rev. Mater.* **2017**, *1* (7), 1–6. https://doi.org/10.1103/PhysRevMaterials.1.075602.

(121) Hempe, M.; Kukhta, N. A.; Danos, A.; Fox, M. A.; Batsanov, A. S.; Monkman, A. P.; Bryce, M. R. Vibrational Damping Reveals Vibronic Coupling in Thermally Activated Delayed Fluorescence Materials. *Chem. Mater.* **2021**, *33* (9), 3066–3080. https://doi.org/10.1021/acs.chemmater.0c03783.

(122) Oh, C. S.; Pereira, D. D. S.; Han, S. H.; Park, H. J.; Higginbotham, H. F.; Monkman, A. P.; Lee, J. Y. Dihedral Angle Control of Blue Thermally Activated Delayed Fluorescent Emitters through Donor Substitution Position for Efficient Reverse Intersystem Crossing. *ACS Appl. Mater. Interfaces* **2018**, *10* (41), 35420–35429. https://doi.org/10.1021/acsami.8b10595.

(123) Kukhta, N. A.; Higginbotham, H. F.; Matulaitis, T.; Danos, A.; Bismillah, A. N.; Haase, N.; Etherington, M. K.; Yufit, D. S.; McGonigal, P. R.; Gražulevičius, J. V.; Monkman, A. P. Revealing Resonance Effects and Intramolecular Dipole Interactions in the Positional Isomers of Benzonitrile-Core Thermally Activated Delayed Fluorescence Materials. *J. Mater. Chem. C* **2019**, *7* (30), 9184–9194. https://doi.org/10.1039/C9TC02742D.

(124) Cho, H. J.; Kim, S. W.; Kim, S.; Lee, S.; Lee, J.; Cho, Y.; Lee, Y.; Lee, T. W.; Shin, H. J.; Song, C. Suppressing π-π Stacking Interactions for Enhanced Solid-State Emission of Flat Aromatic Molecules: Via Edge Functionalization with Picket-Fence-Type Groups. *J. Mater. Chem. C* **2020**, *8* (48), 17289–17296. https://doi.org/10.1039/d0tc04376a.

(125) Reichardt, C.; Welton, T. *Solvents and Solvent Effects in Organic Chemistry*; Wiley-VCH Verlag GmbH & Co. KGaA: Weinheim, Germany, 2010. https://doi.org/10.1002/9783527632220.

(126) dos Santos, P. L.; Etherington, M. K.; Monkman, A. P. Chemical and Conformational Control of the Energy Gaps Involved in the Thermally Activated Delayed Fluorescence Mechanism. *J. Mater. Chem. C* **2018**, *6* (18), 4842–4853. https://doi.org/10.1039/C8TC00991K.

(127) dos Santos, P. L.; Ward, J. S.; Bryce, M. R.; Monkman, A. P. Using Guest–Host Interactions To Optimize the Efficiency of TADF OLEDs. *J. Phys. Chem. Lett.* **2016**, *7* (17), 3341–3346. https://doi.org/10.1021/acs.jpclett.6b01542.

(128) Northey, T.; Stacey, J.; Penfold, T. J. The Role of Solid State Solvation on the Charge Transfer State of a Thermally Activated Delayed Fluorescence Emitter. *J. Mater. Chem. C* **2017**, *5* (42), 11001–11009. https://doi.org/10.1039/c7tc04099g.

(129) Greene, B. I.; Hochstrasser, R. M.; Weisman, R. B. Picosecond Transient Spectroscopy of Molecules in Solution. *J. Chem. Phys.* **1979**, *70* (3), 1247–1259. https://doi.org/10.1063/1.437617.

(130) Fan, J.; Cai, L.; Lin, L.; Wang, C. Understanding the Light-Emitting Mechanism of an X-Shape Organic Thermally Activated Delayed Fluorescence Molecule: First-Principles Study. *Chemical Physics Letters*. 2016, pp 33–38. https://doi.org/10.1016/j.cplett.2016.10.009.

(131) Nobuyasu, R. S.; Ren, Z.; Griffiths, G. C.; Batsanov, A. S.; Data, P.; Yan, S.; Monkman, A. P.;

Bryce, M. R.; Dias, F. B. Rational Design of TADF Polymers Using a Donor-Acceptor Monomer with Enhanced TADF Efficiency Induced by the Energy Alignment of Charge Transfer and Local Triplet Excited States. *Adv. Opt. Mater.* **2016**, *4* (4), 597–607. https://doi.org/10.1002/adom.201500689.

(132) Koti, A. S. R.; Periasamy, N. Time Resolved Area Normalized Emission Spectroscopy (TRANES) of DMABN Confirms Emission from Two States. *Res. Chem. Intermed.* **2002**, *28* (7–9), 831–836. https://doi.org/10.1163/15685670260469447.

(133) Zhang, X.; Zhao, X.; Ye, K.; Zhao, J. Detection of the Dark States in Thermally Activated Delayed Fluorescence (TADF) Process of Electron Donor-Acceptor Dyads: Insights from Optical Transient Absorption Spectroscopy. *Chem. – A Eur. J.* **2023**, *202203737*. https://doi.org/10.1002/chem.202203737.

(134) Notsuka, N.; Nakanotani, H.; Noda, H.; Goushi, K.; Adachi, C. Observation of Nonradiative Deactivation Behavior from Singlet and Triplet States of Thermally Activated Delayed Fluorescence Emitters in Solution. *J. Phys. Chem. Lett.* **2020**, *11* (2), 562–566. https://doi.org/10.1021/acs.jpclett.9b03302.

(135) Stavrou, K.; Franca, L. G.; Böhmer, T.; Duben, L. M.; Marian, C. M.; Monkman, A. P. Unexpected Quasi-Axial Conformer in Thermally Activated Delayed Fluorescence DMAC-TRZ, Pushing Green OLEDs to Blue. *Adv. Funct. Mater.* **2023**, *33* (25), 2300910. https://doi.org/10.1002/adfm.202300910.

(136) Sarma, M.; Wong, K.-T. Exciplex: An Intermolecular Charge-Transfer Approach for TADF. *ACS Appl. Mater. Interfaces* **2018**, *10* (23), 19279–19304. https://doi.org/10.1021/acsami.7b18318.

(137) Li, J.; Shen, P.; Zhao, Z.; Tang, B. Z. Through-Space Conjugation: A Thriving Alternative for Optoelectronic Materials. *CCS Chem.* **2019**, *1* (2), 181–196. https://doi.org/10.31635/ccschem.019.20180020.

(138) Zheng, X.; Huang, R.; Zhong, C.; Xie, G.; Ning, W.; Huang, M.; Ni, F.; Dias, F. B.; Yang, C. Achieving 21% External Quantum Efficiency for Nondoped Solution-Processed Sky-Blue Thermally Activated Delayed Fluorescence OLEDs by Means of Multi-(Donor/Acceptor) Emitter with Through-Space/-Bond Charge Transfer. *Adv. Sci.* **2020**, *7* (7), 1902087. https://doi.org/10.1002/advs.201902087.

(139) Yu, M.; Zhu, X.; Zeng, J.; Liu, H.; Huang, R.; Zhuang, Z.; Shen, P.; Zhao, Z.; Tang, B. Z. Comparative Study on the Impact of Through-Space Charge Transfer over the Electroluminescence Performance of Delayed Fluorescence Molecules. *J. Mater. Chem. C* **2021**, *9* (41), 14808–14814. https://doi.org/10.1039/d1tc03564a.

(140) Herington, E. F. G.; Jones, J. I. Ultraviolet Absorption Spectra of Some Copolymers Containing Acenaphthylene, and of Related Compounds. *J. Polym. Sci.* **1949**, *4* (6), 725–733. https://doi.org/10.1002/pol.1949.120040605.

(141) Kumar, S.; Franca, L. G.; Stavrou, K.; Crovini, E.; Cordes, D. B.; Slawin, A. M. Z.; Monkman, A. P.; Zysman-Colman, E. Investigation of Intramolecular Through-Space Charge-Transfer States in Donor–Acceptor Charge-Transfer Systems. *J. Phys. Chem. Lett.* **2021**, *12* (11), 2820–2830. https://doi.org/10.1021/acs.jpclett.1c00265.

(142) de Sa Pereira, D.; Lee, D. R.; Kukhta, N. A.; Lee, K. H.; Kim, C. L.; Batsanov, A. S.; Lee, J. Y.; Monkman, A. P. The Effect of a Heavy Atom on the Radiative Pathways of an Emitter with Dual Conformation, Thermally-Activated Delayed Fluorescence and Room Temperature Phosphorescence. *J. Mater. Chem. C* **2019**, *7* (34), 10481–10490.

https://doi.org/10.1039/C9TC02477H.

(143) Zachariasse, K. A. Comment on “Pseudo-Jahn–Teller and TICT-Models: A Photophysical Comparison of Meta-and Para-DMABN Derivatives” [Chem. Phys. Lett. 305 (1999) 8]. *Chem. Phys. Lett.* **2000**, *320* (1–2), 8–13. https://doi.org/10.1016/S0009-2614(00)00230-X.

(144) Colella, M.; Danos, A.; Monkman, A. P. Less Is More: Dilution Enhances Optical and Electrical Performance of a TADF Exciplex. *J. Phys. Chem. Lett.* **2019**, *10* (4), 793–798. https://doi.org/10.1021/acs.jpclett.8b03646.

(145) The Kinetics of Phosphorescence and Delayed Fluorescence Decay for Aromatic Hydrocarbons in Liquid Paraffin. *Proc. R. Soc. London. Ser. A. Math. Phys. Sci.* **1964**, *281* (1386), 420–436. https://doi.org/10.1098/rspa.1964.0191.

(146) Aydemir, M.; Haykir, G.; Türksoy, F.; Gümüş, S.; Dias, F. B.; Monkman, A. P. Synthesis and Investigation of Intra-Molecular Charge Transfer State Properties of Novel Donor-Acceptor-Donor Pyridine Derivatives: The Effects of Temperature and Environment on Molecular Configurations and the Origin of Delayed Fluorescence. *Phys. Chem. Chem. Phys.* **2015**, *17* (38), 25572–25582. https://doi.org/10.1039/c5cp03937a.

(147) Wada, Y.; Nakagawa, H.; Matsumoto, S.; Wakisaka, Y.; Kaji, H. Organic Light Emitters Exhibiting Very Fast Reverse Intersystem Crossing. *Nat. Photonics* **2020**, *14* (10), 643–649. https://doi.org/10.1038/s41566-020-0667-0.

(148) Penfold, T. J.; Dias, F. B.; Monkman, A. P. The Theory of Thermally Activated Delayed Fluorescence for Organic Light Emitting Diodes. *Chem. Commun.* **2018**, *54* (32), 3926–3935. https://doi.org/10.1039/C7CC09612G.